Aalborg Universitet

ADDITIVE MANUFACTURING AND PERCRYSTALLIZATION FOR IMPROVED MEMBRANE CRYSTALLIZATION

Kirkebæk, Bastian Stiem

DOI (link to publication from Publisher):
10.54337/aau807374723

Publication date:
2025

Document Version
Publisher's PDF, also known as Version of record

Link to publication from Aalborg University

Citation for published version (APA):
Kirkebæk, B. S. (2025). *ADDITIVE MANUFACTURING AND PERCRYSTALLIZATION FOR IMPROVED MEMBRANE CRYSTALLIZATION*. Aalborg University Open Publishing. https://doi.org/10.54337/aau807374723

General rights
Copyright and moral rights for the publications made accessible in the public portal are retained by the authors and/or other copyright owners and it is a condition of accessing publications that users recognise and abide by the legal requirements associated with these rights.

- Users may download and print one copy of any publication from the public portal for the purpose of private study or research.
- You may not further distribute the material or use it for any profit-making activity or commercial gain
- You may freely distribute the URL identifying the publication in the public portal -

Take down policy
If you believe that this document breaches copyright please contact us at vbn@aub.aau.dk providing details, and we will remove access to the work immediately and investigate your claim.

Downloaded from vbn.aau.dk on: March 27, 2026

AAU OPEN

AALBORG UNIVERSITY
OPEN PUBLISHING

ADDITIVE MANUFACTURING AND PERCRYSTALLIZATION FOR IMPROVED MEMBRANE CRYSTALLIZATION

BY
BASTIAN STIEM KIRKEBÆK

PhD Thesis 2025

AALBORG
UNIVERSITY

ADDITIVE MANUFACTURING AND PERCRYSTALLIZATION FOR IMPROVED MEMBRANE CRYSTALLIZATION

by

Bastian Stiem Kirkebæk

AALBORG UNIVERSITY
DENMARK

PhD Dissertation 2025
August 2025
Department of Chemistry and Bioscience

Submitted: September 2025

Main Supervisor: Associate Professor Cejna Anna Quist-Jensen
Aalborg University, Aalborg, Denmark

Co-supervisors: Associate Professor Aamer Ali
Aalborg University, Aalborg, Denmark

Professor David Bue Pedersen
Technical University of Denmark, Lyngby, Denmark

Assessment: Associate Professor Jens Muff (chair)
Aalborg University, Denmark

Professor Patricia Luis Alconero
Catholic University of Louvain, Belgium

Professor João Crespo
Universidade Nova de Lisbo, Portugal

Department: Department of Chemistry and Bioscience

PhD Series: Faculty of Engineering and Science, Aalborg University

ISSN: 2446-1636
ISBN: 97887-7642-130-4

Published by: Aalborg University Open Publishing | www.open.aau.dk

© Copyright: Bastian Stiem Kirkebæk

Preface

This dissertation is submitted in partial fulfilment of the requirements for obtaining the degree of doctor of philosophy (Ph.D.). The dissertation consists of abstracts in English and Danish, a main thesis and supporting papers and data.

This study was conducted as a 4+4 PhD scheme with the first two years from 2021 to 2023 consisting of 50% Masters and 50% PhD work. 2023 to 2025 100% PhD work. The PhD therefore also contains elements from the masters thesis as supplementing data for the introduction and is reffered to as [A1].

The study was conducted at the Section of Bioresources and Process Engineering , Department of Chemistry and Bioscience at Aalborg University in the period from September 2021 to August 2025.

The project was financed by the Poul Due Jensen foundation as “Membrane Distillation and Membrane Crystallization for recovery of water and minerals from waste streams” project. Furthermore, some elements of the thesis has been funded by Danish Offshore Technology Center through their Radical Innovation Sprint projects.

Part of the work was carried out at Technical University of Denmark (Copenhagen, Denmark) and Lund University (Lund, Sweden).

English Summary

Growing global demand for high-quality water sources, such as freshwater and industrially valuable ultrapure water (UPW), as well as critical minerals, is driving the need for advanced desalination technologies. Among these, Zero Liquid Discharge (ZLD) has emerged as a particularly promising strategy, enabling both the production of high-purity water and the recovery of valuable minerals, while minimizing the environmental footprint of brine disposal.

Traditionally, desalination has relied on thermally driven distillation processes or, more recently, reverse osmosis (RO). While effective, these methods have well-known limitations, including, membrane fouling, and limited performance at high salinity. Membrane Distillation Crystallization (MCr) has been identified as an appealing alternative due to its ability to couple desalination with controlled mineral precipitation. However, widespread adoption has been constrained by persistent challenges, including membrane wetting, scaling, limited selectivity, and difficulties in recovering precipitated solids.

This thesis investigates two complementary approaches to address these limitations: the development of novel membranes via additive manufacturing (AM) towards enhanced precipitation control, and the application of percrystallization as a robust, thermally driven crystallization method.

Given current constraints on resolution and processing speed, directly printing functional membranes via AM is often impractical. A more viable approach involves printing inherently porous materials. Accordingly, a particular focus was placed on combining Vat Photopolymerization (VPP) with Polymerization-Induced Phase Separation (PIPS). This combination allows the fabrication of nanoporous membranes at the highest available AM resolution. Moreover, VPP–PIPS enables membranes with precisely tunable porosity, geometry, and physicochemical properties.

In the first study, systematic copolymerization of polyurethane acrylate, hydroxyethyl methacrylate, and tert-butyl acrylate was used to create VPP–PIPS membranes with tailored hydrophobicity/hydrophilicity (contact angles ranging from 44.3° ±4.0° to 108.8° ±2.6°), thermal stability exceeding 260–345 °C, and mechanical strength from 1.95 to 21.2 MPa, performance levels suitable for demanding desalination applications. Additionally, high-resolution VPP printing enabled micro-scale topographies that further

increased hydrophobicity, achieving contact angles up to 136.8° ±1.0°, demonstrating AM as a powerful tool for modifying membrane properties.

The second study utilized a hydrophobic ink formulation based on tert-butyl acrylate to produce fully 3D-printed VPP–PIPS hydrophobic tubular membranes with diverse geometries for direct contact membrane distillation (DCMD). The results showed that membrane geometry and porosity could be reliably controlled, producing membranes with stable water flux and high salt rejection even at NaCl concentrations exceeding 250 g/L. Unlike a commercial membrane tested under similar conditions, the printed membranes maintained performance through the onset of NaCl crystallization without experiencing pore wetting. However, scaling remained an important challenge, leading to significant flux decline after precipitation. Nevertheless, these PFAS-free VPP–PIPS membranes demonstrate a strong alternative to conventional materials, offering precise control over microstructure and geometry.

The third study focused on overcoming the mechanical brittleness inherent to VPP-derived membranes by printing porous spacers directly onto commercial membrane surfaces. Preliminary tests showed that these integrated spacers significantly improved fouling resistance, achieving up to 192% higher flux during microfiltration of fouling-prone feeds (yeast suspensions). This illustrates the potential for AM to tailor hydrodynamics at the membrane surface, an approach that could also benefit MD and MCr applications.

In parallel, this thesis advances the development and characterization of percrystallization, a process that combines permeation, evaporation, and crystallization across semipermeable membranes. Unlike conventional MD, percrystallization relies on liquid permeation through wetted membranes, eliminating the need for hydrophobicity, broadening material compatibility, and facilitating easier crystal recovery on the permeate side. Additionally, because the membrane remains a barrier prior to evaporation, there is potential for selective solute transport not achievable with MD.

A percrystallization system was designed and built, operating without vacuum assistance, thereby enabling desalination processes that can run almost entirely on low-grade or waste heat sources such as industrial waste heat or solar energy.

The fourth study applied this system to desalinate real seawater from the North Sea. Using both UF and NF membranes, it was demonstrated that ZLD and mineral recovery could be achieved. UF membranes consistently provided higher water throughput than NF membranes. Moreover, experiments showed that the composition of the sweeping gas influenced both water flux and the nature of the precipitated crystals; notably, CO_2 sweeping gas promoted greater carbonate precipitation. The process exhibited excellent stability at high salinities (30–150 g/L), operating continuously for more than 160 hours and achieving 91.7% volume reduction without performance decline as minerals precipitated.

The fifth study tested percrystallization as a treatment method for industrial wastewater. Results demonstrated that ion rejection characteristics differed substantially in percrystallization mode compared to pressure-driven operation with the same membranes. Again, percrystallization proved to be a stable, reliable desalination technique capable of achieving relatively high flux in scenarios where DCMD would suffer from severe wetting. Selectivity differences between UF and NF membranes were observed in the composition of permeate-side crystals, highlighting the potential for enhanced selectivity.

A sixth, smaller study evaluated percrystallization for treating biorefinery wastewater containing high suspended solids (sugar beet wash water). The process operated continuously for over 600 hours, further demonstrating robustness and maturity. The recovered solids were notably rich in phosphorus, underscoring the potential for resource recovery alongside desalination.

Collectively, the findings presented herein demonstrate that advanced additive-manufactured membranes and percrystallization can address many of the key barriers limiting existing ZLD technologies. VPP–PIPS offers unmatched geometric freedom, material tunability, and the ability to tailor surface interactions critical to nucleation and scaling. Meanwhile, percrystallization provides a simple and scalable approach to desalination and resource recovery without requiring high-pressure operation or specialized hydrophobic membranes. While promising, further research is needed to improve the mechanical robustness and scalability of 3D-printed membranes, optimize crystallization selectivity, and integrate heat recovery strategies to reduce energy demands. Overall, this thesis contributes novel insights and practical advances toward realizing ZLD and brine mining solutions. By combining innovative membrane design with process intensification through percrystallization, this work helps lay the foundation for next-generation desalination technologies capable of addressing water scarcity, resource recovery, and environmental protection in parallel.

Resume in Danish

Den stigende globale efterspørgsel efter høj-kvalitets vandkilder, såsom ferskvand og industrielt værdifuldt ultraprent vand (UPW), samt kritiske mineraler driver behovet for avancerede afsaltnings teknologier. Blandt disse er Zero Liquid Discharge (ZLD) fremhævet som en særligt lovende strategi, der muliggør både produktion af højpuret vand og genvinding af værdifulde mineraler, samtidig med at miljøaftrykket fra saltlagebortskaffelse minimeres.

Traditionelt har afsaltning været baseret på termisk drevne destillationsprocesser eller, mere moderne, revers osmose (RO). Selvom disse metoder er effektive, har de velkendte begrænsninger, herunder membrantilsmudsning og begrænset ydeevne ved høje saliniteter. Membran-destillationskrystallisering (MCr) er identificeret som et lovende alternativ på grund af sin evne til at kombinere afsaltning med kontrolleret mineraludfældning. Udbredt anvendelse er dog blevet hæmmet af vedvarende udfordringer som membranvædning, tilskalning, begrænset selektivitet og vanskeligheder med at genvinde udfældede faste stoffer.

Denne afhandling undersøger to komplementære tilgange for at adressere disse udfordringer: udvikling af nye membraner via additiv fremstilling (AM) med henblik på at forbedre kontrollen med udfældning samt anvendelsen af perkrystallisering som en robust, termisk drevet krystallisationsmetode.

Givet de nuværende begrænsninger i opløsning og procestempo er det ofte upraktisk direkte at 3D-printe funktionelle membraner via AM. En mere levedygtig tilgang involverer print af iboende porøse materialer. Derfor blev der lagt særlig vægt på kombinationen af Vat Photopolymerization (VPP) med Polymerization-Induced Phase Separation (PIPS). Denne kombination muliggør fremstilling af nanoporede membraner i den højest tilgængelige AM-opløsning. Desuden gør VPP–PIPS det muligt at fremstille membraner med præcist justerbar porøsitet, geometri og fysikokemiske egenskaber.

I det første studie blev systematisk copolymerisering af polyurethanakrylat, hydroxyethylmethacrylat og tert-butylakrylat anvendt til at fremstille VPP–PIPS membraner med tilpasset hydrofobicitet/hydrofobicitet (kontaktvinkler fra 44,3° ±4,0° til 108,8° ±2,6°), termisk stabilitet på over 260–345 °C og mekanisk styrke fra 1,95 til 21,2 MPa, niveauer velegnede til krævende afsaltningsanvendelser. Derudover muliggjorde højopløselig VPP-print mikroskala-topografier, der yderligere øgede hydrofobiciteten og opnåede

kontaktvinkler op til 136,8° ±1,0°, hvilket demonstrerer AM som et stærkt værktøj til at modificere membraners egenskaber.

Det andet studie anvendte en hydrofob resinformulering baseret på tert-butylakrylat til at fremstille fuldt 3D-printede VPP–PIPS hydrofobe rørformede membraner med forskellige geometrier til direkte kontaktmembrandestillation (DCMD). Resultaterne viste, at membrangeometri og porøsitet kunne styres pålideligt og gav membraner med stabil vandflux og høj saltretention, selv ved NaCl-koncentrationer over 250 g/L. I modsætning til en kommerciel membran testet under lignende betingelser opretholdt de printede membraner ydeevnen gennem begyndende NaCl-krystallisering uden porevædning. Dog forblev tilskalning en vigtig udfordring, der førte til betydeligt fluxfald efter udfældning. Ikke desto mindre demonstrerer disse PFAS-frie VPP–PIPS membraner et stærkt alternativ til konventionelle materialer med præcis kontrol over mikrostruktur og geometri.

Det tredje studie fokuserede på at overvinde den mekaniske skørhed, som er iboende i VPP-baserede membraner, ved at printe porøse afstandsstykker direkte på kommercielle membranoverflader. Indledende tests viste, at disse integrerede afstandsstykker signifikant forbedrede modstandsdygtigheden over for tilsmudsning og opnåede op til 192% højere flux under mikrofiltrering af fødeemner med høj fouling (gærsuspensioner). Dette illustrerer potentialet for AM til at skræddersy strømningsforholdene på membranoverfladen, hvilket også kan gavne MD- og MCr-processer.

Parallelt videreudvikler afhandlingen perkrystallisering, en proces der kombinerer permeation, fordampning og krystallisering over semipermeable membraner. I modsætning til konventionel MD bygger perkrystallisering på væskepermeation gennem vædede membraner, hvilket eliminerer behovet for hydrofobicitet, udvider materialekompatibiliteten og gør det lettere at opsamle krystaller på permeatsiden. Desuden fungerer membranen som en barriere før fordampning, hvilket giver mulighed for selektiv transport af opløste stoffer, som ikke kan opnås med MD.

Et perkrystallisationssystem blev designet og opbygget, som opererede uden vakuumhjælp og dermed muliggør afsaltning næsten udelukkende drevet af lavkvalitets eller spildvarme, f.eks. industriel spildvarme eller solenergi.

Det fjerde studie anvendte systemet til afsaltning af reelt havvand fra Nordsøen. Ved brug af både UF- og NF-membraner blev det demonstreret, at

ZLD og mineralgenvinding kunne opnås. UF-membraner gav konsekvent højere vandgennemstrømning end NF-membraner. Eksperimenter viste desuden, at sammensætningen af ”sweep”-gassen påvirkede både vandflux og de udfældede krystallers karakter; CO_2 som ”sweep”-gas fremmede især udfældning af karbonater. Processen udviste fremragende stabilitet ved høje saliniteter (30–150 g/L), fungerede kontinuerligt i over 160 timer og opnåede 91,7% volumenreduktion uden ydeevneforringelse under udfældning.

Det femte studie testede perkrystallisering som behandlingsmetode til industrielt spildevand. Resultaterne viste, at ionafvisningen adskilte sig betydeligt i perkrystallisationstilstand sammenlignet med trykdrevne processer med samme membraner. Igen viste perkrystallisering sig som en stabil og pålidelig afsaltningsteknik, der kunne opnå relativt høj flux i scenarier, hvor DCMD ville lide under alvorlig vædning. Selektivitetsforskelle mellem UF- og NF-membraner blev observeret i sammensætningen af de udfældede krystaller, hvilket fremhævede potentialet for forbedret selektivitet.

Et sjette, mindre studie evaluerede perkrystallisering til behandling af bioraffinaderispildevand med højt indhold af suspenderede stoffer (sukkerroe-vaskvand). Processen kørte kontinuerligt i over 600 timer og demonstrerede yderligere robusthed og modenhed. De opsamlede faste stoffer var bemærkelsesværdigt rige på fosfor og understøtter potentialet for ressourcegenvinding sammen med afsaltning.

Samlet set viser resultaterne, at avancerede additivfremstillede membraner og perkrystallisering kan adressere mange af de centrale barrierer, der begrænser eksisterende ZLD-teknologier. VPP–PIPS giver uovertruffen geometrisk frihed, materialetilpasning og mulighed for at skræddersy overfladeinteraktioner, der er afgørende for nukleation og tilskalning. Samtidig tilbyder perkrystallisering en enkel og skalerbar tilgang til afsaltning og ressourcegenvinding uden behov for højtryk eller specialiserede hydrofobe membraner.

Selvom resultaterne er lovende, er der behov for yderligere forskning for at forbedre den mekaniske robusthed og skalerbarheden af 3D-printede membraner, optimere krystallisationsselektiviteten og integrere varmegenvindingsstrategier for at reducere energibehovet.

Overordnet bidrager afhandlingen med nye indsigter og praktiske fremskridt mod realisering af ZLD og brinemining løsninger. Ved at kombinere innovativ membrandesign med procesintensivering gennem perkrystallisering medvirker arbejdet til at skabe fundamentet for næste generations afsaltningsteknologier, der kan adressere både vandmangel, ressourcegenvinding og miljøbeskyttelse parallelt.

Acknowledgement

First and foremost, I would like to thank my supervisor, Prof. Cejna Anna Quist-Jensen, for her invaluable insight, guidance, and positive attitude, helping me navigate this journey as her first Ph.D. student.

I also extend my sincere thanks to my co-supervisor, Prof. Aamer Ali, who offered rigorous perspectives and helped open the doors to academia.

I am grateful to Prof. David Bue Pedersen and his research group for their warm welcome and expertise within additive manufacturing.

I wish to thank Poul Toft Frederiksen, Head of Programme for Research and Learning at the Poul Due Jensen Foundation, for his inspiring perspective on bridging research and industry, and a special thanks to the Poul Due Jensen Foundation itself for funding this Ph.D. project, without their support, this dissertation would not have been possible.

Special thanks to Kristine Wille Hilstrøm and Karen Guldbæk Schmidt from DOTC, whose support through the Radical Innovation Sprint projects provided valuable guidance and funding that helped bring radical ideas in this thesis to life.

I am also very appreciative of Lund University, and especially Prof. Frank Lipnizki, for graciously allowing me to work as part of his membrane group and for our inspiring discussions. A heartfelt thank you to Ahmet Halil Avci for his tutorship while being in the Lund membrane group.

I am ever grateful to my friends and colleagues at Aalborg University for fostering both a great work environment and an excellent after-work culture.

To the students at Aalborg University, your innovative ideas, passion, and drive have made supervising a truly enjoyable and inspiring experience.

I would particularly like to acknowledge Anders Emuel Olsen, who has embodied these qualities and demonstrated a commitment far beyond what was asked. His work and collaboration have been invaluable and have helped to elevate this thesis.

My deep appreciation also goes to my good friend Gustav Simoni, who has been by my side for the past eight years at Aalborg University. Gustav, along with his wife and dear friend Xinxin Chen and their daughters Evelin and Jackie, will always hold a special place in my heart.

Finally, I extend my gratitude to all my friends, family and my partner Ana Maria Bratovianu, who through ups and downs, health and illness, have stood by me with patience and understanding.

“C,LKJJJHHHHHHHHHHHHHHHHHHG0020”

- Jackie Chen Simoni, 9 months

List of figures

Figure 1-1: Map of countries by consumption of freshwater for agriculture(orange), domestic(green) and industrial(blue) purposes. (Data: World Bank, [7]) 1
Figure 1-2: Periodic table with 31 critical elements identified by the European commission [17]. 3
Figure 1-3: Illustration of processing chains of domestic brines into critical goods via ZLD. 5
Figure 1-4: Timeline of modern desalination [36]. 7
Figure 1-5: Illustration of size exclusion in membrane filtration. Each section represents different categories of membrane filtration gradually separating different sizes of particles from the feed represented as spheres. 8
Figure 1-6: Illustrations of a: global desalination feedwater and b: distribution of global desalination technologies. (Jones et al. [46]) 8
Figure 1-7: graph of relations between osmotic pressure and brine concentration. B: graph of osmotic pressure and volume reduction of 32g/L seawater. On this blue indicates the limiting concentration of RO and yellow the limit of UHPRO. 10
Figure 1-8: Depiction of an Electrodialysis filtration, with the electrodes at each end and a switching CEM and AEM membranes between the electrodes blocking the baths of anions and cations respectively. 12
Figure 1-9, illustrations of different modes of membrane distillation. I: AGMD, II: SGMD III: VMD, IV: DCMD. 15
Figure 1-10, Illustrations of membrane desalination technologies based on their main respective driving forces. 18
Figure 1-11, Illustrations of Theoretical driving force performance at optimum conditions of ED, RO (80bar), MD and FO (Urea draw solute) as a function of NaCl. 21
Figure 1-12, Illustrations of Theoretical specific energy consumption at optimum conditions of ED, RO and H_{vap} (MD). A: SEC as a function of feed concentration ($R=0.99$, $R_w=0.5$). B: SEC as a function of water recovery factor ($R=0.99$, $C_{NaCl}=35g/L$). C: SEC as a function of solute rejection ($R_w=0.5$, $C_{NaCl}=3.5g/L$). 24
Figure 1-13, Depiction of spontaneous nucleation reached by either solution cooling or increasing concentration (saturating). 31

Figure 1-14, Depiction of a MCr-DCMD system where laminar layer and convective layers are depicted with a dotted line. Concentration polarization is depicted by a line which increases towards the membrane interphase (C_{bulk}-$C_{interphase}$). Temperature polarization is likewise depicted both on the feed side ($T_{f\text{-}bulk}$- $T_{f\text{-}interphase}$) 33
Figure 1-15, Left: Plot of free energy as a function of nucleus radius. Right: different shapes of nucleate crystals Here r and x refers to the radius and length/with of a spherical and a cubic nucleate respectively. 35
Figure 1-16, Plot of free energy of heterogeneous nucleation at different contact angles. 36
Figure 1-17, homogeneous to heterogenous free energy plots as a function of contact angle. With different membrane porosities on the left and different Wenzel roughness on the right. (based on Drioli et Al. [127]) 37
Figure 1- 18, different modes of MCr (illustration based on Aamer et al. [132]). 42

Figure 2-1, Generalized definition of additive manufacturing as a flowchart. 47
Figure 2-2, Illustrations of the 3 most common 3D printing methods and their collegial abbreviations. 48
Figure 2-3, Flowchart of different categories of AM methods based on ISO/ASTM 52900 [162] 50
Figure 2-4, Relationship between resolution and maximum printing area size of different types of 3D printing methods (data from Ge et al. [172]), Note: other VPP(other) is other types of VPP printing methods, such as direct laser and LCD masked VPP. 51
Figure 2-5, of porous 3D printed membrane via VPP-PIPS with special triangular prism topography (Kirkebæk et al. [182]) 52
Figure 2-6. 3 most common VPP methods, laser-VPP(Laser-SLA), masked-VPP(MSLA) and DLP-VPP(DLP-SLA). 55
Figure 2-7, Laser intensity distribution in laser focus “one photon polymerization” and TPP (figure based on Zhou et al [192]). 56
Figure 2-8 Phase inversion simulations of the VPP-PIPS process showcasing the effects of; time before solidification, molecular mobility and polymer concentration on the final membrane structure, based on Soares et al. and remade from Kirkebæk et al. ([182,205]) 58

Figure 2-9, Illustration of controlled membrane geometry, micro structure and molecular structure (Paper[I]) 59
Figure 2-10, Schematic of 3D printing membrane of complex shape via the VPP-PIPS process [A1]. 60
Figure 2-11, Top (a): A DSC curve obtained from a VPP-PIPS membrane. Top (b): TGA (black) and differential TGA of a VPP-PIPS membrane. Bottom: table of mass loss of a VPP-PIPS membrane after 24h submerging in different solvents [A1]. 61
Figure 2-12. Left: a wetted flat sheet VPP-PIPS membrane. Right: Dry VPP-PIPS flat sheet membrane [A1]. 62
Figure 2-13. FTIR spectra highlighting the chemical signatures of the various co-polymerized VPP-PIPS membranes (F0 to F100), along with the corresponding functional groups assigned to the characteristic FTIR absorption peaks. 66
Figure 2-14, Top left: Mean pore diameter as a function of PUA-based ink concentration. Top right: Maximum pore diameter determined by bubble point measurements versus PUA-based ink concentration. Bottom left: Shrinkage and porosity for different concentrations of PUA ink. Bottom right: Permeability of various 3D-printed membranes, ranging from HEMA-based to PUA-based formulations (Illustration from Kirkebæk et al.[213]) [Paper(I)]. 67
Figure 2-15, SEM pictures of cross section and membrane top for VPP-PIPS membranes F0, F50 and F100 (Illustration from Kirkebæk et al.[213])[Paper(I)]. 68
Figure 2-16, A: Tensile strength of different VPP-PIPS membranes copolymerized between HEMA based and PUA based inks. B: TGA decomposition of the same VPP-PIPS membranes (Illustration from Kirkebæk et al.[213])[Paper(I)]. 70
Figure 2-17, Left: Contact angle of different compositions of Ink one and two. Right: Contact angle of different compositions of ink two and three. Highlighting the full range of tune ability between hydrophilic and hydrophobic (Illustration from Kirkebæk et al.[213]) [Paper(I)]. 71
Figure 2-18, Hydrophobic VPP-PIPS membranes with AM printed micro topography produced by DLP and pure ink three. A: Contact angle of different layer hardening time. B: picture of water droplet on 200ms membrane. C, D, E, F and G are top pictures of STD, 1600ms, 800ms, 400ms and 200ms respectively (Illustration from Kirkebæk et al.[213]) [Paper(I)]. 72

Figure 2-19. Illustration of assembly of tubular VPP-PIPS membrane in a 3D printed housing for DCMD module [Paper(II)]. 75
Figure 2-20, A: picture of a VPP-PIPS tubular membrane design on a detachable build plate. B: A dried VPP-PIPS tubular membrane fully stable, with a picture depicting its water contact angle. C: FTIR signature of the membrane showcasing the membrane signature and successful polymerization of tBA and TMPTA [Paper(II)]. 76
Figure 2-21, A, B, C and F: Different SEM pictures of a cross-section of an M-40 membrane at different zooms. E: Image-J pore size analysis of the M-40 membrane. F: porosity of M-40, M-50 and M-60 membrane. G: Contact angles of discs made in under same conditions as M-40, M-50 and M-60, Top and plate sides refer to the side facing upward and the side attached to the build plate respectively [Paper(II)]. 78
Figure 2-22, A: TGA (Black) and DSC (Red) of a piece of M-40 membrane. B: Tensile strength of M-40 (red), M-50 (orange) and M-60 (green). C Youngs modulus of same membranes. D: the same membranes Yield strength (orange) and yield strain (green) [Paper(II)]. 79
Figure 2-23, Left is DI-water flux of M-40 and M2 membrane at 60°C (green), 70°C (red) or 80°C (orange). Right, graph of membrane permeability (K) of M-40 and M2 at 60°C (green), 70°C (red) or 80°C (orange) [Paper(II)]. 81
Figure 2-24. A: Flux (Black) of a M-40 membrane at different NaCl as well as a theoretical (solid red) and experiment (dotted red) flux decline in percentages depending on NaCl concentrations. B: flux graphs of M-40, M-50 and M-60 membranes. C: Membrane flux of membranes with different inner tubular diameters.. 82
Figure 2-25. A: Comparison of performance between 3D printed VPP-PIPS membrane and a 0.2µm Pall PTFE membrane in the form of a DCMD experiment at 80ºC and 100g/L. B: Permeate conductivity of the two membranes showcasing wetting of the 0.2µm Pall PTFE membrane. C: Long term experiment of M-40 at 80ºC and a starting salinity of 250g/L. Black line depicts membrane flux and red line the permeate conductivity. Picture of produced NaCl crystals is depicted at the point of crystallization [Paper(II)]... 84
Figure 2-26: Key steps involved in making the inherently integrated spacers on commercial membranes. 87
Figure 2-27. Top: illustration of different spacer names P, A and S and their subsequent dimensions. Middle: CFD simulations of membranes with either

a P, A and S spacer. Bottom: Picture of P membrane (pristine) and membranes with VPP-PIPS produced spacers, A1 (non-porous arrow), A2(porous arrow) and S1 (porous square) spacer [Paper(III)]. 88
Figure 2-28: Crossflow system with a sterlitech crossflow cell, two pressure meters, a pump, feed tank, scale and online data-logging system [Paper(III)]. 89
Figure 2-29. SEM pictures of P, A1 and A2 at 25x, 1000x and 4000x zooms [Paper(III)]. 90
Figure 2-30. A: pore size distribution of A1 (blue), A2 (black), S (green) and P (red). B: Resulting mean pore size of A1, A2, S and P membranes. C: Thickness of membrane (green) and membrane + spacer (orange) of A1, A2, S and P membranes as well as their porosities on the second y-axis. 91
Figure 2-31, A: graph of actual permeability of a 5g/L yeast feed solution over volume reduction for P (gray), A1 (red) and A2 (blue). B: Relative permeability over volume reduction for P (gray), A1(red) and A2 (blue). Bottom: depicts, yeast retentate concentration (yellow axis) and membrane yeast rejection (grey axis) of the different membranes as well as before and after pictures at the filtration start and end [Paper(III)]. 93
Figure 2-32. A: pictures of fouling layer on P, A1 and A2 membranes after 5g/L yeast filtration. B, C, D and E: depicts comparisons between A2 membrane fouling patterns and CFD simulations [Paper(III)]. 94
Figure 2-33. Top: CAD of membrane topography. Bottom:Pictures of different hydrophobic (ink three) VPP-PIPS printed topologies on 0.2µm Pall PTFE membrane with different patterns [A2]. 96

Figure 3-1, illustration of percrystallization with flow through the membrane, and selective rejection of red solute. 102
Figure 3-2, schematic of fully 3D printed percrystallization module, fully assembled – disassembled and picture of module with membrane respectively. 105
Figure 3-3, Illustration of percrystallization using sweeping gas. Sensors pumps and other unit operations are depicted as well as the three cycles, sweeping gas(grey), feed(red) and cooling(blue). 106
Figure 3-4. Left: Bar graph of pure water flux for a UF (green) and NF (orange) membrane at different inlet temperatures. Right: The Vapor pressure(black) and overall permeability(red) of the UF and NF membrane. [Paper (V)] 109

Figure 3-5. Top left: Water flux of NF99HF membrane in percrystallization mode using seawater. Top right: Temperature and humidity of input and outlet streams in the percrystallization experiment. Bottom picture: Pictures of permeate side of the membrane in chronological order. [Paper (IV)] ... 110
Figure 3-6, desalination of seawater with UF membrane ETNA01PP and NF membrane NF99HF. Top picture depicts membrane surface on the permeate side at the beginning and end of the run. [Paper(IV)] 112
Figure 3-7, Top graphs are of water flux (orange) and drymatter flux (green) at different compressed air used as sweeping gas at different flows. Top Right: humidity of the sweeping gas at different compressed air flows. Bottom graphs depicts similar but for CO_2 gas as sweeping gas. [Paper(IV)] 114
Figure 3-8: Top: XRD graphs of the produced crystals from the percrystallization experiments at different Compressed air flow and different CO_2 gas flows. Clear Carbonate peaks occur more prominently when CO_2 is utilized (arrows at prominent $CaCO_3$ 14.5° peak). Bottom: Bar graph of membrane rejection of the components Mg, Ca, Mg and Li at the different sweeping gas compositions and flows [Paper(IV)] 116
Figure 3-9, Plot of water flux (green) and feed conductivity (red) of an seawater desalination experiment with 5 cycles of refilling reaching 91.7% volume reduction. Pictures of permeate side of membrane at different time are depicted, at 71.8h both before and after crystal recovery is shown [Paper(IV)]. 118
Figure 3-10, Left: Drymatter flux between each feed refilling cycle. Right: Relative weight percentage of Ca, Mg, Li and Na in the precipitating crystals at different pH treatment cycles [Paper(IV)]. 119
Figure 3-11: Process diagram illustrating seawater treatment, beginning with the percrystallization step in a crystallizer, followed by pH adjustment using NaOH. Process streams are shown in blue, direct outputs in green, indirect outputs in purple, and inputs in orange [Paper(IV)]. 120
Figure 3-12. Water flux Percrystallization of color water from anodized wastewater industry using either an UF or NF membrane. Bottom pictures are permeate side of the membranes in chronological order from start to midway to end experiment. [Paper(V)].. 123
Figure 3-13: Top: Flux (red) and permeate conductivity of a DCMD experiment on color wastewater as a function of volume reduction (Olsen et al. [301]) Bottom Left: Permeability (black), membrane resistance (red) and cake resistance (blue) of pressure filtration with NF membrane. Bottom

right: Permeability (black), membrane resistance (red) and cake resistance (blue) of pressure filtration with UF membrane [Paper(V)]. 124
Figure 3-14. Left: Membrane rejection in percrystallization and pressure driven system for Cr, Cu, color compound and drymatter. Right: XRD graph of percrystallization crystals for either UF or NF membrane. Nb: PCr=percrystallization and P=pressure driven [Paper(V)]. 126
Figure 3-15. Picture of sugar beet wash water from Nordzucker plant Nakskov, Denmark, depicting high concentration of suspended solids [A3]. 128
Figure 3-16: Plot of water flux (black) and feed conductivity (red) of sugar beet wash water desalination experiment over 600h with 13 cycles of refilling reaching 96% volume reduction. Additionally, a picture of membrane surface after experiment with crystals. [A3]. 129
Figure 3-17, Permeability of VPP-PIPS, 3D printed disks with different thicknesses, showcasing the control of liquid flow (Kirkebæk et, al. [182].) 133
Figure 3-18, VPP-PIPS printed MF membranes, left: full membrane module and membrane with precipitating NaCl crystals. Right: 3D printed membrane topography a, b, c and d pictures of precipitation over time (Steen A, et Al. [321]). 134

List of tables

Table 1-1: Qualitative estimation of RO, NF, FO, ED and MD for ZLD and brine mining. The (*) scoring system is; (*) not suitable, (**) Technically possible but with some challenges, (***) Suitable. 27

Table 2-1, Ink compositions of different VPP-PIPS produced membranes copolymerized between (hydrophilic ink one, flexible ink two and hydrophobic ink three (Table from Kirkebæk et al.[213]) [Paper(I)]. 64
Table 2-2, Naming of different tubular membranes depending on their Inner diameter, Ink/porogen composition and cross section type. Bottom picture depicts the different Cross section types [Paper(II)]. 74
Table 2-3, Table of inlet feed temperatures (T_f) and permeate temperature (T_p), For membranes M-40 and riffled M2 setup in a DCMD setup running DI-water at either 60°C, 70°C or 80°C [Paper(II)]. 80

Table 3-2, Alfa Laval membranes used in these studies and their specifications [Paper IV] 107
Table 3-1, Na, Ca, Mg and Li composition of the seawater from Hanstholm harbor, coast of Denmark at the North sea. 107
Table 3-3, Composition of spent anodized color water from DAI (Olsen et Al. [301]) 121
Table 3-4, Table of desalintation types compared to percrytallization results (Process type, membrane type, flux, permeabillity, Volume reduction/operation time) 131

Abbreviations

MED – Multi effect distillation
MSF – Multi stage flash distillation
NIPS – Non-solvent induced phase separation
TIPS – Temperature induced phase separation
VIPS – Vapor induced phase separation
UPW – Ultrapure Water
ZLD – Zero Liquid Discharge
RO – Reverse Osmosis
MCr – Membrane Crystallization
AM – Additive Manufacturing
VPP – Vat Photopolymerization
PIPS – Polymerization-Induced Phase Separation
DCMD – Direct Contact Membrane Distillation
PFAS – Per- and Polyfluoroalkyl Substances
UF – Ultrafiltration
NF – Nanofiltration
MD – Membrane Distillation
AGMD – Air Gap Membrane Distillation
SGMD – Sweeping Gas Membrane Distillation
VMD – Vacuum Membrane Distillation
LEP – Liquid Entry Pressure
ED – Electrodialysis
CEM – Cation Exchange Membrane
AEM – Anion Exchange Membrane
FO – Forward Osmosis
MF – Microfiltration
UHPRO – Ultra-High Pressure Reverse Osmosis
SEC – Specific Energy Consumption
SI – Saturation Index
IAP – Ionic Activity Product
CNT – Classical Nucleation Theory
VPP–PIPS – Vat Photopolymerization – Polymerization Induced Phase Separation
CAD – Computer-Aided Design
FFF – Fused Filament Fabrication
FDM – Fused Deposition Modelling
MEX – Material Extrusion
MJT – Material Jetting

LOM – Laminated Object Manufacturing
PBF – Powder Bed Fusion
SLS – Selective Laser Sintering
DED – Direct Energy Deposition
BJT – Binder Jetting
TPP – Two-Photon Polymerization
SLA/SL – Stereolithography
DAI – Dansk anodiserings industri – Danish anodizing industry
CFD – Computational fluid dynamics
XRD – X-ray diffraction
SEM – Scanning electron microscopy
HEMA – 2-hydroxyethylmethacrylate
tBA – tert-butyl acrylate
PUA – Polyurethane acrylate
TPP – Two photon polymerization
1PP – one photon polymerization ATR-FTIR
ATR-FTIR – one photon polymerization ATR-FTIR
DSC-TGA – Differential scanning calorimetry – Thermogravimetric analysis
CA – Compressed air

Variables

γ – Surface tension
θ – Contact angle
β – Shape factor
r – Pore radius
P – Pressure
P_{feed} – Feed side pressure
$P_{permeate}$ – Permeate side pressure
A, B, C – Antoine constants
a_w – Water activity
P_* – Corrected partial pressure
x_w – Water molar fraction
l_w – Activity coefficient
v – Cumulative valence of ions
R – Ideal gas coefficient
T – Temperature
c – Concentration

c_p – Permeate concentration
c_f – Feed concentration
c_b – Brine concentration
R_w – Water recovery factor
π – Osmotic pressure
SEC – Specific energy consumption
ΔH_{lat} – Latent heat of evaporation
R – Rejection coefficient
K_{sp} – Solubility product constant
G – Gibbs free energy
R_n – Nucleation rate
Z – Zeldovich factor
j – Molecule attachment rate
ρ – Number of nucleation sites
k_b – Boltzmann constant
t_i – Induction time
J – Flux
C – Concentration
A_s – Transfer coefficient (solute)
B_t – Transfer coefficient (temperature)
V – Molar volume
A – Interfacial area
ε – Porosity
r_w – Wenzel roughness
I – Photoinitiator
hv – photons
R – Photoinitiator product
M – Monomers
n – Monomers molar amount
χ_{12} – Solvent polymer interaction parameter
ϑ – Polymer molar volume
M_{CH} – Molecular mobility
$F(c)$ – Total system free energy
κ – interfacial constant
μ – Dynamic viscosity
L – Membrane thickness
k – Permeability coefficient
B_{vap} – Vapor permeability
K_s – Sorption constant
D – Diffusion constant

Table of Contents

Preface I
English Summary III
Resume in Danish VII
Acknowledgement XI
List of figures XIII
List of tables XX
Abbreviations XXI
Variables XXII
Chapter 1. Introduction 1
  1.1. Water resources 1
  1.2. Water desalination 2
  1.3. Brine mining 3
  1.4. Desalination technology 5
  1.5. Membrane desalination methods 11
    1.5.1 Electrodialysis 11
    1.5.2 Forward osmosis 12
    1.5.3 Membrane distillation 14
  1.6. Comparison of membrane desalination methods 17
    1.6.1 Limiting concentration 19
    1.6.2 Energy consumption 21
    1.6.3 (Ion)Selectivity 25
    1.6.4 Comparison 27
  1.7. MCr 29
    1.7.1 Crystallization 29
    1.7.2 Temperature/concentration induced crystallization 32
    1.7.3 Solute-membrane interaction 34
    1.7.4 Directions of MCr 38

1.8. Scope summary and objectives 43
1.9. Thesis content 44
  1.9.1 Included works 44
  1.9.2 Other included works 45

Chapter 2. Additive manufacturing 47
2.1. AM Principle 47
2.2. VPP-PIPS 53
  2.2.1 Vat Photopolymerization (VPP) 53
  2.2.2 VPP methods 54
  2.2.3 VPP materials 56
  2.2.4 Polymerization induced phase separation (PIPS) 57
  2.2.5 VPP-PIPS membranes 59
2.3. Tunable physicochemical properties via VPP-PIPS copolymerization 63
  2.3.1 Materials and methods 63
  2.3.2 Results and discussion 65
  2.3.3 Effects of Copolymerization on membrane properties 66
  2.3.4 Tuning of membrane physiochemical properties via Copolymerization 69
  2.3.5 Enhancing hydrophobicity via 3D printed topography 71
  2.3.6 Summary 73
2.4. Fully 3D printed VPP-PIPS membranes for MD/MCr 73
  2.4.1 Materials and methods 73
  2.4.2 Membrane characteristics 75
  2.4.3 Membranes for DCMD MD/MCr 79
  2.4.4 Summary 85
2.5. Enhancing membrane properties with VPP-PIPS topography 85
  2.5.1 Porous spacers through VPP-PIPS 85
  2.5.2 Materials and methods 86

2.5.3 VPP-PIPS inherent spacer characteristics.................................. 89
2.5.4 MF performance with VPP-PIPS made spacers 92
2.5.5 Porous spacers printed for MD/MCr... 95
2.5.6 Summary 96
2.6. Summary and Perspectives of AM for membranes and MD/MCr.... 97
Limitations and future.. 97
Chapter 3. Percrystallization.. 99
3.1. Percrystallization principles (Permeation, Evaporation, Crystallization)... 99
3.2.1 Future of percrystallization 104
3.2. Our Percrystallization method 104
3.3. Percrystallization for Seawater desalination 106
3.3.1 Materials and methods 106
3.3.2 Percrystallization characterization 107
3.3.3 Preliminary seawater testing 109
3.3.4 Membrane selection 111
3.3.5 Sweeping gas flow and composition... 112
3.3.6 Full continuous ZLD seawater desalination system with mineral recovery... 116
3.3.7 Summary 119
3.4. Percrystallization of industrial wastewater (anodizing industry).... 120
3.4.1 Materials and methods 121
3.4.2 Waste water treatment.. 122
3.4.3 Process selectivity 125
3.4.4 Summary 126
3.5. Percrystallization of food industry wastewater (Sugar-beet washwater) 127
3.5.1 Wash water processing.. 127
3.5.2 Summary 130

3.6. General summary and perspective on percrystallization 130
Limitations and Future Perspectives 132
Chapter 4 Expanded thesis summary 135
Chapter 5 Future works 137
Chapter 6 Other works 139
6.1. Published works 139
6.2. Conference Proceedings.. 140
Literature list 141
Appendices 191

Chapter 1. Introduction

1.1. Water resources

Water is a vital resource for society, supporting industry, agriculture, and potable drinking supplies. Global demand is steadily increasing and is projected to be ever increasing [1–3]. For this reason, water has been designated as the sixth Sustainable Development Goal by the United Nations [4]. Although 71% of the Earth's surface is covered by water [5], only about 3% is suitable for human consumption [6]. According to the World Bank, just 13% of freshwater is used for domestic purposes, 15% for industry, and 72% for agriculture. In industrialized regions, the share of water used by industry is disproportionately higher, accounting for 20.1% in China, 43.6% in the European Union, and 47.2% in the United States [7]. As economies develop, industrial demand for freshwater grows alongside essential agricultural and domestic needs.

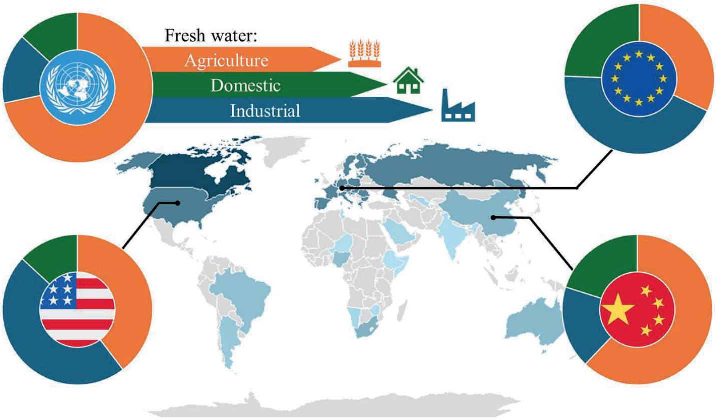

Figure 1-1: Map of countries by consumption of freshwater for agriculture(orange), domestic(green) and industrial(blue) purposes. (Data: World Bank, [7])

Modern industries also contribute significantly to the rising demand for highly purified water. Data centers, pharmaceutical manufacturing, semiconductor fabrication, and emerging green fuel production processes, such as ammonia, methanol, and hydrogen synthesis, all require ultrapure water (UPW), characterized by mineral concentrations up to 250 times lower than those in potable water [8]. The UPW market was estimated to be a billion USD industry by 2022 and is projected to grow 59% by 2027 [9]. Consequently, access to fresh and ultrapure water is not only essential for sustaining human life and agricultural production but is also critical to the continued development of the energy, pharmaceutical, and other high-tech sectors.

1.2. Water desalination

To meet the growing demand for high-quality water driven by global industrialization and population growth, it is necessary to adopt measures such as desalination, which can unlock the remaining 77% of the global water supply for consumption, or the re-purification of waste brines for reuse. However, while desalination effectively removes dissolved minerals to produce purified water, it simultaneously generates concentrated brine waste. According to Panagopoulos et al. [10], conventional desalination processes typically achieve only ~40% water recovery, leaving ~60% as highly concentrated waste brine. These residual brines cannot simply be discharged into lakes or marine environments, as doing so would have severe adverse impacts on local ecosystems [11]. This challenge is recognized as a global environmental issue and is reflected in the United Nations' 14th Sustainable Development Goal, which emphasizes the protection of marine life [12]. Managing concentrated waste is a critical concern not only for treating municipal and industrial wastewater but also for seawater and brackish water desalination. In response, industries and regulatory authorities are adopting stricter discharge standards and exploring advanced waste management strategies such as minimum liquid discharge (MLD) and zero liquid discharge (ZLD). Both approaches aim to minimize liquid waste by recovering as much water as possible; ZLD, in particular, achieves the complete separation of solids from water. While the solid residues produced by ZLD can still pose environmental hazards, their concentrated form facilitates storage, disposal, and potential valorisation, creating new opportunities to offset the costs of desalination.

1.3. Brine mining

In addition to global water scarcity, society also faces an impending shortage of valuable minerals and metals. As technological and economic development progresses, the demand for both metallic and non-metallic resources continue to grow [13]. However, these elements are unevenly distributed across the globe, meaning that a country's geographic size and location can strongly influence its access to critical raw materials. Historically, competition over resources has contributed to international conflicts. For example, the European Union was founded in part on a common market for steel and coal to help prevent future international conflicts [14,15]. To ensure the long-term availability and self-sufficiency of essential materials, the EU launched the Raw Materials Initiative [16]. The European Commission has since identified 70 critical resources, which include 31 individual elements as well as all rare earth elements [17].

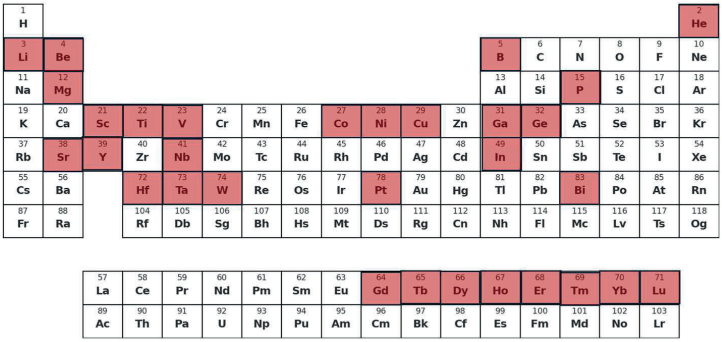

Figure 1-2: Periodic table with 31 critical elements identified by the European commission [17].

In response to this rising demand, the European Commission is actively identifying potential sources of critical raw materials within the EU. While geological deposits remain one option, they are relatively scarce and can be depleted rapidly. An alternative source is brines, which are abundant and may contain a wide range of elements. These brines originate from both natural and industrial processes, contributing to the circular economy through “brine mining” [18–21].

Magnesium (Mg): Magnesium is a vital material used in transportation, electronics, packaging, and construction. Seawater is particularly rich in magnesium, where it is the third most abundant cation, with an approximate concentration of 1.3 g/L. This equates to roughly 1.3 kg of magnesium per cubic meter of desalinated seawater [22]. Given that the EU imports approximately 120,000 tonnes of magnesium annually [23] and possesses a desalination capacity of 8.7 million m^3 per day [24], transitioning desalination plants to zero liquid discharge (ZLD) could theoretically recover the entire annual magnesium import within 10–11 days.

Phosphorus (P): Phosphorus is another critical resource, essential for fertilizers as well as chemical and defense manufacturing. It is also recognized as a water pollutant, prompting strict regulations on its discharge. Municipal wastewater represents a significant potential source, containing up to 16 mg/L of phosphorus [25,26]. Considering that the average EU farmer applies 7.6 kg of mineral phosphorus per hectare annually, treating approximately 475 m^3 of wastewater with ZLD technologies could yield enough phosphorus to meet this requirement for one hectare each year.

Lithium (Li): Lithium is increasingly important, especially for battery production, alongside its established uses in ceramics and metallurgy [19]. In 2023, the EU imported 1,712 tonnes of pure lithium, primarily in the form of lithium carbonate (Li_2CO_3) [27]. Recent studies have reported that some European brines contain lithium concentrations ranging from 150 to 400 mg/L [28,29]. Desalinating between 4.8 and 11.4 million m^3 of these brines annually via ZLD could substantially improve the EU’s lithium self-sufficiency.

Magnesium, phosphorus, and lithium illustrate how ZLD desalination can simultaneously provide a sustainable water supply and reduce dependence on foreign raw materials by recovering critical elements from domestic brine sources. In fact, most elements can be found in wastewater and brines [29,30], although in some cases concentrations are too low to justify recovery.

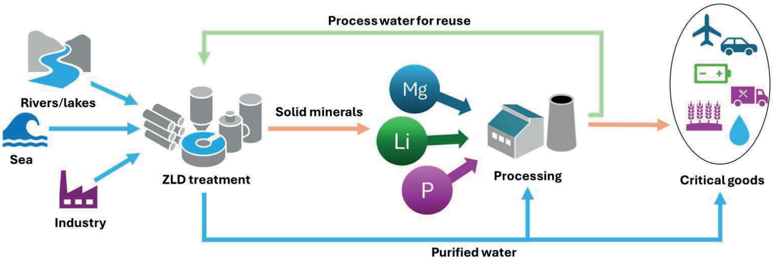

Figure 1-3: Illustration of processing chains of domestic brines into critical goods via ZLD.

1.4. Desalination technology

In order to achieve zero liquid discharge (ZLD) and enable the recovery of both minerals and water from diverse waste streams, it is essential to understand the available desalination technologies as desalination plays a central role in ZLD implementation. Over the years, numerous desalination methods have been developed [31]. Traditionally, evaporation-based desalination has been practiced for millennia. Examples include, solar ponds, large shallow basins exposed to sunlight, heat water to induce evaporation, leaving the dissolved minerals behind. Although solar ponds rely on renewable thermal energy, they offer limited process control and since the water must remain continuously exposed to the sun, these systems require substantial land area, and collecting the generated vapor is difficult or infeasible [32]. Distillation is another thermal desalination approach distinguished from solar ponds by its active condensation of vapor. In traditional setups, brine is heated in a vessel, and the resulting vapor condenses in a cooled tube known as a condenser which unlike solar ponds make the water easily collectable [33]. However, simple distillation has high energy demands; even under ideal conditions, it consumes a minimum energy equivalent to the latent heat of evaporation, approximately 619.4 kWh/m^3. Moreover, this energy is typically supplied by combustion or electrical heating rather than renewable sources, such as solar [34].

While basic distillation remains an effective means of producing high-purity water, it was not until 1880–1928 that industrial-scale distillation became widespread. This was followed by the introduction of multi-effect distillation (MED) in 1930 and multi-stage flash distillation (MSF) in 1957, which significantly reduced overall energy consumption [31].

In MED, the first stage heats a feed such as seawater. The vapor generated condenses inside heat exchange coils, transferring heat to the next stage ultimately recovering some of the latent heat of vaporization. This sequential process continues across multiple stages for effectively recovering as much heat as possible making MED much more energy efficient than simple distillation [35].

MSF operates on a different principle, relying on flash evaporation. The feed solution, e.g., seawater, is first heated under pressure to prevent boiling. When the pressurized, superheated liquid passes through a thermal expansion valve, the sudden pressure drop causes instantaneous adiabatic flash evaporation, generating a substantial amount of vapor. Like in MED, the feed solution also serves to condense the vapor in successive stages to recover most of the latent heat of vaporization [31].

Because both MED and MSF recover latent heat from condensation, they are far more energy efficient than simple distillation. Energy consumption ranges from approximately 14.45–21.35 kWh/m^3 for MED and 19.85–27.25 kWh/m^3 for MSF, according to Al-Karaghouli and Kazmerski [35]. This represents a dramatic improvement compared to the 619.4 kWh/m^3 required by single-stage distillation.

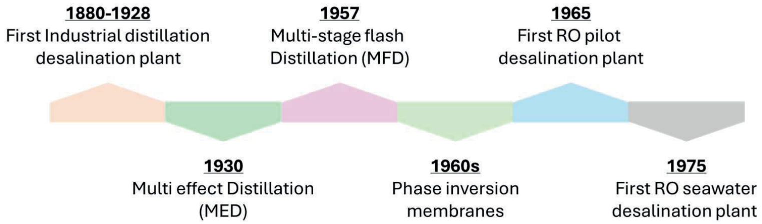

Figure 1-4: Timeline of modern desalination [36].

Physical separation methods, such as filtration, have been used for nearly as long as distillation and were historically applied in desalination using sand filtration columns [35]. More recently, in the 1960s, filtration membranes were developed based on the phase inversion of dissolved polymers. This process involves rapidly decreasing polymer solubility, either by introducing a non-solvent (NIPS), lowering the temperature (TIPS), or evaporating the solvent (VIPS) [37,38].

Phase inversion membranes revolutionized filtration technology and filtration membranes quickly became popular for water treatment due to their high energy efficiency, low chemical requirements, compact footprint, and operational simplicity [39–41]. A key advantage is their selectivity through size exclusion, determined by their tunable pore size. Membrane pore sizes are typically classified as follows: microfiltration (MF; ~1000–100 nm), ultrafiltration (UF; ~100–10 nm), nanofiltration (NF; ~10–1 nm), and reverse osmosis (RO; <1 nm). The separation capability generally correlates with pore size: MF and UF can remove large colloids and macromolecules respectively, whereas NF and RO can reject dissolved divalent ions and all ions respectively while allowing water to permeate, thereby achieving desalination of the feed solution [42].

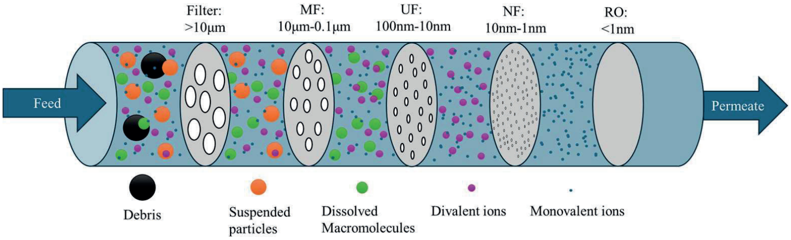

Figure 1-5: Illustration of size exclusion in membrane filtration. Each section represents different categories of membrane filtration gradually separating different sizes of particles from the feed represented as spheres.

Reverse osmosis (RO) offers a significant advantage over thermal desalination methods due to its substantially lower energy consumption. RO typically requires 2–6 kWh/m³, representing a reduction of more than 80% compared to the most efficient thermal desalination process, multi-effect distillation (MED) [43,44]. In addition, RO systems can be configured with high packing density and exhibit nearly linear scalability between applied pressure and water output. These attributes have contributed to RO becoming the most widely adopted desalination technology worldwide, accounting for more than 69% of global desalination capacity [45].

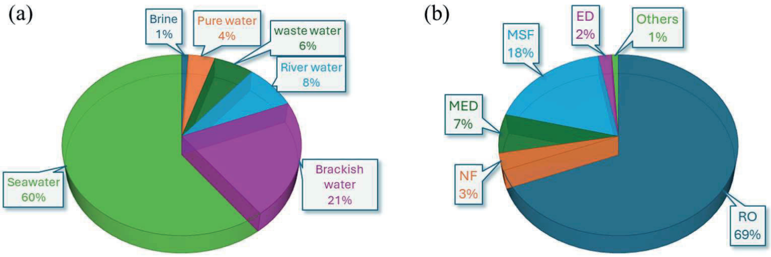

Figure 1-6: Illustrations of a: global desalination feedwater and b: distribution of global desalination technologies. (Jones et al. [46])

However, RO also posses several limitations compared to simple distillation, including low thermal and chemical stability and a pronounced tendency toward membrane fouling which ultimately lowers filtration throughput [47,48]. Membrane fouling is an inherent consequence of size exclusion, occurring when solutes accumulate on the membrane surface. This accumulation reduces mass transport and ultimately decreases permeate flux and water output [49,50].

To maintain membrane performance, pretreatment is often required to cool the feed stream and to remove harmful pollutants such as chlorine and suspended particles [51]. While chlorine is typically neutralized with chemical dosing, suspended solids are removed by pre-filtration steps such as sand filtration, microfiltration (MF), and ultrafiltration (UF). These additional processes increase system complexity and operational costs, in some cases accounting for more than two-thirds of total desalination expenses [52,53].

Another significant limitation of RO, particularly when processing high-salinity feed streams, is osmotic pressure. As the name implies, reverse osmosis operates by applying hydraulic pressure that exceeds the osmotic pressure created by dissolved solutes [54]. This pressure differential is relatively easy to achieve when treating freshwater or slightly contaminated streams. However, in seawater and natural brines with much higher salinity, osmotic pressure imposes a practical constraint. Conventional RO systems are typically limited to operating pressures around 80 bar, while newer ultra-high pressure reverse osmosis (UHPRO) units can reach approximately 120 bar. These limits correspond to maximum sodium chloride concentrations of roughly 94 g/L and 140 g/L, respectively, beyond which water recovery becomes unfeasible [54,55].

Seawater itself has a salinity of approximately 32 g/L, corresponding to an osmotic pressure near 27 bar. Under RO or UHPRO operation, the theoretical maximum volume reduction is about 66%–77%, leaving 340–230 liters of concentrate per cubic meter of seawater treated. In practice, the actual recovery is often lower due to concentration polarization effects.

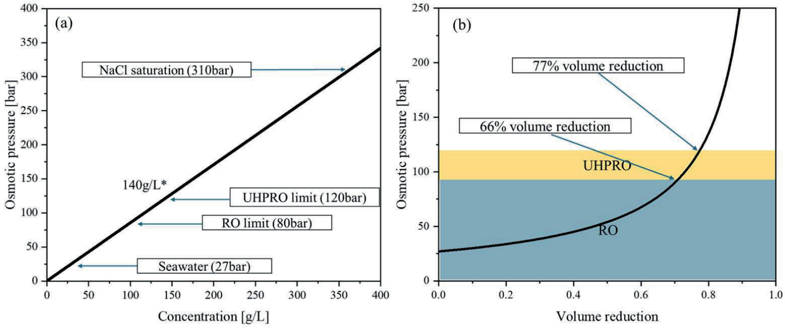

Figure 1-7: graph of relations between osmotic pressure and brine concentration. B: graph of osmotic pressure and volume reduction of 32g/L seawater. On this blue indicates the limiting concentration of RO and yellow the limit of UHPRO.

Although RO is the most widely adopted desalination method, its limitations, particularly osmotic pressure constraints and membrane fouling, mean that it is generally not suitable as a stand-alone process for zero liquid discharge (ZLD) when treating highly concentrated brines [56].

In contrast, thermal processes theoretically do not have a maximum concentration limit; with sufficient thermal energy, all water can eventually be evaporated, as demonstrated by solar evaporators. However, multi-effect distillation (MED) and multi-stage flash (MSF) systems are highly susceptible to corrosion and scaling at elevated salinities. For this reason, operational concentration limits are typically set around 62 g/L [57,58].

The practical disadvantages of MED and MSF at high concentrations are further illustrated by their brine discharge volumes relative to RO. On a global average, when desalinating seawater, MSF and MED produce approximately 3.6 m^3 of waste brine for every cubic meter of desalinated water, whereas RO generates only about 1.4 m^3 [46].

1.5. Membrane desalination methods

Due to the limitations presented in the conventional methods, other membrane methods for desalination have been developed. Four methods (ED, FO and MD) as well as RO will be considered here.

1.5.1 Electrodialysis

Electrodialysis (ED) is an alternative to conventional desalination processes such as RO and thermal methods. ED has been employed for desalination for nearly as long as RO and is recognized as a mature technology, accounting for approximately 2% of global desalination capacity. Unlike RO, which relies on hydraulic pressure, ED uses an electrical potential as the driving force to separate ions. When a voltage is applied across the feed brine, anions migrate toward the anode while cations move toward the cathode. Ion-selective membranes positioned between the electrodes prevent oppositely charged ions from crossing into the wrong compartment. Specifically, cation exchange membranes (CEM) are placed adjacent to the cathode to allow only cations to pass, while anion exchange membranes (AEM) are positioned near the anode to permit only anions. This configuration produces three separate streams: a central feed stream that becomes progressively desalinated as it flows through the cell stack, and two concentrate streams enriched in either cations or anions [59,60].

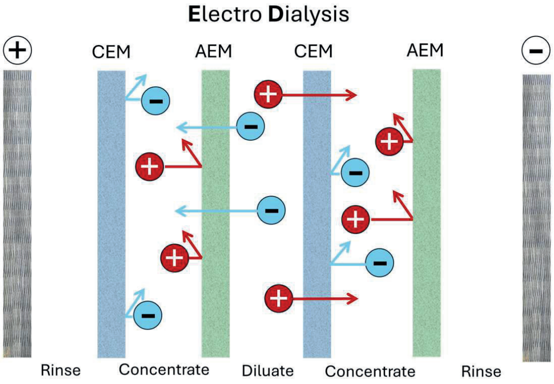

Figure 1-8: Depiction of an Electrodialysis filtration, with the electrodes at each end and a switching CEM and AEM membranes between the electrodes blocking the baths of anions and cations respectively.

1.5.2 Forward osmosis

Forward osmosis (FO) uses the same type of selective membrane employed in RO but reverses the direction of water transport with the osmotic pressure instead of against it. This allows water to move from the less concentrated side toward the more concentrated side.

FO operates by transferring water from the feed solution to what is called a draw solution. For water flux to occur, the draw solution must have lower solvent activity, and therefore higher osmotic pressure, than the feed. This is typically achieved by maintaining a higher solute concentration on the draw side. As water selectively moves across the membrane, the draw solution becomes diluted while the feed stream is concentrated. Since FO acts with the osmotic pressure, unlike RO, FO is not limited by the need to overcome osmotic pressure via applied hydraulic pressure and can achieve much higher feed concentrations, depending on the draw solution composition. For example, McGinnis et al. [61] demonstrated that FO can concentrate brines to approximately 180 g/L.

However, as the draw becomes diluted and the feed becomes concentrated, osmotic equilibrium will eventually be reached, halting water transport. This limitation means that FO alone is not a continuous desalination process.

To address this constraint, several strategies have been developed to reconcentrate the draw solution while processing the feed. One approach involves continuously adding more solutes to the draw, though this is generally inefficient and wasteful. Another strategy couples FO with a thermal desalination step to reconcentrate the draw solution [62]. However, for applications aiming to achieve ZLD, adding thermal desalination after FO can be counterproductive, as it effectively shifts the desalination burden back to a thermal process and adds complexity.

Research into reactive draw solutes offers promising alternatives that could reduce or eliminate the need for energy-intensive draw reconcentration. These include:

- **Nanoparticles**, which can be separated or reconcentrated by simple MF/UF filtration or magnetic recovery [63,64].

- **Thermolytic or thermoresponsive solutes**, which can be removed from the draw by heating and then reintroduced upon cooling to restore osmotic pressure [65,66].

Regarding energy consumption, FO is highly dependent on the downstream treatment of the draw solution. While the specific energy consumption of the FO step itself is very low (Mazlan et al. [67] reported values as low as 0.11 kWh/m^3 for seawater), post-treatment of the diluted draw solution, especially via thermal desalination, can be highly energy-intensive. Although the principle has been known as long as RO and has been used in niche applications such as emergency seawater desalination since the late 20th century [68], FO has only gained broader traction as a desalination method over the past two decades [69].

1.5.3 Membrane distillation

None of the previously discussed desalination methods match the robustness of thermal processes such as MED and MSF. However, a major limitation of these systems is their large physical footprint. In contrast, membrane technologies can significantly increase the effective area for water transport. For example, in RO systems, the packing density, defined as membrane area per unit module volume, can range from approximately 100 m^2/m^3 in plate-and-frame configurations to over 1,000 m^2/m^3 in spiral-wound modules [70].

Membrane distillation (MD) combines the thermal driving force of evaporation with the modular scalability of membrane technology. Unlike RO, NF, UF, and MF, which rely on applied hydraulic pressure, or processes such as ED and FO, which exploit electrical or osmotic gradients, MD uses a vapor pressure gradient as the driving force for separation.

In MD, a hydrophobic microporous membrane physically separates the feed and permeate streams, allowing only water vapor to pass through while retaining non-volatile solutes such as dissolved ions. Consequently, MD selectivity is governed by the partial vapor pressures of the solvent and solutes, similar in principle to MED and MSF.

To prevent unwanted liquid penetration through the membrane pores, the system must maintain a minimum liquid entry pressure (LEP) exceeding 0.5 bar to be practically effective [71]. The LEP is determined by the membrane's pore size and surface hydrophobicity (contact angle) as described by the following equation (1-1):

$$LEP = -2\gamma * \frac{\beta * \cos(\theta)}{r} \tag{1-1}$$

In this correlation θ is the contact angle, β is a pore shape factor, γ is the surface tension and r the pore radius. An MD membrane therefore must be dry and hydrophobic with a contact angle higher than >90° for it to function properly.

When the vapours are carried through the membrane, they are condensed on the permeate side. The method of condensation defines which configurations the MD is run at. There are four popular configurations in MD, airgap (AGMD), sweeping gas (SGMD), vacuum (VMD) and the most popular direct contact (DCMD) [72,73]. The different modes are shown in Figure 1-9.

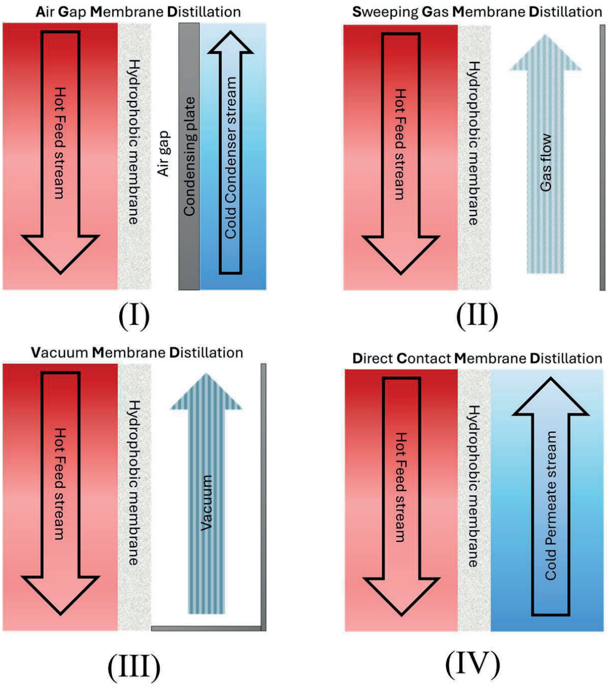

Figure 1-9, illustrations of different modes of membrane distillation. I: AGMD, II: SGMD III: VMD, IV: DCMD.

I) Air Gap Membrane Distillation (AGMD) (Figure 1-9)
In AGMD, an air gap is situated on the permeate side, separating the membrane interface from a cooled condensing surface. Water vapor passing through the membrane diffuses across the air gap and condenses on the cold plate, maintaining the air gap in a dry state and sustaining the vapor flux.

II) Sweeping Gas Membrane Distillation (SGMD) (Figure 1-9)
Similar to AGMD, SGMD also features an air-filled permeate side. However, in SGMD, a continuous flow of dry sweeping gas (typically air) is introduced across the membrane surface. This gas stream transports the water vapor to an external condenser, where it condenses into distilled liquid.

III) Vacuum Membrane Distillation (VMD) (Figure 1-9)
In VMD, a vacuum is applied to the permeate side, generating a significant pressure differential between the feed and permeate compartments. This enhances vapor transport across the membrane, which is one of VMD's primary advantages. The vapor is then conveyed downstream, similar to SGMD, and subsequently condensed.

IV) Direct Contact Membrane Distillation (DCMD) (Figure 1-9)
DCMD is the most widely used MD configuration due to its operational simplicity. In this mode, the permeate side contains a chilled liquid solvent, typically pure water. The temperature difference between the hot feed and the cold permeate stream drives vapor migration across the membrane, where it condenses directly into the cooling liquid. This mode typically offers higher condensation efficiency compared to other MD configurations.

Regardless of the configuration employed, the driving force in MD is the vapor pressure gradient between the feed and permeate streams, expressed as (Equation (1-2)):

$$\Delta P = \mathrm{P}_{feed} - P_{permeate} \tag{1-2}$$

The vapor pressure is highly dependent on the temperature can be calculated with the Antoine equation (1-3):

$$\log_{10}(P) = A - \frac{B}{T + C} \tag{1-3}$$

Here P it the vapor pressure, T is the water temperature, A, B and C are empirical constants and depends on the units of P and T [74]. Although thermal desalination methods are capable of handling much higher solute concentrations than non-thermal processes, the vapor pressure, and consequently the driving force for desalination, is influenced by solute concentration. This relationship can be described by Raoult's law, which defines the water activity coefficient (a_w) as follows (Equation (1-4)):

$$a_w = \frac{P_*}{P} = x_w * l_w \tag{1-4}$$

P_* is the corrected partial pressure, x_w is the mole fraction of water and l_w is an activity coefficient. The partial vapor pressure is therefore linearly related to the concentration and concentrating the feed will lead to a lower driving force[75].

1.6. Comparison of membrane desalination methods

Based on their driving forces, membrane desalination methods can be categorized into different classes, including pressure-driven, thermally driven, electrically driven, and concentration gradient-driven processes (Figure 1-10). As discussed in the previous sections, each method has distinct advantages and limitations depending on its intended application.

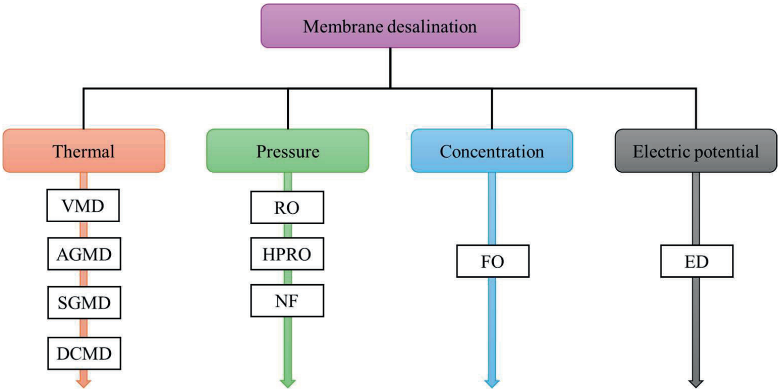

Figure 1-10, Illustrations of membrane desalination technologies based on their main respective driving forces.

In the context of zero liquid discharge (ZLD), desalination processes must be capable of concentrating solutes to the point of solidification. Accordingly, the limiting concentration achievable by a given method must be sufficiently high to meet ZLD requirements. Although this has already been demonstrated in approaches such as evaporation ponds, other considerations are equally important for making membrane desalination methods commercially viable. Marketability is determined by both the cost per volume of treated water and the value of the recovered outputs. Therefore a low energy consumption as possible is prefered and a water output and produced minerals as pure as possible is greatly beneficial for ZLD and brine mining to further generate valuable products.

From this perspective, three primary evaluation parameters can therefore be defined:

1. Limiting concentration
2. Energy consumption
3. (Ion)Selectivity

1.6.1 Limiting concentration

For different applications, varying concentrations must be achieved to reach saturation and thereby enable separation of liquid and solids for ZLD. For example, to precipitate NaCl it requires reaching a concentration of 357 g/L [76].

This requirement imposes significant constraints on processes relying on applied pressure, as osmotic pressure increases linearly with feed concentration. Although RO can feasibly concentrate low soluble minerals such as struvite solutions up to precipitation, concentrating NaCl to saturation becomes much more challenging because the required osmotic pressure exceeds the 80–120 bar operational limits of conventional RO. Moreover, this estimate neglects additional effects from concentration polarization and fouling. In practice, operating pressures in desalination plants are typically around 59 bar, corresponding to NaCl concentrations of about 70 g/L [77].

Concentration-gradient-driven processes such as forward osmosis (FO) can overcome this limitation by reversing the osmotic pressure gradient and thereby achieving much higher effective concentrations. Since FO depends on having a draw solution with higher osmotic pressure than the feed, it requires draw solutes that are more soluble than the salts in the feed to induce precipitation. This imposes constraints when treating feeds with highly soluble salts. Nevertheless, when using urea as the draw solute, FO has been demonstrated to achieve osmotic pressures up to 400 bar, exceeding the ~310 bar associated with saturated NaCl solutions and suggesting its potential viability for seawater ZLD [78].

Thermally driven membrane desalination processes, in contrast, can typically achieve higher concentrations than pressure-driven or concentration-gradient-driven methods and are not inherently limited by osmotic pressure. As observed with conventional thermal technologies, the driving force in thermal desalination is the vapor pressure gradient, which is primarily influenced by water activity rather than osmotic pressure. Since water activity decreases less steeply with solute concentration, membrane distillation (MD) can effectively concentrate brines to saturation and beyond. For example, MD has been shown to achieve precipitation of highly soluble salts such as NaCl (357 g/L) and $MgCl_2$ (560 g/L) under ambient conditions [76,79,80].

However, in DCMD configurations, some backflow of water can occur when feed concentrations sufficiently lower water activity to the point where the permeate side experiences a lower vapor pressure, reversing the flux. For instance, Quist-Jensen et al. [81] found that saturating LiCl solutions (solubility ~661 g/L) was nearly impossible with DCMD, whereas VMD could achieve crystallization.

Electrically driven membrane processes, such as electrodialysis (ED), also lack a theoretical upper concentration limit. In ED, ion removal is primarily determined by the applied current density. In principle, increasing current density or membrane area enables treatment of more concentrated streams. This has been demonstrated in practice, with feed concentrations up to 250 g/L processed successfully [82]. However, at high salinities, increasing current density alone eventually becomes ineffective due to limited ion transport at the probe. This threshold, known as the limiting current density, requires further increases in membrane area rather than current to achieve desalination of higher concentrations [83]. While this increases costs due to membrane requirements, it does not inherently limit the maximum treatable salinity. The driving force for the different membrane desalination methods dependent on the NaCl concentration is illustrated in (Figure 1-11).

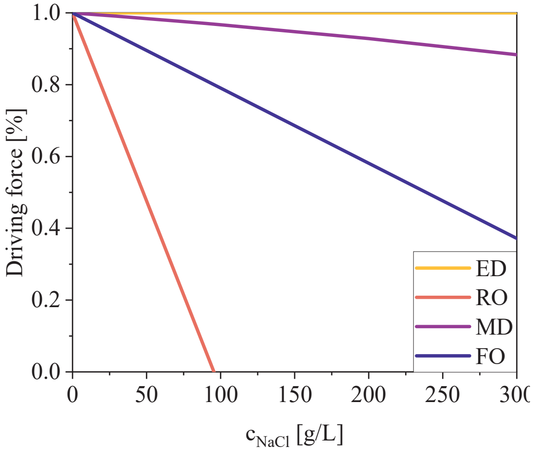

Figure 1-11, Illustrations of Theoretical driving force performance at optimum conditions of ED, RO (80bar), MD and FO (Urea draw solute) as a function of NaCl.

1.6.2 Energy consumption

Estimating the energy consumption of desalination systems in practice is complex, as many factors, including feed pretreatment, viscosity, and pump efficiency, significantly influence overall performance. However, it is possible to consider the specific energy consumption (SEC) of individual desalination methods under simplified single-pass configurations.

From a thermodynamic perspective, there is a theoretical minimum energy required to separate a saline solution into pure water and salt, which depends strongly on the salt concentration (Equation (1-5) and (1-6)). This value represents the absolute minimum energy necessary to de-mix a solution. For pressure-driven and electrically driven methods, a similar minimum energy threshold can also be established depending on the driving force, which will be close to the theoretical minimum. This will however lead to a slow process and a constant driving force is therefore added to the theoretical SEC of RO or ED (Equation (1-5) to (1-8)) as explained by Wang et al. [84,85].

$$SEC_{min} = vRT\left[\frac{c_f}{R_w}\ln\left(\frac{c_b}{c_f}\right) - c_p\ln\left(\frac{c_b}{c_p}\right)\right] \tag{1-5}$$

$$SEC_{min} = -\frac{-\pi_f}{R_w} * ln(1 - R_w) \tag{1-6}$$

$$SEC_{min}^{RO} = \frac{\pi_f}{1 - R_w} \tag{1-7}$$

$$SEC_{min}^{ED} = vRT\left(c_f - c_p\right)\ln\left(\frac{c_b}{c_f}\right) \tag{1-8}$$

Here *v, R, T, c,* R_w and π the cumulative valence of ions, ideal gas constant, temperature, solute concentration, water recovery factor and osmotic pressure respectively. Furthermore, the subscripts *RO, ED, min, f, b* and *p* are reverse osmosis, electrodialysis, minimum, feed, brine and permeate respectively. Thermal desalination processes such as MD, in contrast, are primarily governed by the latent heat of vaporization (ΔH_{lat}) as the theoretical limitation. The relationship between latent heat and salinity concentration is most accurately described empirically. Among available correlations, the formulation proposed by Valderrama et al. has demonstrated the best agreement with experimental data [86,87] (Equation(1-9))

(1-9)

$$\Delta H_{lat} = (a_1 + a_2(T - 273.15) + a_3(T - 373.15)^2 + a_4(T - 273.15)^3 + a_5(T - 273.15)^4)(1 - \frac{c_f}{1000})$$

When comparing the different driving forces, it becomes evident that the energy requirements of RO and ED are substantially lower, by roughly one to two orders of magnitude, than those of thermal processes such as MD, which rely on latent heat of vaporization (Figure 1-12(A)). This fundamental difference is the reason thermal desalination has historically been regarded as energy intensive. Generally, RO has a lower SEC than ED, particularly when treatment of high concentration solutes is required. This is because ED consumes energy proportional to the number of ions transported, whereas RO requires energy proportional to the applied hydraulic pressure and the losses associated with permeation. This distinction is reflected when considering the SEC as a function of water recovery (R_w) (Figure 1-12(B)). As RO systems must increase applied pressure proportionally to the final retentate concentration, ED only requires a modest increase in electrical input to prevent back-diffusion of ions into the permeate. This behaviour is further illustrated when plotting SEC as a function of the rejection coefficient(*R (1-10))*) (Figure 1-12(C)).

$$R = 1 - \frac{c_p}{c_f} \qquad (1\text{-}10)$$

Where c_p and c_f are the permeate and feed concentrations, respectively. In such comparisons, the SEC curves of RO and ED intersect at approximately $R \approx 73\%$ when desalinating 3.5g/L NaCl. Consequently, ED has a comparative advantage over RO in scenarios requiring high recovery factors, such as ZLD, or when treating streams with smaller concentration gradients, for example, converting brackish water to potable water. It is also notable that the SEC of RO and ED increases linearly with salinity, whereas the thermal energy demand generally decreases as concentration rises. This means that while electrical and pressure-driven processes become progressively less energy efficient with higher concentrations or recovery factors, thermal methods in these conditions tend to become relatively more favourable.

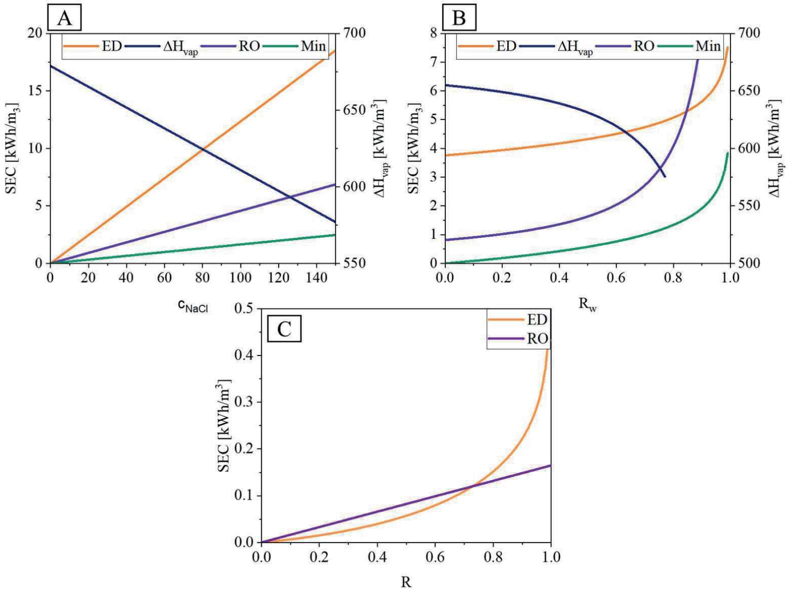

Figure 1-12, Illustrations of Theoretical specific energy consumption at optimum conditions of ED, RO and H_{vap} *(MD). A: SEC as a function of feed concentration (R=0.99,* R_w*=0.5). B: SEC as a function of water recovery factor (R=0.99,* C_{NaCl}*=35g/L). C: SEC as a function of solute rejection (*R_w*=0.5,* C_{NaCl}*=3.5g/L).*

These comparisons represent theoretical minimum energy requirements for the different desalination methods. In practical applications, system inefficiencies further increase actual energy consumption. For example, RO typically consumes approximately 4–6 kWh/m³, while ED requires around 2.7–8.0 kWh/m³, when desalinating seawater. It is generally accepted that ED is usually first more energy efficient than RO when the feed salinity is below approximately 5–10 g/L [88,89].

Thermally driven processes tend to exhibit even greater variability in energy consumption for desalinating seawater. For instance, MED and MSF typically consume between 14.45 and 27.25 kWh/m^3, whereas MD, which remains less commercially established, has reported energy consumption ranging from 1.6 up to 10,000 kWh/m^3, depending on system design and operating conditions [88,90].

A major factor contributing to these wide ranges is the potential for energy recovery. In thermal desalination, latent heat released during condensation can be recaptured to preheat the incoming feedwater. Additionally, supplying waste heat or utilizing environmental heat sources can further reduce the net energy demand. In some configurations, these approaches can effectively eliminate the need for dedicated heating energy, leaving only minimal electricity consumption for circulation pumps [91–93]. Accordingly, selecting an appropriate desalination method requires careful consideration of both the quantity and type of energy available. While RO and ED generally consume less energy for separation at low to moderate salinities, thermally driven processes can become more energy-efficient in applications involving high concentrations, high recovery factors, or access to low-cost or free heat sources.

1.6.3 (Ion)Selectivity

Selectivity refers to the ability of a membrane process to preferentially remove certain ions or solutes over others from the feed stream. This property is particularly important in valorizing the solid outputs of ZLD systems to enable brine mining applications.

Pressure-driven membranes have a long history of selectively separating valuable components. Dense membranes such as RO and NF can exhibit ion selectivity based on charge and ionic radius [94]. However, in practice, the selectivity of RO and NF is strongly influenced by feed concentration and composition, which can make achieving consistent performance challenging [95]. Despite this, RO and NF are often considered effective options for selective separations.

FO utilizes the same membrane materials as RO and NF and thus can also exhibit selectivity which is generally high [96]. Nevertheless, because FO requires a draw solution to generate osmotic driving force, the permeate contains both target solutes and draw solutes, necessitating additional downstream separation. This requirement makes FO less ideal for direct water or solute recovery [97].

ED offer inherently good selectivity, by inhibiting the transport of co-ions while promoting counter-ion migration [98]. Therefore, ED can separate cations and anions into distinct streams, and the use of monovalent/divalent selective membranes enables further refinement. This was demonstrated by Ying et al. [99]. Who demonstrated an ED process with a monovalent/divalent selective membrane which achieved a tenfold higher transport rate of Li^+ compared to Mg^{2+}.

Thermally driven membrane processes such as MD do not rely on membrane selectivity but rather on the relative volatility (high vapor pressure) of solutes and solvents. As a result, MD typically provides excellent rejection of non-volatile contaminants, including dissolved salts. Though non-volatile solutes are difficult to selectively separate, volatile solutes can be selectively transported which was demonstrated by Simoni et al. [100]. Although MD does not separate non-volatiles such as ions by charge or size, selective recovery can also be achieved via controlled precipitation, whereby differences in solubility cause one salt to crystallize preferentially over another [101,102]. Finally, it is important to note that membrane selectivity and permeate quality are often inversely related. For example, achieving 100% rejection of all solutes yields a pure permeate but no selectivity. Conversely, rejecting only specific solutes increase selectivity but reduces permeate purity. In contrast, selectivity achieved through precipitation does not involve this trade-off, allowing both high permeate purity and targeted recovery of specific salts.

1.6.4 Comparison

Based on the evaluation criteria discussed in the preceding sections, a qualitative assessment of the different desalination methods can be made. The results of this assessment are summarized in Table 1-1. Using the available information, the methods can be comparatively estimated in terms of their suitability for achieving ZLD, their potential for brine mining, and their capability to produce purified water.

Table 1-1: Qualitative estimation of RO, NF, FO, ED and MD for ZLD and brine mining. The (*) scoring system is; (*) not suitable, (**) Technically possible but with some challenges, (***) Suitable.

	RO	NF	FO	ED	MD
Driving force	Pressure	Pressure	Concentration	Electric potential	Vapor pressure
Energy type	Mechanical (Electric)	Mechanical (Electric)	Chemical	Electric	Thermal
SEC Energy consumption	Low (4-6 kWh/m^3) Limit 1.1 kWh/m^3	Low (4-6 kWh/m^3) Limit 1.1 kWh/m^3	1.1 kWh/m^3 no supplied energy needed. Much higher energy requirement if draw is treated	seawater 2.7-8.0 kWh/m^3 2500ppm or lower 0.7-2.5 kWh/m^3	Highest, min 640 kWh/m^3 approaching 0 kWh/m^3 if supplied by waste heat and heat recovery
Critical concentration	Limited by the membrane pressure limit and osmotic pressure to about ≈70000ppm	Limited by the same limiting forces as RO. ≈70000ppm	Limited by the draw solution osmotic pressure. (f.x urea=400bar)	Theoretically unlimited. However, due to heat loss from ion transport and current density limit treating brines above 10000ppm becomes expensive.	Until precipitation. DCMD is limited by water activity of permeate*

Selectivity	Low as rejection is high	Relatively high for monovalent and divalent ions	In the range of RO and NF. However, needs further processing to separate draw solute and permeate	High selectivity. Can separate both based on charge but also ion valence if modified.	High selectivity of volatiles. Selectivity of non-volatile ions possible through selective precipitation
Permeate quality	400ppm-500ppm SWRO	Depends on the membrane selectivity but will inevitably be higher than RO	Low grade. Draw needs to maintain a high TDS to keep driving force high.	Practically 150-500 ppm Can't separate larger non-charged molecules	Distilled water quality ≤10ppm
ZLD	*	*	**	**	***
Brine mining	*	***	**	***	** (***)
Water quality	***	**	*	**	***

From the qualitative evaluation of desalination methods, membrane distillation (MD) appears to be the most suitable technology for ZLD, as it is not inherently constrained by a maximum concentration limit and has been demonstrated capable of achieving crystallization. In addition to its ability to reach saturation, MD offers superior water purity, making it well-suited for both human consumption and industrial applications. The principal drawback of MD is its relatively high energy consumption, which is often the limiting factor for its widespread adoption in desalination. Nevertheless, given MD's unique capability to concentrate brines to the point of solidification, it is the only membrane-based technology among those evaluated that can achieve ZLD as a stand-alone process. Opportunities exist to reduce MD's energy demands through energy recovery strategies and the utilization of waste heat. Additionally, pre-concentrating the feed using other desalination technologies can significantly lower the overall energy requirement. While the selectivity of MD is less straightforward compared to processes such as NF or ED, and has not yet been fully characterized, improvements in the understanding and control of precipitation during crystallization could position MD as an effective single-step process for both brine valorisation and water recovery, potentially enabling ZLD in an economically viable manner.

Therefore, in this thesis there will be focus on the crystallization process while using thermally driven MD processes.

1.7. MCr

Although the term *membrane crystallization* (MCr) could, in principle, encompass any process that utilizes membranes to induce crystallization, it most commonly refers to crystallization driven by membrane distillation (MD). MCr (also referred to as MDCr or MDC) is, in its simplest form, a process in which selective mass transport of solvent occurs across a (often hydrophobic) membrane contactor in the form of vapor. This vapor removal concentrates solutes and cools the feed stream until supersaturation is reached, causing rapid crystallization of the target compounds [103]. MCr involves specific dynamic phenomena that additionally distinguish it from conventional evaporation–crystallization processes. Notably, concentration polarization and temperature polarization at the membrane–liquid interface strongly influences nucleation and crystal growth [104]. These effects lead to locally increased solute concentrations and decreased temperatures at the membrane surface relative to the bulk solution, both of which favor earlier onset of precipitation [105]. For this reason, it is not uncommon for crystallization to occur in MCr even when the bulk feed temperature remains elevated and solute concentrations are still below the nominal saturation point [105]. Overall, the advantages of MCr compared to simple crystallization arise from the combined effects of controlled mass and heat transfer dynamics inherent in the membrane process, as well as the specific interactions between the solute and the membrane surface.

1.7.1 Crystallization

To understand the advantages of MCr it is necessary to understand precipitation and nucleation theory. Precipitation occurs when saturation conditions are reached in a given solution, this occurs when thermodynamic conditions makes a two component system more favourable compared to a dissolved system [106] The common expression for solubility is the solubility product constant (K_{sp}), this expression is a constant for solubility of the solutes and is defined as a function of solute concentrations as seen in Equation (1-11), [107].

$$K_{sp} = [A]^x[B]^y \tag{1-11}$$

Here A, B, x and y is a hypothetical solute concentration of solute A and B, and their coefficients respectively. K_{sp} is linked with the Gibbs free energy of change (ΔG) which in turn is dependent on temperature, this expression can be formulated as in Equation (1-12), [107].

$$lnK_{sp} = -\frac{RT}{\Delta G} \tag{1-12}$$

Here R and T is the ideal gas constant and the temperature respectively. These relations illustrate the classical variables for precipitation, namely solute concentration and temperature. While K_{sp} represents a thermodynamic saturation point the solute conditions may in fact be different. A saturation index (SI) is therefore commonly used to illustrate favourable precipitation conditions (supersaturation) or unfavourable (undersaturation) this index is defined as in Equation (1-13), [108].

$$SI = \frac{IAP}{K_{sp}} \tag{1-13}$$

Here IAP is the ionic activity product (the actual product of solutes). Therefore, if $SI=1$ then the solution is at equilibrium (saturated), if $SI<1$ the solution is undersaturated and a stable solution is maintained and if $SI>1$ then supersaturation is reached, and spontaneous precipitation will occur [108]. Though $SI>1$ is reached this does not always cause immediate precipitation. This is due to the kinetics and critical energy barriers which inhibits immediate precipitation. However, over time precipitation will always occur at supersaturation an arbitrary zone where the crystal induction time is too high for pragmatic purposes [109]. This zone is called the metastable zone, and is simply defined by the induction time (t_i), which relies on the nucleation rate (R_n) which relationship can be seen in Equation (1-14) and (1-15) literature [110].

$$R_n = \rho Z j \left(- \frac{\Delta G_{crit}}{k * T} \right) \tag{1-14}$$

$$t_i \approx R_n^{-1} \tag{1-15}$$

Z, J, ρ and k is the Zeldovich factor, rate at which molecules attach to the nucleus, number of available nucleation sites per volume and Boltzmann constant respectively. A depiction of the different zones of a solution as well as the effects cooling and saturating can be seen in Figure 1-13. This approach results in high-purity solvent recovered on the permeate side and solid solute precipitated on the feed side, thereby simultaneously achieving ZLD and water recovery.

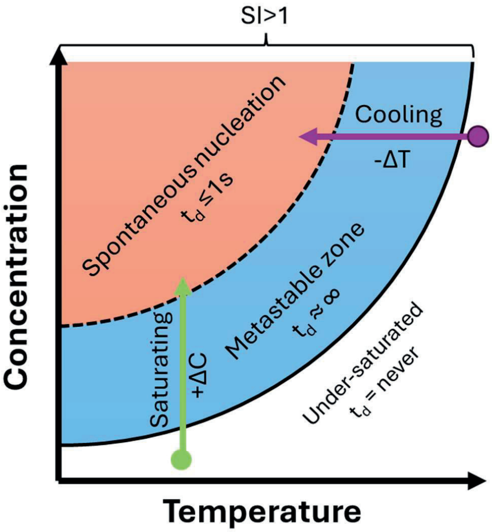

Figure 1-13, Depiction of spontaneous nucleation reached by either solution cooling or increasing concentration (saturating).

1.7.2 Temperature/concentration induced crystallization

Temperature and concentration are therefore traditionally the two primary parameters controlled in crystallization processes [111,112]. In cooling crystallization, temperature is decreased to induce supersaturation and nucleation. In contrast, evaporative crystallization achieves supersaturation by gradually increasing solute concentration through solvent removal. Both the concentration and temperature are parameters tunable in MCr. Directly, the temperature can be tuned by heating or cooling the feed and concentration will increase over time when solvent is being selectively transported from the feed to the permeate. However, as MCr is far from a homogeneous system, different conditions are found at different points of the system. For example, at the inlet of a MCr module the concentration and temperature may increase dynamically going towards the outlet of the membrane module. This happens since solvent is removed dynamically over the membrane which increases the concentration but also reduces the temperature due to evaporative cooling (and some conduction) along the membrane. This difference in concentration and temperature between inlet and outlet are commonly observed [113]. This leads to a difference in solubility from the inlet to the outlet which can be tuned for favorable conditions. This effect can however be mitigated by increasing feed flowrate, which will if increased sufficiently will lead to outlet conditions approaching inlet conditions [114]. Polarization of the temperature and concentration doesn't only happen along the membrane, but due to laminar layer conditions, solute and heat transport close to the membrane is governed by diffusion [115]. This is explained by Equation (1-16) and (1-17).

$$J_{solute} = A_s(C_{interphase} - C_{bulk}) \tag{1-16}$$

$$J_{temp} = B_t(T_{bulk} - T_{interphase}) \tag{1-17}$$

Here J_{solute} and J_{temp} are the fluxes of solutes and temperature from bulk towards the membranes. A_s and B_t are transfer coefficients for solutes and temperature respectively. subscripts interphase and bulk refer to at the membrane interphase and the bulk solution respectively. These phenomena are referred to as concentration polarization and temperature polarization, respectively [105,115]. As a result, the local conditions at the membrane interface can differ substantially from the apparent bulk concentration and temperature. Both temperature and concentration polarization is effected by the size and conditions of the laminar layer, this can be reduced by inducing turbulence in the bulk, via f.x turbulence promoters or feed flow [116]. A temperature and concentration profile in a MD system can be seen in Figure 1-14.

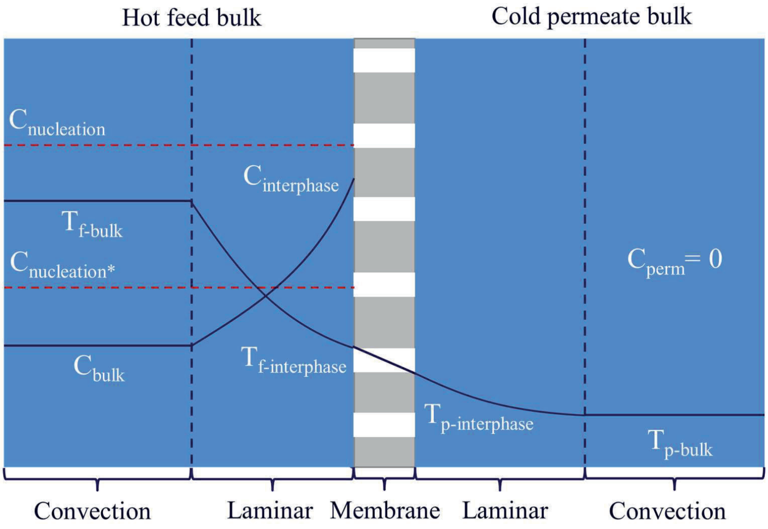

Figure 1-14, Depiction of a MCr-DCMD system where laminar layer and convective layers are depicted with a dotted line. Concentration polarization is depicted by a line which increases towards the membrane interphase (C_{bulk}-$C_{interphase}$). Temperature polarization is likewise depicted both on the feed side ($T_{f\text{-}bulk}$- $T_{f\text{-}interphase}$) to the permeate side ($T_{p\text{-}interphase}$- $T_{p\text{-}bulk}$). Furthermore, a saturation concentration ($C_{nucleation}$) and a saturation concentration at the interphase conditions ($C_{nucleation*}$) are depicted with red lines.

Therefore in MCr by controlling temperature and concentration conditions in the bulk and interphase, it is possible to influence crystallization behavior. For example, Zhang et al. [117] demonstrated that increasing the feed temperature decreased the average size of NaCl crystals. Both nucleation and crystal growth rates have been shown to depend on temperature, although the direction of these effects is often highly case-specific [118–120]. Induction time, defined as the time interval between achieving supersaturation and the appearance of the first nuclei, generally decreases with increasing temperature due to enhanced solvent evaporation rates [121]. Moreover, precise temperature control in membrane crystallization (MCr) can yield selectivity in the polymorph and composition of the precipitated solids. Different crystal polymorphs have been obtained by adjusting supersaturation conditions through parameters such as temperature and feed velocity [121]. For example, Di Profio et al. [122] showed that varying the vapor flux could induce different polymorphs of glycine. Quist-Jensen et al. [123] demonstrated that LiCl precipitates transitioned between needle-like and cubic morphologies depending on feed temperature and flow rate, with needle-like crystals favored at elevated temperatures. It has also been proposed that MCr could be applied to selectively precipitate target compounds based on their differing solubilities as functions of temperature and concentration. Shirazi et al. [114], for example, successfully precipitated Li_2CO_3 selectively from a synthetic solution containing NaCl and KCl. However, achieving such selective precipitation in real brines remains challenging due to co-precipitation phenomena [124].

1.7.3 Solute-membrane interaction

Temperature and concentration primarily influence crystallization. Additionally, the membrane itself provides a surface that can act as a preferential site for nucleation, governed by physicochemical and morphological factors. These phenomena are described by classical nucleation theory (CNT) [125,126]. According to CNT, nucleation occurs when there is a thermodynamic driving force favoring the formation of a new phase from the dissolved state. This is expressed as a net negative free energy change associated with the volume occupied by the emerging phase (ΔG_{volume}). However, the creation of an interface between the newly formed phase and the surrounding solution also introduces interfacial tension, which contributes a net positive free energy change ($\Delta G_{surface}$). The interplay between these two opposing contributions results in an overall Gibbs free energy change that determines the likelihood of nucleation. This balance can be expressed by the equation (1-18):

$$\Delta G_{hom} = \Delta G_{volume} + \Delta G_{surface} = V * \Delta G_{nucleation} + A_{\alpha\beta} * \gamma_{\alpha\beta} \tag{1-18}$$

Here ΔG_{hom}, V, $\Delta G_{nucleation}$, $A_{\alpha\beta}$ and $\gamma_{\alpha\beta}$ is the Gibbs free energy of homogeneus nucleation, molar volume, volumetric free energy of a crystal, interfacial area of nucleate and continuous phase and interfacial tension respectively. Since the free energy is dependent on the shape of the nucleate is important to consider the actual shape of the nucleate as well as the interphase energy.

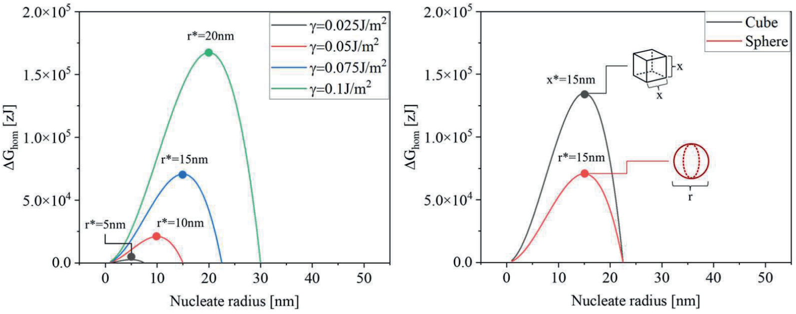

Figure 1-15, Left: Plot of free energy as a function of nucleus radius. Right: different shapes of nucleate crystals Here r and x refers to the radius and length/with of a spherical and a cubic nucleate respectively.

Most crystallization, happens as heterogeneous nucleation this is when another phase is included, often referred to as a "wall"[125]. This wall phase could for example be a membrane piece. The membrane "wall" has a large effect on the likelihood of nucleation, by removing some of the surface tension from a nucleate. Here especially the contact angle (θ) has a correlation between heterogenous and homogeneous as can be seen in Equation (1-19).

$$\Delta G_{het\_sphe} = \Delta G_{\hom\_sphere} * \left(\frac{2 - 3cos\theta + \cos^3\theta}{4}\right) \tag{1-19}$$

In Figure 1-16, a correlation between nucleate contact angle and *ΔG* can be seen. It can be seen that the necessary energy for critical nucleation size increases with the increasing contact angle. This is due to at 180° there is no contact between the wall/membrane and the crystal formation and the wall/membrane will therefore not have any effect on the nucleate formation. Through the CNT theory it could be tempting to believe that the crystal size does not change with changing contact angle. However, though the apparent critical radius doesn't change the critical nucleate volume lowers with decreasing contact angle. Therefore, the critical size of the nucleates will lower with lower contact angles.

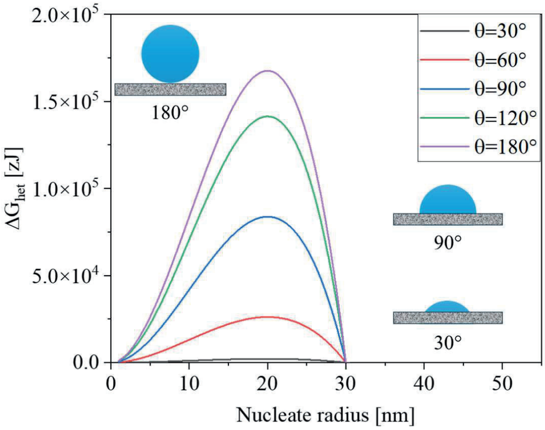

Figure 1-16, Plot of free energy of heterogeneous nucleation at different contact angles.

Membrane surfaces are usually not smooth homogeneous films as illustration Figure 1-16 would suggest, they are usually porous with somewhat rough surfaces. Both porosity and Wenzel surface roughness will according to CNT change the nucleation formation. This should be apparent from (1-20 and (1-21 however to further demonstrate Drioli et Al. [127] Simplified the relationship between $\frac{\Delta G_{hom}}{\Delta G_{het}}$ and membrane porosity (ε) and also membrane Wenzel roughness (r_w) when considering prismatic roughness in the following relationships (Equation (1-20) and (1-21)):

$$\frac{\Delta G_{hom}}{\Delta G_{het}} = \frac{1}{4}(2+cos\theta)(1-cos\theta)^2\left(1-\frac{\varepsilon(1+\cos\theta)^2}{(1-cos\theta)^2}\right)^3 \tag{1-20}$$

$$\frac{\Delta G_{hom}}{\Delta G_{het}} = \frac{1}{4}\left(\frac{r_w cos\theta(1+cos\theta)-2}{cos\theta(1+cos\theta)-2}\right)^3 * (\cos^3\theta - 3cos\theta + 2) \tag{1-21}$$

From this some $\frac{\Delta G_{ho}}{\Delta G_{het}}$ relations as function of ε and r_w can be seen in Figure 1-17. It can be seen that increasing the membrane ε will favour nucleation. Likewise the surface roughness r_w also favours nucleation formation.

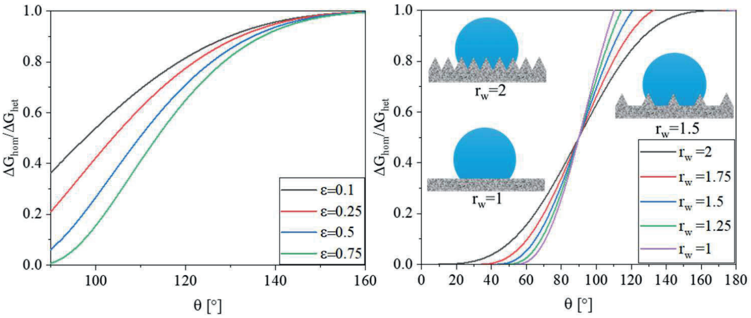

Figure 1-17, homogeneous to heterogenous free energy plots as a function of contact angle. With different membrane porosities on the left and different Wenzel roughness on the right. (based on Drioli et Al. [127])

Although the preceding discussion is based on theoretical considerations of CNT, experimental studies have confirmed that crystallization can indeed be enhanced by modifying substrate properties such as porosity [128] and surface roughness [129]. Furthermore, a concept called Ostwald's rule of stages, a widely accepted concept in crystallization science, states that when multiple polymorphs of a compound exist, the polymorph with the higher Gibbs free energy (i.e., the more soluble and less stable form) tends to form first, eventually transforming into the thermodynamically more stable (less soluble) polymorph [130]. This principle implies that controlling the free energy of formation ΔG provides a means to influence polymorph selection. Accordingly, polymorph formation is closely linked to heterogeneous nucleation processes and is affected by membrane porosity, surface roughness, and interfacial interactions. This dependence of polymorph stability on surface structure has been experimentally validated. For example, Yang et al. [131]. demonstrated that modifying the structure and material of the crystallizer surface significantly increased the likelihood of precipitating an otherwise unstable polymorph of carbamazepine. Therefore, not only is it possible to tune nucleation formation favourability via the membrane structure and surface tension but also selectively nucleate polymorphs.

1.7.4 Directions of MCr

Therefore, compared to conventional crystallization, membrane crystallization (MCr) offers enhanced control over crystallization due to enhanced concentration and temperature control and the physicochemical interactions between the nucleating solute and the membrane surface. In theory, MCr provides significant advantages, including controlled nucleation, tunable induction time, adjustable crystal growth, and polymorph selectivity. Combined with its integrated desalination capability, MCr is highly promising for achieving ZLD and brine mining in a single process. However, because MCr is a relatively new field (≈30 years), several obstacles must be overcome before it becomes a viable industrial technology. As highlighted in numerous reviews [121,132,133], the main challenges include:

- Scaling and fouling mitigation

- Selectivity in multi-solute systems

- Recoverability of precipitated crystals

Scaling and fouling are among the most limiting factors. Surfactants and oily deposits can irreversibly damage membranes, while mineral scaling may render membranes hydrophilic, causing liquid breakthrough [134]. Selectivity remains difficult to control, as co-precipitation frequently occurs in real brines despite some demonstrations of targeted crystallization. Crystal recovery is also challenging, since crystals tend to accumulate near the membrane interface or in the brine slurry. Recovery often requires interrupting operation, which is undesirable because prolonged immersion promotes uncontrolled crystal growth. While batch processing is commonly used in industrial crystallization [135,136], it is not ideal for continuous MCr applications. To address these challenges, several solutions have been proposed, though many still require technological maturity. Consensus exists that further understanding of crystallization dynamics, development of new materials and membranes, and improved process designs are all essential.

Elucidation of MCr Crystallization: A better understanding of nucleation and growth near the membrane is key to overcoming scaling, wetting, and limited selectivity. Research priorities include wetting/scaling control, co-precipitation behaviour, and computational modelling. Wetting and scaling are tightly linked and often resist mitigation strategies like intermittent operation or hydrophobic membranes, particularly in solar-driven systems. Membrane properties (e.g., pore size, roughness) and localized temperature gradients strongly influence these phenomena. Selectivity is further complicated by overlapping solubilities and similar nucleation kinetics. Mechanistic and thermodynamic models are needed to enable targeted recovery. Molecular dynamics simulations have provided insights into nucleation mechanisms but lack spatial resolution; coupling MD with computational fluid dynamics (CFD) could better capture local gradients. Integration of tools like PHREEQC with kinetic data can further guide design and predict scaling risks.

Membrane and membrane materials: Current membranes are typically designed for pressure-driven separations rather than MD or MCr. MCr membranes require a pore size of >0.1 μm, hydrophobicity, and robust thermal and chemical stability. As a result, PP, PVDF, and PTFE remain the main materials [137,138]. Fluoropolymers are preferred for their durability but have come under scrutiny due to PFAS-related health and environmental concerns, prompting regulatory restrictions [139]. Consequently, new materials specifically designed for MCr are needed. Some efforts have focused on doping membranes with hydrophobic nanoparticles or surface functionalization [140,141], but these approaches complicate fabrication and remain costly without resolving the limitations of the bulk materials. Membrane geometry also plays an important role in hydrodynamics and nucleation as explained in section 1.7.3. Techniques such as additive manufacturing (AM) have been investigated to produce micropatterned membranes with anti-wetting properties for non-membrane related objects [142]. AM offers exceptional geometric control down to sub-micron scales [143], expanding the range of usable materials and enabling innovative designs. However, despite significant interest, no scalable and reliable AM methods for producing functional membranes have yet been established [144–146]. Advancing AM and materials research could unlock new possibilities for MCr membranes and address many of the existing barriers.

Process Design: Process design of MCr systems can be further optimized. Most MD configurations were not developed for crystallization, and retrofitting them introduces limitations. Three main design aspects are relevant:

1. Module design
2. Membrane utilization
3. Process integration

Conventional MD modules are designed to maintain uniform temperature profiles to maximize water flux [113]. For MCr, however, designs that mitigate fouling and scaling may be preferable. For instance, high shear conditions at the membrane surface could be induced using 3D-printed shear promoters [147,148]. Membrane utilization modes (DCMD, AGMD, SGMD, VMD) offer flexibility in heat recovery and flux control but do not fully address scaling or crystal recovery challenges. Alternative approaches have been proposed. Immersed MCr systems, where membranes are submerged in the feed tank, allow crystals to precipitate in the bulk and settle, simplifying recovery [149]. Other configurations pass gas through immersed membranes, simultaneously aiding vapor transport and reducing fouling [150]. MCr could be integrated with RO or NF to pre-concentrate brines. This hybrid approach is the most frequently proposed solution, as it can enhance selectivity and reduce energy consumption. For example, MD can concentrate RO retentate close to saturation before final crystallization in a separate unit. However, combining technologies may reduce process simplicity and potentially diminish the nucleation control benefits offered by heterogeneous crystallization directly on the membrane surface. One way to hybridize RO/NF and MCR is by what is called Percrystallization. Percrystallization, was first described by Kober in 1917 [151] and differs fundamentally by allowing the feed to permeate and form a film on the membrane's opposite surface. Thereby needing liquid permeation through the membrane as in RO/NF. The film is then evaporated by gas or vacuum, as in MD/MCr, producing dry easily recoverable crystals and potentially improving selectivity by combining size exclusion and vapor transport.

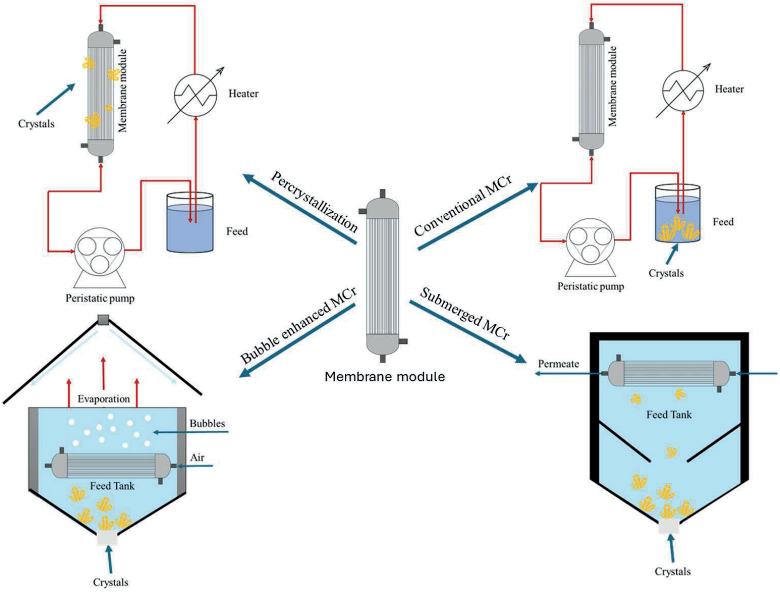

Figure 1- 18, different modes of MCr (illustration based on Aamer et al. [132]).

Therefore, through this thesis the aim is to advance the MCr process by finding new methods for making novel membranes via additive manufacturing and investigate new methods such as percrystallization for a more robust and selective one step MD and MCr method. Finding a way to use both additive manufacturing for new membranes and elucidate percrystallization, is believed to take us a step further towards mitigating the problems facing current MCr, leading to industrial applicability for ZLD and brine mining.

1.8. Scope summary and objectives

Having control over mineral crystallization is crucial for future sustainable resource recovery like ZLD and brine mining. MCr is seen here to be a promising method as a future crystallizer and water desalination method. However, MCr is a relatively new and rarely utilized method and is therefore also in its early infancy of development. Current available membranes and methods do not possess the tunability of geometry, physicochemistry and process parameters which is known to have a great impact on mineral crystallization. We believe that with the utilization of AM, which has an unprecedented control of processing geometry might uncover new shapes and materials which could improve crystallization. Therefore, through this project in collaboration with DTU department of Civil and Mechanical Engineering, we will utilize conventional and unconventional 3D printing methods to make novel membrane or membrane related items. We further believe that a since MCr is relatively early stage, it could be improved by utilising new methods such as the percrystallization concept which though an old technology hasn't gained much attention in the membrane field but due to the increased focus on crystallizers and its selectivity would fit the concept of the futures crystallizers. The scope of this work is therefore to use both AM and percrystallization and the combination thereof for MCr and thereby to uncover new improved ways of mineral recovery and water treatment. This will be done by the following objectives:

1. Develop/source an additive manufacturing method suitable for membrane production.
2. Develop a material suitable for membrane distillation.
3. Produce a membrane via additive manufacturing capable of MD and MCr and test it in an appropriate setting
4. Make a MCr system capable of selective crystallization via percrystallization.
5. Showcase percrystallization utilization for real world solutions

1.9. Thesis content

This thesis is written as a combined collection of works/papers made during this thesis. A summary of included works can be found in section 1.9.1. Other data is supplied as supplementary information found in section 1.9.2. Furthermore, my master thesis will be included as an introduction and will be put in appendix one and referred to as [A1].

The experiments in this thesis were mostly done at Aalborg University. Minor experiments were done at Danish Technological institute and Lund university.

1.9.1 Included works

The papers are listed below and will be cited by their roman numerals in the following thesis:

I. **Bastian S. Kirkebæk,** M. Artemeva, J.L. Navas, A.H. Danielak, D.B. Pedersen, A. Ali, C.A. Quist-Jensen, Tunable physicochemical properties of 3D printed membranes via copolymerization and micropatterning, J Memb Sci (2025) 124483. https://doi.org/10.1016/J.MEMSCI.2025.124483.

II. **Bastian S. Kirkebæk**, Aamer Ali, Cejna A. Quist-Jensen, fully 3D printed membrane for water desalination (to be submitted)

III. **Bastian S. Kirkebæk**, Aamer Ali, Cejna A. Quist-Jensen, 3D printing of inherently porous membrane spacers for improved performance (to be sumitted)

IV. **Bastian S. Kirkebæk**, Anders Emuel Olsen, Alexander V. Grønne, Aamer Ali, Cejna A. Quist-Jensen Membrane crystallization of seawater for CO_2 storage (to be submitted)

V. **Bastian S. Kirkebæk**, Anders Emuel Olsen, Aamer Ali, Cejna A. Quist-Jensen, Recrystallisation for zero liquid discharge of industrial wastewater, (to be submitted)

1.9.2 Other included works

Elements of my master thesis “Additive manufacturing of membranes with controlled inherent porosity using SLA printing technology” will be included only as introduction and will be referred to as [A1]. The total master thesis can be seen in Appendix 1.

[A1] **Bastian Kirkebæk**, Additive manufacturing of membranes with controlled inherent porosity using SLA printing technology (Masters thesis, 2023), Proceedings have been published in peer reviewed journal: **Kirkebæk, B.S.**, Ali, A. & Quist-Jensen, C.A. Masked stereolithography and polymerization induced phase separation for 3D printing of membranes. *Sci Rep* **15**, 18776 (2025).

[A2] Initial results for VPP-PIPS printed hydrophobic topography for membrane distillation.

[A3] Initial results from percrystallization of sugar-beet wash water from Nordzucker, Nakskov, Denmark.

Chapter 2. Additive manufacturing

2.1. AM Principle

The development of membranes with complex geometries has been shown to significantly improve performance by enhancing mass and heat transfer [152,153], reducing fouling tendencies [154–156], promoting better cell adhesion [157–159], and modifying surface wettability [160,161]. As discussed previously, such features also offer benefits for MCr. Despite these advantages, conventional membrane fabrication methods are largely restricted to producing simple flat-sheet or hollow fiber configurations [162,163]. Additive manufacturing (AM), commonly referred to as 3D printing, provides precise control over object geometry in all spatial dimensions. According to ISO/ASTM 52900, AM is defined as “a process of joining materials to make objects from three-dimensional model data, usually layer upon layer.” In practice, a computer-aided design (CAD) file is digitally sliced into instructions, often G-code, that direct the printer to build the object layer by layer. Depending on the AM process, additional post-processing steps such as post process curing or cooling may be required [164,165].

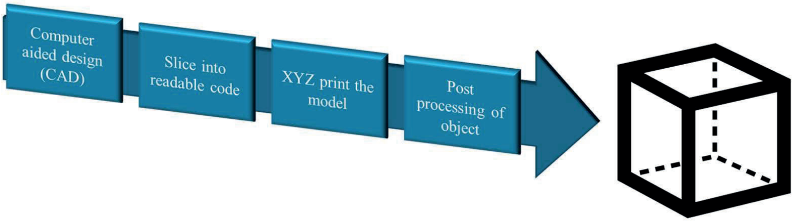

Figure 2-1, Generalized definition of additive manufacturing as a flowchart.

This broad definition makes additive manufacturing (AM) encompass a wide range of processes, leading to the development of many subcategories. Traditionally, the three most common AM methods have been stereolithography (SLA), fused deposition modelling (FDM), and selective laser sintering (SLS) [166]. However, this classification is now somewhat outdated, as numerous new AM techniques have emerged. The field also lacks consistent terminology, with multiple names often used for the same process. For example, stereolithography may be referred to as SLA, SL, or vat photopolymerization (VPP). To address this inconsistency, the ISO/ASTM 52900 standard was established to harmonize definitions and nomenclature (see Figure 2-3) [165].

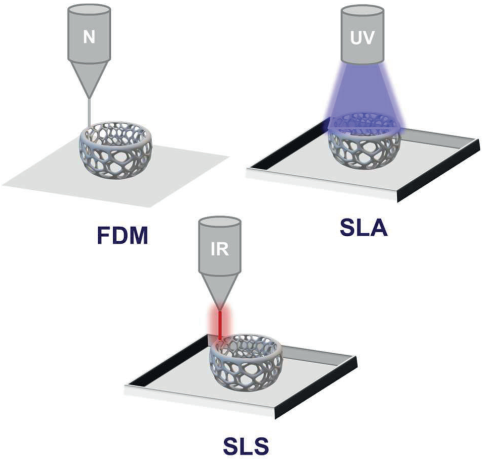

Figure 2-2, Illustrations of the 3 most common 3D printing methods and their collegial abbreviations.

Based on the physical state of the processed material, solid, liquid, or powder, additive manufacturing (AM) methods can be grouped into three main categories, which further expand into seven widely used techniques [162]:

1. **Material Extrusion (MEX):** A thermoplastic filament is fed through a heated nozzle and deposited layer by layer to build the object. The most common MEX process is fused filament fabrication (FFF), also known as fused deposition modeling (FDM).

2. **Material Jetting (MJT):** Liquid droplets of material are selectively deposited onto a build platform, solidifying either through cooling or UV curing.

3. **Sheet Lamination (LOM):** Sheets of material are cut to shape, typically using a laser or blade, and bonded together layer by layer to form the part.

4. **Powder Bed Fusion (PBF):** A laser or electron beam selectively fuses regions of a powder bed. This category includes selective laser sintering (SLS), widely used for manufacturing metal and ceramic components.

5. **Direct Energy Deposition (DED):** Material is simultaneously melted and deposited by a focused energy source, similar to advanced welding processes.

6. **Binder Jetting (BJT):** A liquid binding agent is deposited onto a powder bed to create a “green body” which is then post-processed to consolidate the material.

7. **Vat Photopolymerization (VPP):** A liquid photopolymer resin is selectively cured by a light source within a vat. This process, also referred to as stereolithography (SLA) or SL, is one of the most prevalent AM methods alongside MEX.

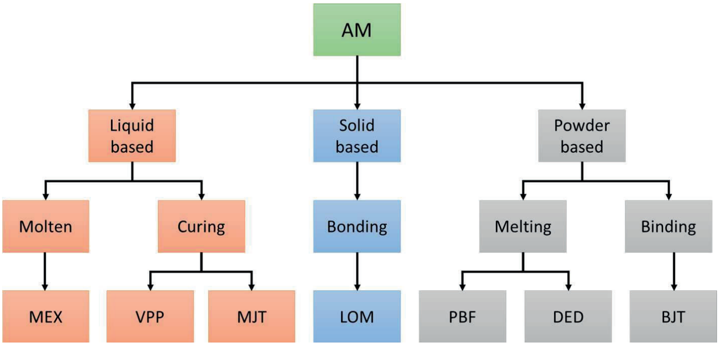

Figure 2-3, Flowchart of different categories of AM methods based on ISO/ASTM 52900 [162]

Given the diversity of additive manufacturing (AM) methods, the technology is highly versatile. For membranes, this design freedom is particularly advantageous, as membrane performance is strongly influenced by geometry and morphology [167,168]. Another benefit of AM is the wide range of materials that can be processed, which is also critical for membrane fabrication. However, achieving functional membranes directly via AM requires high resolution. For example, producing microfiltration (MF) membranes, which have the largest pore sizes among pressure-driven membranes, demands a resolution of ≤1 μm. Different AM techniques offer varying resolutions, with vat photopolymerization (VPP) providing the highest. In particular, two-photon polymerization (TPP), an advanced VPP method, has demonstrated feature sizes down to 9 nm, sufficient for fabricating both microfiltration and ultrafiltration structures [169–171]. Nevertheless, a general trade-off exists in AM between resolution, maximum build size, and print speed. As a rule, higher resolution results in smaller printable areas and slower fabrication. Ge et al. [172], mapped the relationship between build area and resolution, as illustrated in Figure 2-4.

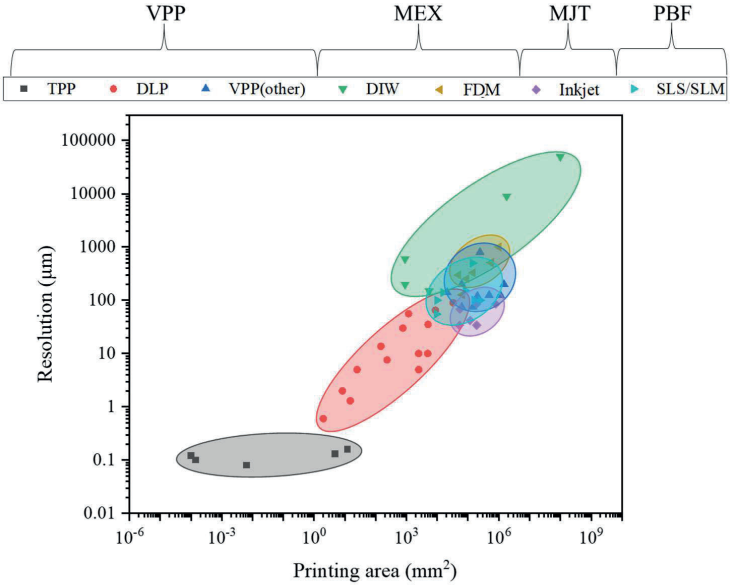

Figure 2-4, Relationship between resolution and maximum printing area size of different types of 3D printing methods (data from Ge et al. [172]), Note: other VPP(other) is other types of VPP printing methods, such as direct laser and LCD masked VPP.

This trade-off implies that producing membranes with pore sizes ≤1 μm restricts fabrication to areas of approximately 1 cm² or smaller, even before considering additional challenges such as overexposure during curing and difficulties detaching membranes from the build platform. Furthermore, most AM systems capable of such resolutions are laboratory-scale setups and are not commercially available [173–175]. As a result, directly printing membranes via AM remains challenging due to the limitations imposed by available technologies and the inherent correlation between resolution and build size. This constraint is reflected in the fact that most directly 3D-printed membranes have only been suitable for lab scale applications like oil–water separation, where pore sizes exceeding 150 μm are acceptable [166]. To overcome these limitations, less direct strategies have been proposed. One approach involves 3D-printing membrane supports, which are subsequently coated or modified using conventional fabrication techniques such as phase inversion or electrospinning. This enables the production of membranes with tailored surface topographies, for example, wavy structures that improve antifouling performance. However, this two-step process reduces design freedom and reintroduces many of the constraints associated with conventional manufacturing methods like injection moulding [176,177]. Another strategy is porous printing, as exemplified by selective laser sintering (SLS), where the inherent porosity of sintered particles creates a permeable structure. While this allows for the fabrication of large-area porous components, the resulting pore sizes typically range from 10–800 µm, making them unsuitable for most membrane separation processes [178–180]. An innovative solution combining additive manufacturing and phase inversion was demonstrated by Dong et al. [181], who used polymerization-induced phase separation (PIPS) instead of conventional techniques such as NIPS or TIPS. This approach enabled the creation of nanoporous structures with pore sizes below 1 µm while maintaining the resolution and build size capabilities of larger VPP systems. Subsequently, Kirkebæk et al. [182] applied this method to produce ultrafiltration/microfiltration-range membranes with areas up to 103 cm² within minutes, with the promise of easy scalability to beyond this area. The process preserved the geometric freedom of VPP, achieving macrostructures with 50 µm resolution. Given these advantages, VPP combined with PIPS appears to be one of the most promising methods for membrane fabrication and is therefore the primary focus of this thesis.

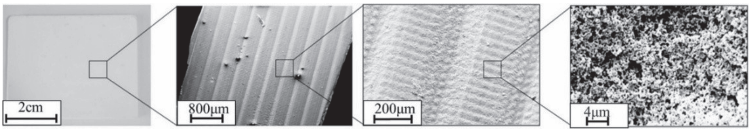

Figure 2-5, of porous 3D printed membrane via VPP-PIPS with special triangular prism topography (Kirkebæk et al. [182])

2.2. VPP-PIPS

VPP-PIPS (or SLA-PIPS, depending on terminology) combines vat photopolymerization (VPP) with polymerization-induced phase separation (PIPS). Understanding both mechanisms is essential to appreciating the process advantages for membrane fabrication and how micro- and macrostructures are formed.

2.2.1 Vat Photopolymerization (VPP)

As described earlier, VPP operates through the photohardening of a reactive polymer precursor, which can be a monomer, dimer, trimer, or oligomer that undergoes photopolymerization to generate polymer chains [183]. In most applications, a mixture of monomers or oligomers, crosslinkers, and photoinitiators, collectively referred to as “ink” is used [183,184]. This formulation is typically UV-reactive within the 365–405 nm wavelength range. Upon UV exposure, polymerization initiates, most often via a radical polymerization mechanism. This process is conventionally divided into three steps [185]:

1. **Initiation (Equation (2-1) and (2-2)):** The photoinitiator (I) absorbs UV energy and decomposes into an active radical species (R), which activates the monomer (M).

2. **Propagation (Equation (2-3)):** Activated monomers sequentially react to form growing polymer chains.

3. **Termination (Equation (2-4) and (2-5)):** Polymer chains are terminated by reaction with another radical, either from another propagating chain or an additional photoinitiator fragment.

Initiation: $$\mathrm{I} \overset{hv}{\rightarrow} 2R\cdot \tag{2-1}$$

$$R\cdot + M \rightarrow RM\cdot \tag{2-2}$$

Propagation:

$$\mathrm{RM}\cdot + \mathrm{nM} \rightarrow R[M]_n M\,\cdot \qquad (2\text{-}3)$$

Termination:

$$\mathrm{RM}\cdot + \mathrm{RM}\cdot \rightarrow \mathrm{R}_2 M_n \qquad (2\text{-}4)$$

$$\mathrm{RM}\cdot + \mathrm{R}\cdot \rightarrow \mathrm{R}_2 M_n \qquad (2\text{-}5)$$

Here I, hv, R and M, photoinitiator, photons, photoinitiator product and monomer respectively.

2.2.2 VPP methods

Multiple irradiation techniques are employed in vat photopolymerization (VPP). The simplest configuration uses a controlled laser beam to selectively cure the resin point by point. While this method achieves high precision, it is relatively slow because it solidifies only one spot at a time [186]. Masked VPP addresses this limitation by projecting UV light through a screen, commonly an LCD, that selectively blocks or transmits light to form an entire layer simultaneously [187,188]. This approach enables much faster printing and is the most prevalent VPP technique in commercial systems. However, its resolution is limited by the pixel size of the LCD, typically between 32–50 μm. Another common method is digital light processing (DLP), which employs an array of micromirrors to project UV patterns onto the resin surface [189]. Like masked VPP, DLP cures full layers at once but offers higher resolution because the projected image can be optically focused [187,188]. However, increasing resolution by focusing the lens also reduces the effective curing area.

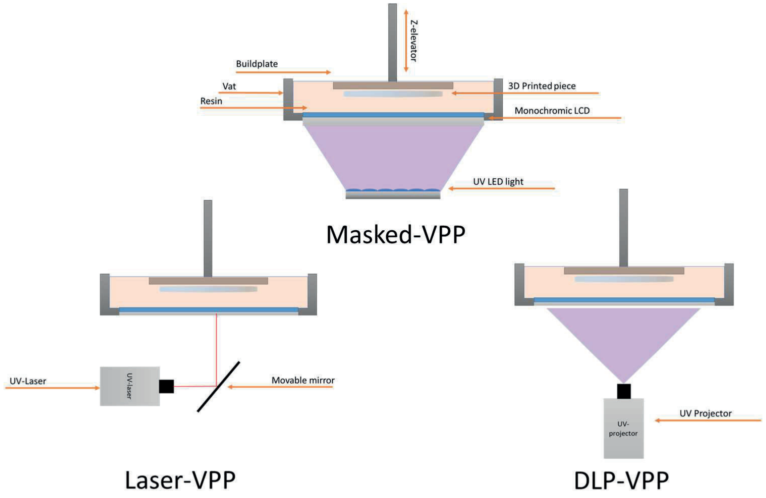

Figure 2-6. 3 most common VPP methods, laser-VPP(Laser-SLA), masked-VPP(MSLA) and DLP-VPP(DLP-SLA).

The resolution of the VPP process depends primarily on the spot size but also the activation energy delivered by the UV source. Excessive UV exposure results in overcuring and reduced resolution, while insufficient exposure prevents complete polymerization, producing a weak, gel-like structure [173,190,191]. In addition, the focal point and intensity distribution of the UV irradiation are critical for achieving high resolution. Because the beam intensity follows a Gaussian profile, only the beam center reaches sufficient energy to initiate polymerization reliably as depicted on Figure 2-7 [192]. This intensity gradient underlies VPP's exceptional resolution, allowing feature sizes down to the nanometer scale despite the diffraction limit [192]. Furthermore, by increasing the concentrations of photons with a high intensity (often pulsed) laser, can lead to two photo absorption or two photo polymerization (TPP or 2PP). This is done with photons with down to half the bandgap of the necessary photon. This allows for even better control of the polymerization which is why TPP is used in most sub 1µm printing[193,194].

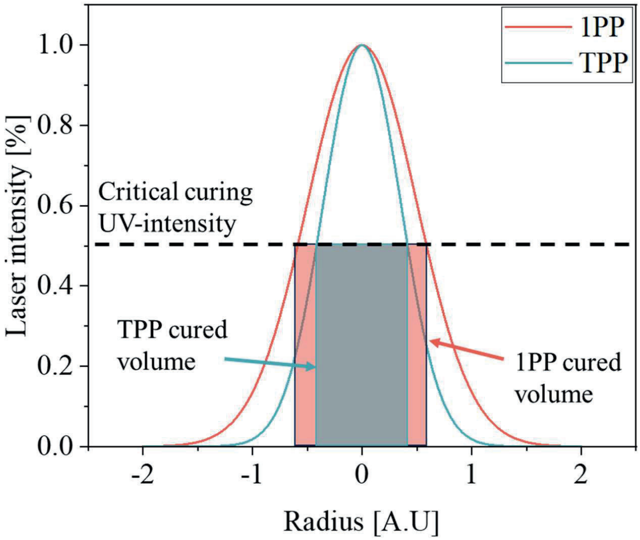

Figure 2-7, Laser intensity distribution in laser focus "one photon polymerization" and TPP (figure based on Zhou et al [192]).

2.2.3 VPP materials

The polymers used in VPP are predominantly thermosets formed via radical polymerization, with acrylate-based functional groups being the most common [183,195]. From these base acrylates, a vast array of new materials can be developed through co-polymerization, enabling an almost unlimited range of achievable polymer compositions. The final VPP-produced objects are thermoset plastics, which are generally stronger, more brittle, non-dissolvable, and more heat-resistant than thermoplastics. Furthermore, the co-polymerization capability of VPP allows tuning of key physicochemical properties, including hydrophilicity, flexibility, and mechanical strength [196,197]. These attributes, tailorable surface chemistry, high mechanical strength, and insolubility, contrast with conventional polymeric membrane manufacturing, which relies almost exclusively on thermoplastics and thus lacks similar performance characteristics [198,199]. The combination of high resolution and access to advanced materials offered by VPP could be highly advantageous for membrane fabrication, particularly for MD and MCr applications where thermally stable, chemically robust, hydrophobic membranes are essential.

2.2.4 Polymerization induced phase separation (PIPS)

PIPS is a phase inversion method similar to TIPS, NIPS and VIPS, where the solubility of the polymer is rapidly decreased to induce phase separation [200]. The phase separation process leads to polymer rich and polymer poor zones, the polymer rich zones end up being the membrane walls and the polymer poor zones the voids. This leads to a porous membrane network, the overall phase inversion process can be explained by the Gibbs free energy of mixing (ΔG_{mix}) in the Flory Huggins relation:

$$\Delta G_{mix} = \mathrm{RT}[n_1 \ln{(1 - \vartheta)} + n_2 \ln{(\vartheta)} + n_1 \vartheta \chi_{12}] \qquad (2\text{-}6)$$

Here n_1 and n_2 are the mole amount of porogen and polymer respectively, χ_{12} is the solvent polymer interaction parameter and ϑ is the molar volume of polymer. In PIPS the solubility is rapidly decreased by polymerization, this is done by lowering the mole amount of the monomer/polymer. As can be seen in Equation (2-6), this leads higher ΔG_{mix} and thereby leads to lower solubility and phase inversion. Since the PIPS technique relies on monomers and oligomers rather than polymers used in conventional phase inversion methods, the solubility of the base components is higher which can be dissolved in solvents such as water [201,202]. This opens for new porogens which previously couldn’t be used. Since PIPS utilize polymerization it can be utilized in the VPP process during the UV-curing step and thereby result in porous membrane networks in the bulk printed material. The of PIPS follows the same trend as other phase inversion schemes, however Flory Huggins relation only explains the solubility, Cahn Hilliard is used as the kinetic decomposition term, the expression can be seen at Equation(2-7) [203,204].

$$\frac{\delta c}{\delta t} = M_{CH}\nabla^2\left(\frac{\delta F(c)}{\delta c}\right) = M_{CH}[-\kappa\nabla^4 c + \nabla^2\frac{\delta\Delta G_{mix}(c)}{\delta c}] \quad (2\text{-}7)$$

Here M_{CH}, $F(c)$ and κ are the molecular mobility, total free energy of the system and interfacial constant respectively. This leads to some predictability of porous structure in phase inversion systems as shown in the simulation based on Soares et al in Figure 2-8 [182,205].

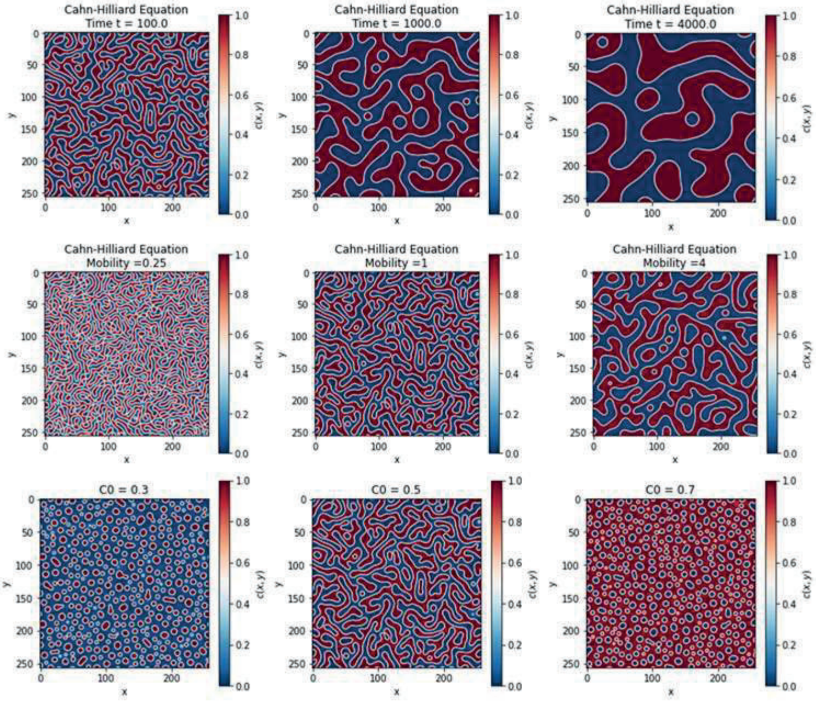

Figure 2-8 Phase inversion simulations of the VPP-PIPS process showcasing the effects of; time before solidification, molecular mobility and polymer concentration on the final membrane structure, based on Soares et al. and remade from Kirkebæk et al. ([182,205])

2.2.5 VPP-PIPS membranes

Therefore, ultimately VPP-PIPS shows itself to be a new possible method for membrane synthesis with controlled geometry via the chosen VPP type, controlled microstructure via PIPS and also tunable material (polymer) structure, with the general mechanisms of VPP-PIPS illustrated on Figure 2-9.

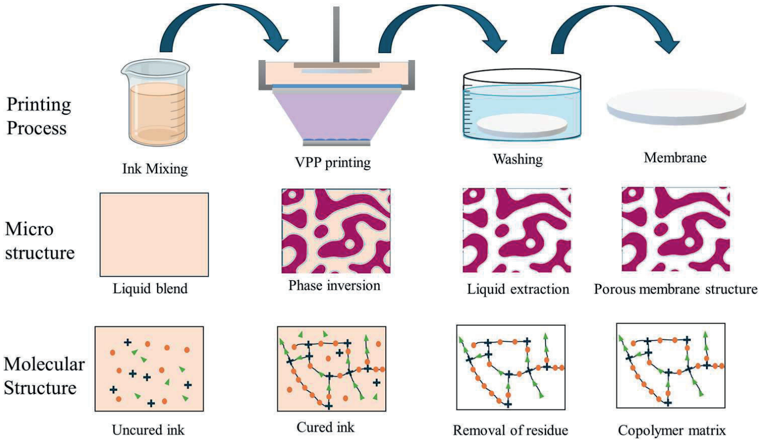

Figure 2-9, Illustration of controlled membrane geometry, micro structure and molecular structure (Paper[I])

Kirkebæk et al. [182] demonstrated that fully functional membranes can be produced using the VPP–PIPS approach with inexpensive, commercially available VPP printers. In their work, a commercially available resin (Anycubic Clear) was combined with bio-based decan-1-ol as a porogen. The resulting membranes required a post-treatment step involving acetone washing to remove unreacted resin and extract the porogen. The process is illustrated in Figure 2-10.

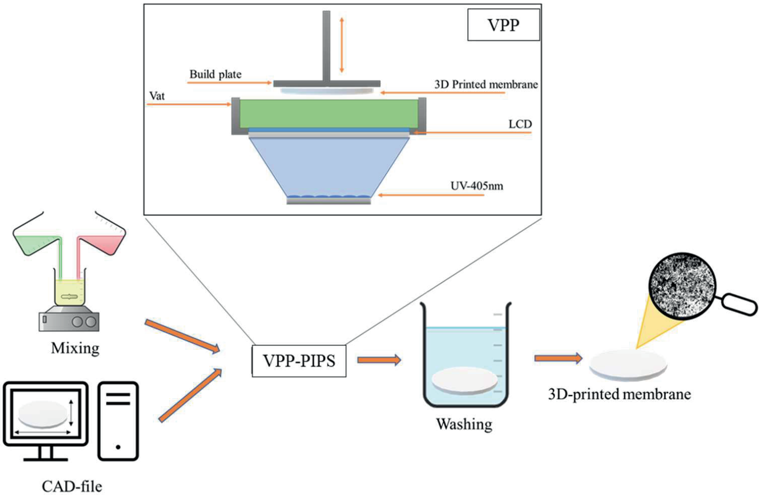

Figure 2-10, Schematic of 3D printing membrane of complex shape via the VPP-PIPS process [A1].

The membrane structure was shown to be influenced by porogen concentration, UV irradiation, and temperature, following trends predicted by Flory–Huggins and Cahn–Hilliard models for phase inversion. Key properties, including pore size, porosity, and water permeability, were fully tunable across ranges of <108 nm to 666 nm, 0.60 to 0.81, and 27 ± 4 to 1235 ± 45 LMH/bar, respectively. The membranes effectively rejected nanoparticle suspensions and, to some extent, bovine serum albumin, demonstrating suitability for microfiltration applications. Materials used in these membranes ([A1]) exhibited the high durability characteristic of thermosets. Thermal stability was confirmed up to approximately 200 °C, exceeding the requirements for MD and MCr processes, which typically require stability at 100 °C. Additionally, chemical resistance was evaluated in DMF, THF, acetone, and hexane, with the membranes showing no dissolution and negligible mass loss. These properties are illustrated in Figure 2-11.

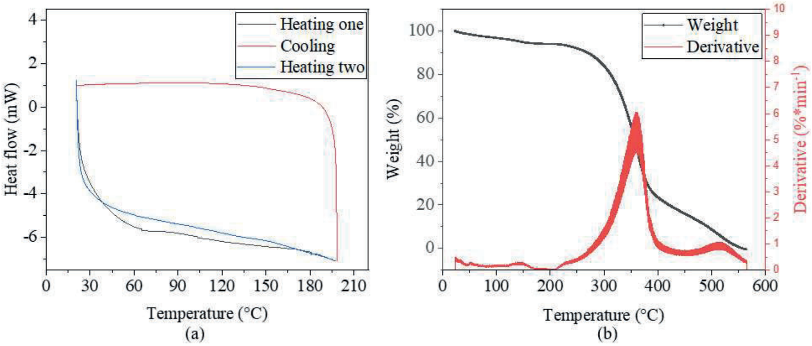

	m [g]	m_{loss} [g]	$\%m_{loss}$
DMF	0,227	0,006	2,6%
THF	0,410	0,012	2,9%
Acetone	0,266	0,006	2,3%
Hexane	0,445	0,009	2,1%

Figure 2-11, Top (a): A DSC curve obtained from a VPP-PIPS membrane. Top (b): TGA (black) and differential TGA of a VPP-PIPS membrane. Bottom: table of mass loss of a VPP-PIPS membrane after 24h submerging in different solvents [A1].

Therefore, VPP–PIPS has demonstrated strong potential as a method for producing durable, high-performance membranes. The combination of tunable pore sizes and excellent thermal stability makes these materials particularly relevant for MD and MCr applications and positions them as promising candidates for fully 3D-printed membranes with complex geometries. However, several challenges remain before VPP–PIPS membranes can be successfully implemented in MD/MCr systems. Although thermosets offer higher strength than thermoplastics, they are inherently brittle and lack flexibility [183,206,207]. This low flexibility reduces crack resistance, an issue that becomes more pronounced as membrane thickness decreases. Additionally, MD/MCr membranes must be dry during operation. Drying further increases brittleness due to changes in the glass transition temperature of multi-component systems, as described by the Fox and Flory–

Fox equations [208–210]. This often leads to increased fragility as seen on Figure 2-12.

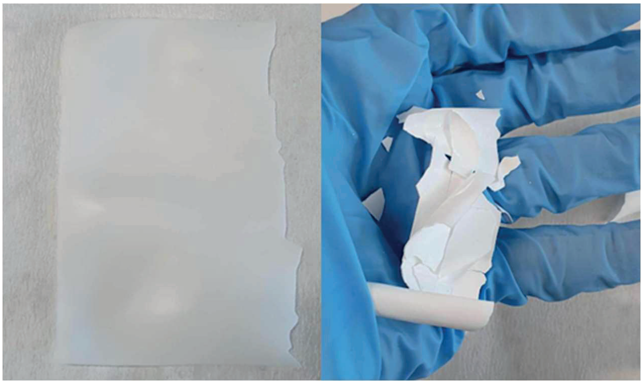

Figure 2-12. Left: a wetted flat sheet VPP-PIPS membrane. Right: Dry VPP-PIPS flat sheet membrane [A1].

VPP–PIPS is well suited for rapidly producing large, fully 3D-printed membranes with high resolution. The wide range of available materials offers significant advantages for membrane applications, particularly due to their thermal and chemical robustness. However, for successful use in MD/MCr, the inherent brittleness and low flexibility of VPP–PIPS membranes must be addressed. Consequently, it is essential to identify materials that are both mechanically strong and hydrophobic.

2.3. Tunable physicochemical properties via VPP-PIPS copolymerization

The following section elucidates the possibility to tune the physicochemical properties of membranes produced via VPP-PIPS to increase strength and hydrophobicity of the membranes. This section will mostly consist of data from paper (I).

2.3.1 Materials and methods

The ink used in VPP typically consists of a mixture of monomers or oligomers, crosslinkers, and photoinitiators. The monomers form the primary polymer backbone through radical polymerization, while crosslinkers enhance mechanical strength and photoinitiators accelerate curing [183,206,207]. Among these components, the monomers and oligomers primarily determine the physicochemical properties of the final polymer. When combined with other monomers or oligomers, the resulting material properties change accordingly, a process known as copolymerization. Unlike many other AM and membrane fabrication methods, VPP directly employs base monomers, providing the unique capability to tailor material properties through copolymerization. This approach enables an almost unlimited range of polymer formulations. Copolymerization in VPP has been shown to improve mechanical performance, including flexibility and strength. For example, incorporating polyurethane acrylates (PUA) can increase elasticity, allowing strains exceeding 50% [211], comparable to PTFE, a common material for MD/MCr membranes [212]. Such improvements could potentially be translated to VPP–PIPS membranes. In paper(I), a copolymerization of the PUA containing commercial ink is combined with either an ink based on 2-hydroxyethylmethacrylate(HEMA) which is highly hydrophobic or tert-butyl acrylate which is hydrophobic. The inks have the following compositions as shown on Table 2-1:

- **Ink One (HEMA-based):** 76% 2-Hydroxyethyl methacrylate (HEMA), 19% Trimethylolpropane triacrylate, 5% Irgacure 819.
- **Ink Two (PUA-based):** Commercial Flex resin containing 20% PUA, 42% AcM, 13% Tripropylene glycol diacrylate, 19% Ethoxylated trimethylpropane triacrylate, 2.4% Phosphine oxide, and 0.6% 4-Methoxyphenol.

- **Ink Three (tBA-based):** 76% tert-Butyl acrylate(tBA), 19% Trimethylolpropane triacrylate, 5% Irgacure 819.

Table 2-1, Ink compositions of different VPP-PIPS produced membranes copolymerized between (hydrophilic ink one, flexible ink two and hydrophobic ink three (Table from Kirkebæk et al.[213]) [Paper(I)].

Membrane Label	Ink one [m%]	Ink two [m%]	Ink three [m%]
F0	100	0	0
F20	80	20	0
F40	60	40	0
F50	50	50	0
F60	40	60	0
F80	20	80	0
F100	0	100	0
B0	0	100	0
B25	0	75	25
B50	0	50	50
B75	0	25	75
B100	0	0	100

The final ink was ultimately diluted to 40w% with porogen decan-1-ol to generate pores. Thereafter membrane discs of 1mm thickness and a 25 mm diameter were printed on a (Anycubic Photon mono 2) printer. The final discs would be washed for any remaining liquid ink/porogen in acetone, and subsequently dried at 105°C.

The produced membranes were characterized for their membrane properties; porosity, pore size, topography, micro structure, thickness and permeability via wetting/evaporation method, capillary flow porometry (Porelux 1000), confocal microscopy (Olympus OLS 4000 LEXT laser confocal microscope), electron microscopy (Zeiss evo 60 scanning electron microscope) ,micrometer measurement (Mitutoyo 543-391B micrometer) and dead-end filtration experiment respectively. The membrane physical characteristics; material composition, thermal resistance, mechanical strength and hydrophobicity/hydrophilicity of the printed membranes was determined by ATR-FTIR (Bruker Tensor II ATR-FTIR), thermal gravimetric analysis (TA SDT650), Tensile strength test and water contact angle measurements (Biotic Scientific Attention Theta Lite optical tensiometer) respectively.

2.3.2 Results and discussion

PUA based ink and HEMA based ink showed a successful copolymerization between the two as shown by its FTIR signature, as seen in Figure 2-13. Especially peak at 3416 cm^{-1} and 1465 cm^{-1} for -OH and -NH which are characteristic for HEMA and PUA respectively, showed a gradual change when changing the HEMA and PUA composition. FTIR therefore confirmed the suggested copolymerization through the VPP-PIPS process. This confirms the possibility of making membranes of a vast new number of polymers via VPP-PIPS.

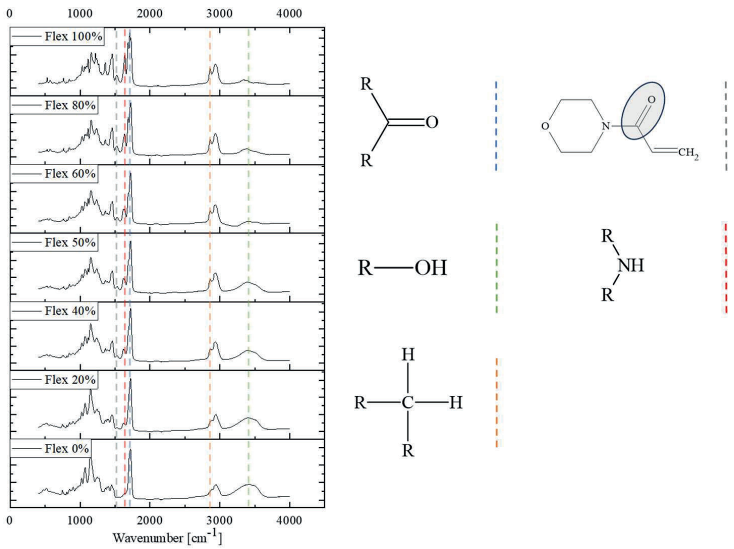

Figure 2-13. FTIR spectra highlighting the chemical signatures of the various co-polymerized VPP-PIPS membranes (F0 to F100), along with the corresponding functional groups assigned to the characteristic FTIR absorption peaks. (Illustration from Kirkebæk et al.[213])[Paper(I)].

2.3.3 Effects of Copolymerization on membrane properties

Membrane properties such as microstructure, porosity, pore size, and permeability were analyzed by evaporation method, capillary flow porometry and pressure induced water permeation respectively. Results which can be seen in Figure 2-14. There were found clear signs that the composition of the printing ink greatly affects the final membrane properties. This was expected as the PIPS process is affected by the solubility, molecular mobility and polymerization rate [182,200,214]. It was here seen that copolymerizing with PUA would gradually result in a denser membrane, with smaller pores, porosity and permeability. This densification reduced porosity from 0.65±0.01 (F0) to 0.47±0.03 (F100), alongside a drop in effective largest pore size from 319 nm to 119 nm and mean pore diameter from 171 nm to 46 nm. Consequently, the membrane transitions from microporous to mesoporous solely by altering ink composition. Also, a shrinkage from 27.2%±1.1% (F0) to 39.6%±3.4% (F100) with higher PUA composition was seen, which also relates to the densification. This opens for even further tune ability of membranes made via VPP-PIPS other than UV-irradiation, porogen concentration and temperature as suggested in Kirkebæk et al. [182] and could lead to denser membranes.

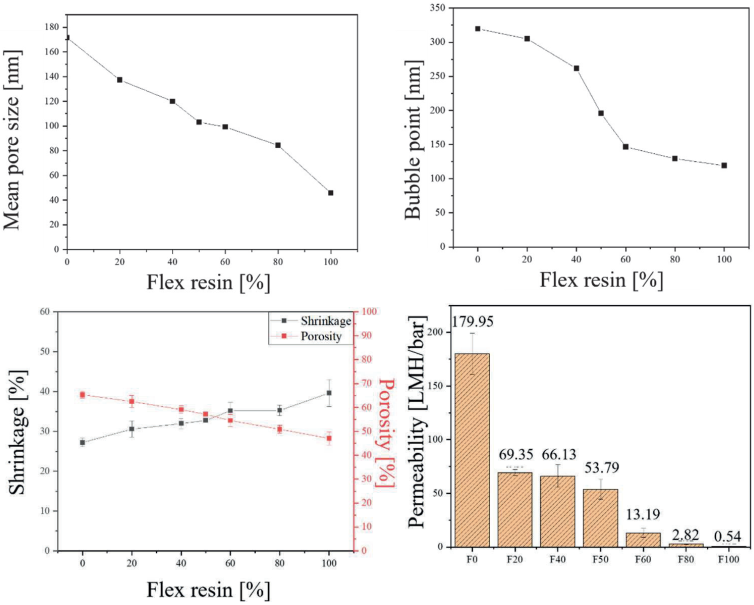

Figure 2-14, Top left: Mean pore diameter as a function of PUA-based ink concentration. Top right: Maximum pore diameter determined by bubble point measurements versus PUA-based ink concentration. Bottom left: Shrinkage and porosity for different concentrations of PUA ink. Bottom right: Permeability of various 3D-printed membranes, ranging from HEMA-based to PUA-based formulations (Illustration from Kirkebæk et al.[213]) [Paper(I)].

The membranes were analyzed using SEM to examine their porous structure, shown in Figure 2-15. As expected from phase inversion, the membranes display a porous morphology, with increasing densification from F0 to F100. This densification may stem from polymer de-mixing dynamics influenced by molecular mobility and solubility, as suggested by Kirkebæk et al. [182]. Micro-scale surface defects, likely caused by pixel-induced uneven polymerization in the LCD pixels from the VPP method, are present in all samples but decrease toward F0. Though difficult to avoid, these defects may enhance membrane roughness, potentially improving flux and adhesion [215–217]. Layering defects (~35 µm thick) are also visible in cross-sections. Despite these, SEM confirmed the porous structure, and performance tests showed the membranes function well as UF-MF membranes, comparable to those made by conventional phase inversion.

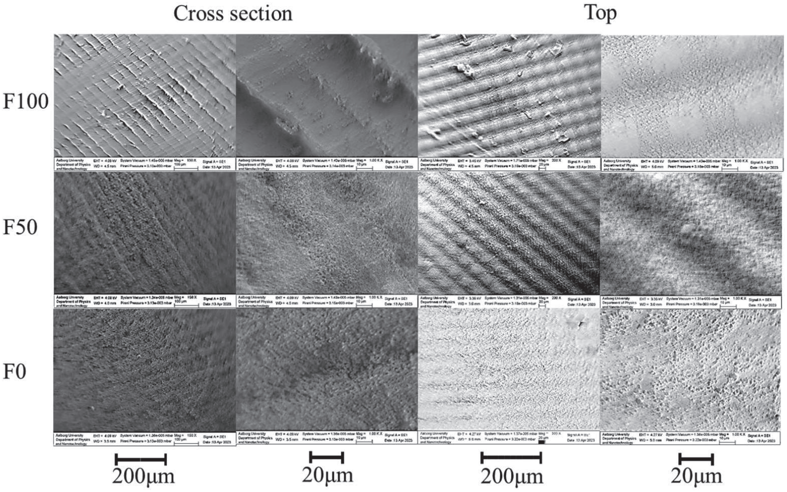

Figure 2-15, SEM pictures of cross section and membrane top for VPP-PIPS membranes F0, F50 and F100 (Illustration from Kirkebæk et al.[213])[Paper(I)].

2.3.4 Tuning of membrane physiochemical properties via Copolymerization

With the gradual change in composition of PUA and HEMA, it was hypothesized to gradually change the membrane physicochemical properties as well. Mechanical strength through tensile stress and thermal stability via TGA with a temperature ramp of 10K/min under atmospheric gas composition, were done on membranes with gradual different PUA/HEMA compositions (Figure 2-16). Mechanical testing reveals that higher PUA content markedly enhances strength and ductility. Brittle F0 (1.95 MPa, 1.02% strain) transitions to a tough, flexible material by F100 (21.2 MPa, 20.3% strain). Young's modulus also increases from 1.89 MPa to 13.03 MPa, indicating growing stiffness. Compared to conventional membranes like PSf (3.88 MPa), PVDF (2.19 MPa), and PP (25 MPa) [218–220], F100 approaches comparable strength. However, strain remains lower due to VPP-printed thermosets high crosslinking. Still, PUA copolymerization significantly enhances performance, suggesting further gains could be achieved by adding long-chain acrylates to the VPP-PIPS ink. Like mechanical strength, copolymerization also showed a large effect on the temperature stability of the produced membranes. Increasing PUA content was shown to improve thermal stability. The temperature for 10% mass loss rises from 260 °C (F0) to 345 °C (F100), with total degradation shifting from 562 °C to 664 °C. These values align with literature for HEMA and PUA [221] [222]. Differential TGA shows degradation begins near 240 °C, likely due to acrylate bonds common in both inks. While these bonds limit degradation resistance, the 240 °C threshold remains more than sufficient for most membrane processes (<100 °C), confirming suitability for various filtration applications [223].

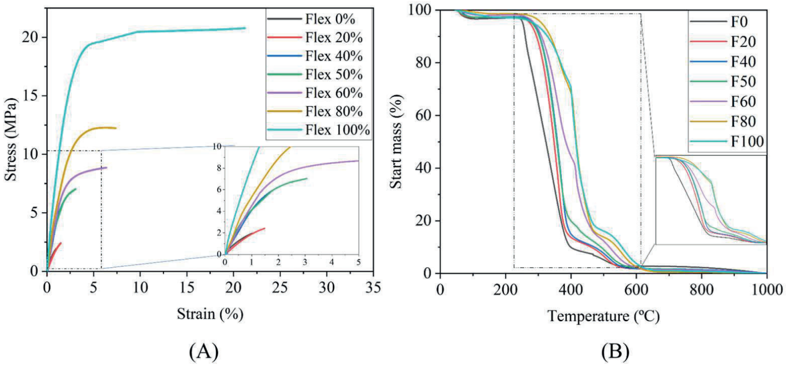

Figure 2-16, A: Tensile strength of different VPP-PIPS membranes copolymerized between HEMA based and PUA based inks. B: TGA decomposition of the same VPP-PIPS membranes (Illustration from Kirkebæk et al.[213])[Paper(I)].

Copolymerization therefore seems to be able to solve/alleviate the problems caused by brittleness inherent in the VPP-PIPS method and takes the method a step further to produce dried MD/MCr membranes which can be used at elevated temperatures. Hydrophobicity is still a problem which needs to be solved before utilization in MD/MCr can be achieved. Therefore, contact angle was measure on ink compositions of HEMA, PUA and t-butyl inks as in Table 2-1. It was revealed that copolymerization was a great tool for tuning the material surface tension. As can be seen in Figure 2-17, by gradually changing HEMA to PUA based ink the contact angle would go from 44.3º±4.0º to 66.2º±3.2º and by changing PUA to t-butyl a further gradual increase of contact angle was achievable up to 108.8°±2.6° was achieved, crossing the 90° contact angle needed for MD/MCr membranes to work. This suggests that there is a great deal of tune ability when it comes to surface tension via VPP-PIPS and with its superior thermal stability and improved mechanical strength could be very useful not only for MD/MCr but could further enhance other membrane applications due to its high tune ability between hydrophilic and hydrophobic properties [224,225].

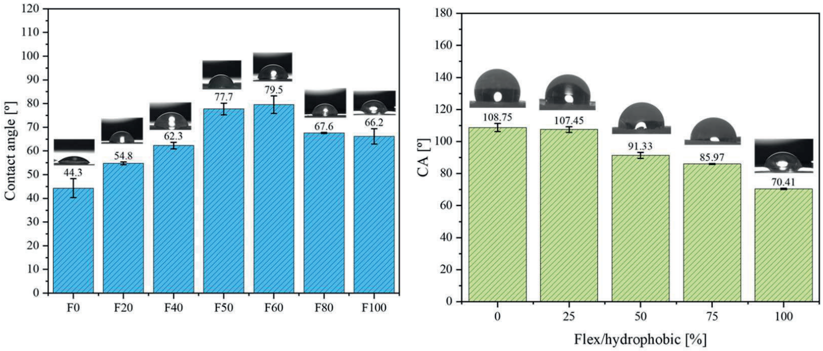

Figure 2-17, Left: Contact angle of different compositions of Ink one and two. Right: Contact angle of different compositions of ink two and three. Highlighting the full range of tune ability between hydrophilic and hydrophobic (Illustration from Kirkebæk et al.[213]) [Paper(I)].

2.3.5 Enhancing hydrophobicity via 3D printed topography

Since VPP offers high resolution printing, altering topography has been seen to further increase or decrease apparent contact angle. Therefore, to enhance membrane hydrophobicity, micro-topographies were 3D printed onto membranes using a high-resolution open source DLP-VPP printer developed at Technical University of Denmark, forming small 10 mm × 20 mm membranes with 70 µm pillars spaced 70 µm apart. Pillars were printed with varying layer curing times (1600 ms to 200 ms) to adjust resolution and avoid overcuring. Shorter curing times produced more defined structures, increasing the contact angle from 97.8° ± 1.4° (flat surface) to 136.8° ± 1.0° (200 ms exposure), as shown in Figure 2-18. Longer exposures caused overcuring and blurred features, reducing hydrophobicity. The observed wetting behaviour followed the Wenzel state, with water infiltrating the pillars likely due to excessive spacing. Reducing this could improve performance [226]. These results align with Li et al.'s simulations [227] and highlight that VPP-printed surface roughness can tune membrane wettability, with implications for controlling fouling, crystallization, and adhesion in membrane applications [228,229].

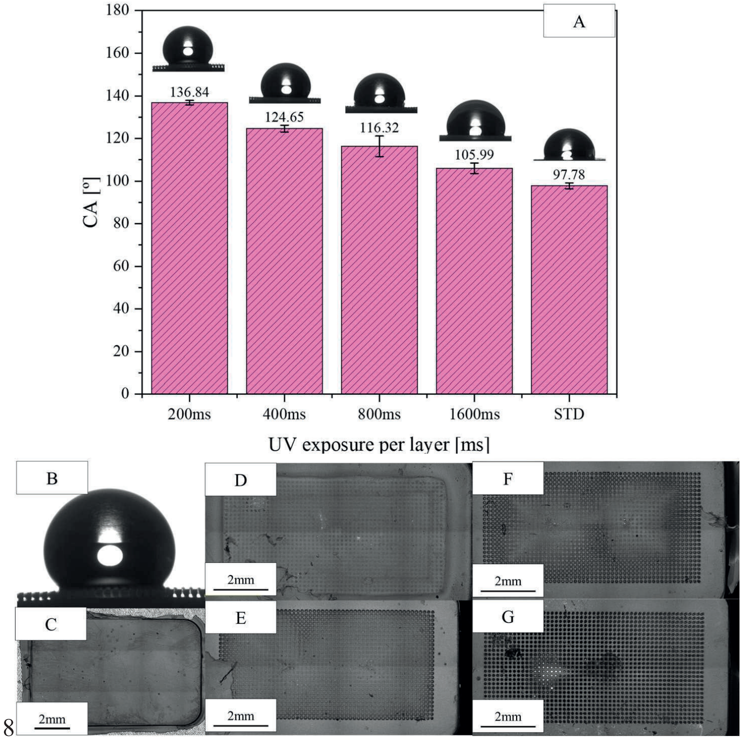

Figure 2-18, Hydrophobic VPP-PIPS membranes with AM printed micro topography produced by DLP and pure ink three. A: Contact angle of different layer hardening time. B: picture of water droplet on 200ms membrane. C, D, E, F and G are top pictures of STD, 1600ms, 800ms, 400ms and 200ms respectively (Illustration from Kirkebæk et al.[213]) [Paper(I)].

Further attempt on making even smaller topological also attempted with the hydrophobic ink (B100). However, due to overexposure gel can also be seen to develop between the pillars, here simply lowering the exposure time was not possible as the fragility of the porous membrane material would not form a coherent structure strong enough for the VPP process and would end up breaking through the printing process. It also becomes less practical as the smaller the details ultimately would result in smaller membranes possible to print. This plays back to the tradeoff between resolution and printing area.

2.3.6 Summary

The work described in this section represents a step forward toward printable MD/MCr membranes. Fully 3D-printed, porous, hydrophobic discs were fabricated and successfully dried, demonstrating all the essential properties for MD/MCr applications while also being free of PFAS-containing materials. This study further illustrates that copolymerization can be used to readily tailor physicochemical properties, an advantage relevant to nearly all membrane processes. In particular, the ability to adjust hydrophobicity is highly beneficial for MCr, as heterogeneous nucleation depends on interfacial tension and surface interactions. Additionally, this work showed that surface microstructuring during VPP printing, such as incorporating micropillars, can further increase hydrophobicity by modifying the contact angle. While some challenges remain, including improving resolution and mitigating overexposure, further advances could enable the direct fabrication of submicron pores (<1 μm).

2.4. Fully 3D printed VPP-PIPS membranes for MD/MCr

With the hydrophobic VPP-PIPS material sourced in section 2.3. it is possible to make both dry, porous and hydrophobic membranes. In this section fully 3D printed membranes via VPP-PIPS are made and evaluated in a MD/MCr system. This section is primarily based on paper (II).

2.4.1 Materials and methods

The hydrophobic porous membrane material found in the previous section was found to still be too fragile to be used due to the brittleness when dried. Therefore, tubular shapes were favored to produce fully 3D printed desalination membranes. Tubular membranes (7.5 cm length, 1 cm inner diameter, 1.5 cm outer diameter) were designed in CAD and printed using three ink formulations with varying polymer concentrations: 40/60, 50/50, and 60/40 (Ink B100 with decan-1-ol), resulting in membranes M-40, M-50, and M-60. To study wall thickness effects, membranes were also made with 5 mm, 7.5 mm, and 10 mm walls. Additionally, a rifled membrane (M2) was created to promote turbulence. All membranes were sliced in Chitubox and printed with commercial printer (Anycubic Photon mono 2) with a 50 µm layer height and 20 s curing time. Details of the different produced tubular membranes can be seen on Table 2-2.

Table 2-2, Naming of different tubular membranes depending on their Inner diameter, Ink/porogen composition and cross section type. Bottom picture depicts the different Cross section types [Paper(II)].

Name	**Inner diameter**	**Ink concentration**	**Cross section**
M-40	10mm	40%	Type A
M-50	10mm	50%	Type A
M-60	10mm	60%	Type A
5 mm	5mm	40%	Type B
7.5 mm	7.5mm	40%	Type C
10 mm	10mm	40%	Type A
M2 (riffled)	10mm	40%	Type D
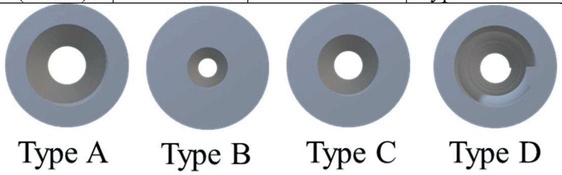			

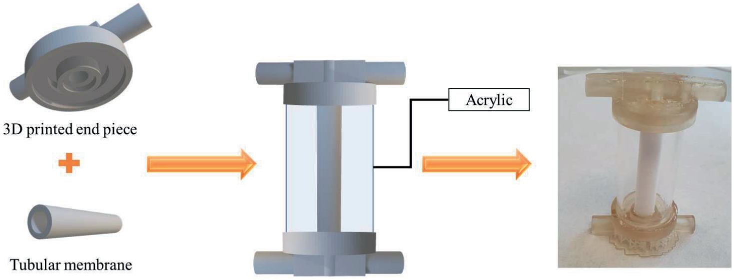

Figure 2-19. Illustration of assembly of tubular VPP-PIPS membrane in a 3D printed housing for DCMD module [Paper(II)].

The produced membranes were characterized for it membrane properties; porosity, micro structure and thickness via wetting/evaporation method, electron microscopy (Zeiss evo 60 scanning electron microscope) ,micrometer measurement (Mitutoyo 543-391B micrometer) and dead-end filtration experiment respectively. The membrane physical characteristics; material composition, thermal resistance, mechanical strength and hydrophobicity/hydrophilicity of the printed membranes was determined by ATR-FTIR (Bruker Tensor II ATR-FTIR), thermal gravimetric analysis and differential scanning calorimetry (STA 449 F5, Netzsch), Tensile strength test and water contact angle measurements (Biotic Scientific Attention Theta Lite optical tensiometer) respectively. The membranes were then tested in a DCMD setup with DI-water as permeate solution and), NaCl(Sigma) as a model solute for the feed.

2.4.2 Membrane characteristics

The produced tubular membrane would be fixed in a 3D printed module. The tube ends of the membrane would be glued to the 3D printed end pieces with epoxy glue. Secondary an acrylic shell would be glued to the outer ring of the end pieces, resulting in a transparent shell and a module as seen in Figure 2-19. Initially, the printed membranes appeared yellow (Figure 2-20(A)) but turned white after solvent washing and thermal drying (Figure 2-20(B), indicating effective removal of porogens and unreacted components typical of polymeric membranes. All membranes were fabricated using VPP-PIPS with 300 layers, taking about 2 hours total (approximately 0.67 hours per membrane). Since print time depends on the z-axis height, increasing the x- or y-axis (build plate) could scale up production without increasing print time. Showcasing the scalability of the method. ATR-FTIR spectroscopy (Figure 2-20(C)) confirmed the presence of tert-butyl acrylate (tBA) with TMPTA in the final polymer, showing characteristic peaks at 2968 cm^{-1} (CH_3 stretching), 1721 cm^{-1} (C=O stretching), and 1158 cm^{-1} (C–O–C linkages). The enhanced CH_3 signal supported tBA incorporation. The resulting membranes also showed strong hydrophobicity.

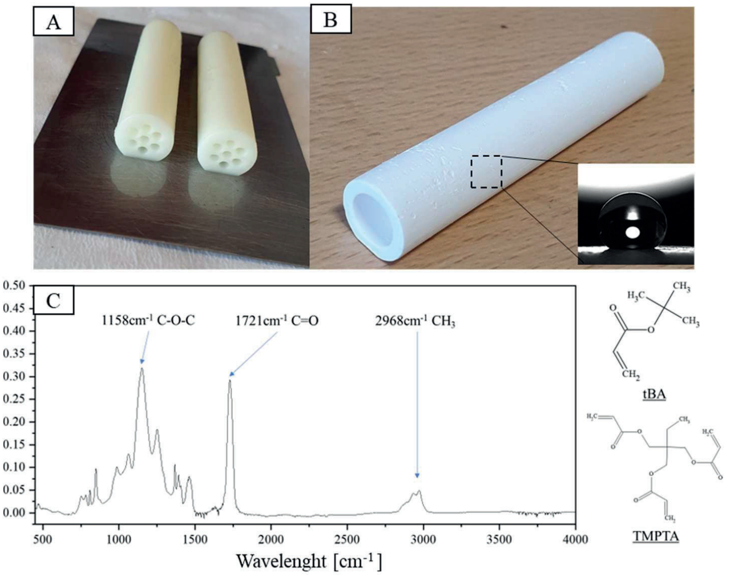

Figure 2-20, A: picture of a VPP-PIPS tubular membrane design on a detachable build plate. B: A dried VPP-PIPS tubular membrane fully stable, with a picture depicting its water contact angle. C: FTIR signature of the membrane showcasing the membrane signature and successful polymerization of tBA and TMPTA [Paper(II)].

Porous structure is essential for membrane distillation (MD), which typically requires pore sizes in the microfiltration (MF) range of 0.1–1.0 µm. SEM cross-sectional images (Figure 2-21(A–D)) confirmed that the printed membranes exhibit a porous, nodule-based morphology characteristic of phase inversion in the binodal region similar to that seen in ceramic membranes and previously reported VPP-PIPS membranes from the earlier section. The internal structure appears asymmetric, with visible horizontal layering (~23 µm thick) due to the layer-by-layer stereolithography process. Surface pore size analysis using ImageJ on Figure 2-21(D) yielded a mean Feret diameter of 438.1 nm, with a median of 324.5 nm and mode of 192.0 nm. While these measurements are from the surface and may overestimate average pore size due to membrane asymmetry, they still fall well within the MF range appropriate for MD. Porogen concentration significantly affected porosity. As shown in Figure 2-21(F), increasing porogen content resulted in higher porosity values: 0.46 ± 0.01 (M-60), 0.59 ± 0.01 (M-50), and 0.68 ± 0.00 (M-40). Only M-40 exceeds the 0.65 threshold typically desired for MD performance [230,231]. Although increasing porogen further could improve porosity, this may compromise mechanical strength, posing challenges for thinner or more delicate membranes. Contact angle measurements (Figure 2-21(G)) showed high hydrophobicity across all membranes, ranging from 122.9° ± 9.9° to 144.2° ± 5.2°, well above the 90° minimum for MD [232]. While no direct correlation was observed between porosity and contact angle, the top surfaces consistently showed higher contact angles than the plate-facing sides. This asymmetry may be due to differences in surface smoothness.

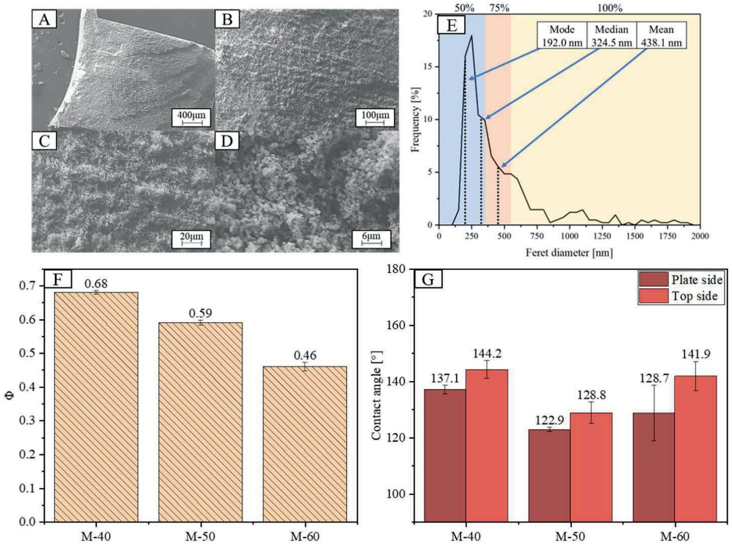

Figure 2-21, A, B, C and F: Different SEM pictures of a cross-section of an M-40 membrane at different zooms. E: Image-J pore size analysis of the M-40 membrane. F: porosity of M-40, M-50 and M-60 membrane. G: Contact angles of discs made in under same conditions as M-40, M-50 and M-60, Top and plate sides refer to the side facing upward and the side attached to the build plate respectively [Paper(II)].

MD membranes must withstand temperatures up to 100 °C and maintain mechanical integrity under operational stress. Thermal and mechanical properties were evaluated using DSC-TGA and tensile testing (Figure 2-22). DSC-TGA (Figure 2-22(A)) showed two mass loss events: one at ~246 °C (residual porogen evaporation) and another starting at ~300 °C (polymer decomposition), indicating thermal stability up to 300 °C. This exceeds common MD membrane materials like PP (163 °C) [233] and PVDF (171 °C) [234], and is comparable to PTFE (327 °C) [235]. The thermoset matrix also ensures thermal dimensional stability below Tg, minimizing deformation over time. Mechanical tests (Figure 2-22(B–D)) revealed high rigidity and brittleness typical of thermosets. M-40 had a Young's modulus of 0.94 MPa and a yield strain of 0.81%, much lower than PP (~3.1 MPa, ~30% strain) [236]. Reducing porogen content improved mechanical properties raising modulus to 3.67 MPa and yield strength to 3.51 MPa but flexibility remained limited. These results suggest that thick-walled or reinforced membrane designs are necessary to overcome brittleness.

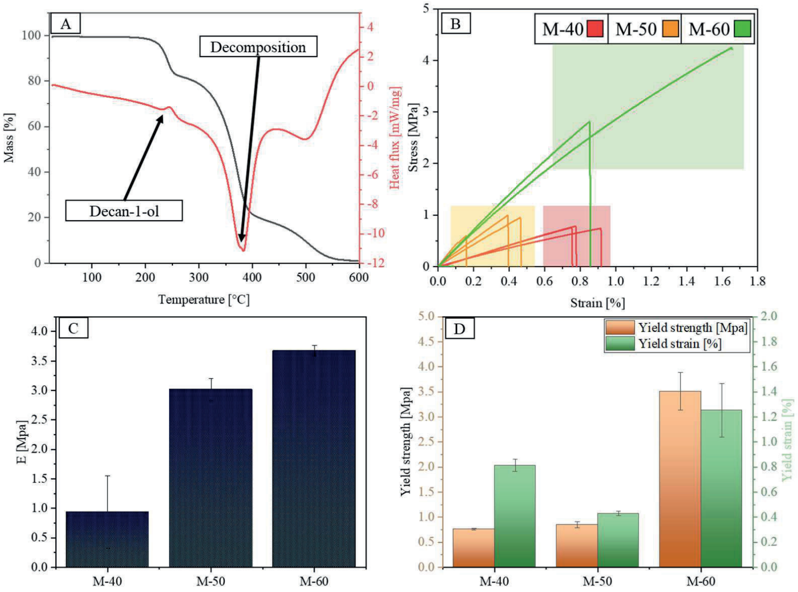

Figure 2-22, A: TGA (Black) and DSC (Red) of a piece of M-40 membrane. B: Tensile strength of M-40 (red), M-50 (orange) and M-60 (green). C Youngs modulus of same membranes. D: the same membranes Yield strength (orange) and yield strain (green) [Paper(II)].

2.4.3 Membranes for DCMD MD/MCr

Therefore, the tubular membranes were characterized to be suitable for MD, the membranes were fixated in 3D printed modules and subsequently tested in a DCMD setup with demineralized water with a temperature profile explained in Table 2-3. The M-40 membrane was tested for water transport in a DCMD setup at feed temperatures of 60 °C, 70 °C, and 80 °C (cooling side at 15 °C), and flow velocities of 4.26 to 26.25 m/s. A second membrane, M2, with internal rifling for turbulence promotion, was also tested with the same conditions. Both membranes showed stable performance with flux increasing at higher feed temperatures (Figure 2-23). M-40 flux rose from 2.10 to 5.93 LMH (60 °C to 80 °C), while M2 increased from 0.89 to 4.43 LMH. Notably, M2 outperformed M-40 at low velocity but declined at higher velocities, likely due to the rifling disrupting flow and increasing resistance. Pressure normalized flux (K) revealed a small increase for M-40 with velocity (e.g., 12.25 to 14.59 LMH/bar at 80 °C), but a consistent decline for M2, confirming the negative impact of rifling at high shear rates. While M2's turbulence design did not enhance performance here, it demonstrates the capability of VPP-PIPS to create complex internal geometries, offering potential for future optimization.

Table 2-3, Table of inlet feed temperatures (T_f) and permeate temperature (T_p), For membranes M-40 and riffled M2 setup in a DCMD setup running DI-water at either 60°C, 70°C or 80°C [Paper(II)].

M-40 (60°C)	T_f=57.5°C ±0.6°C, T_p=16.7°C ±0.1°C	M2 (60°C)	T_f =57.7°C ±0.5°C, T_p =16.7°C ±0.0°C
M-40 (70°C)	T_f =67.0°C ±0.3°C, T_p =16.9°C ±0.1°C	M2 (70°C)	T_f =67.0°C ±0.1°C, T_p =16.5°C ±0.0°C
M-40 (80°C)	T_f =76.3°C ±0.1°C, T_p =16.9°C ±0.1°C	M2 (80°C)	T_f =76.5°C ±0.1°C, T_p =16.8°C ±0.0°C

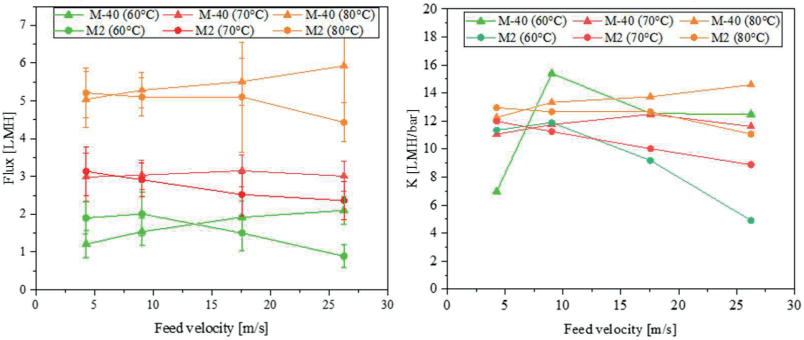

Figure 2-23, Left is DI-water flux of M-40 and M2 membrane at 60°C (green), 70°C (red) or 80°C (orange). Right, graph of membrane permeability (K) of M-40 and M2 at 60°C (green), 70°C (red) or 80°C (orange) [Paper(II)].

Porogen concentration was characterized to have a large effect on the membrane porosity (Figure 2-24(B)). Reducing porogen content from M-40 to M-60 lowered porosity and significantly decreased flux: from 5.62 LMH (M-40) to 0.71 LMH (M-50), and near zero for M-60. The dramatic drop suggests not only reduced porosity but also increased tortuosity or decreased pore connectivity. While lower porogen improves strength, it severely limits vapor transport. Membranes were made with wall thicknesses ranging from 5 to 10 mm (Figure 2-24(C)). Increasing thickness modestly reduced flux (from 5.62 to 4.46 LMH), which was expected due to the increased mass transfer length through the membrane. This is supported by literature [237]. However, thicker walls lower membrane packing density, reducing water output at scale. VPP-PIPS enables tuneable membrane properties through control of porogen content, wall thickness, and geometry. Optimizing porosity and thickness could enhance MD performance, but current brittleness requires mechanical improvements before implementing thinner designs. In MD desalination, it is crucial that the membranes show high resistance to fouling and wetting and water flux at elevated salinities, especially NaCl which is the main component of seawater is of interest. Therefore, the M-40 membrane was tested with NaCl feed concentrations of 0–250 g/L. Flux decreased from

5.93 to 3.71 LMH as salt concentration rose, consistent with the relationship between water activity and NaCl concentration as observed by Jenkins *et al.* [238]. However, reductions exceeded predictions due to concentration polarization at the membrane surface. Despite this, the membrane retained 81% flux at 100 g/L and 62% at 250 g/L. Salt rejection remained excellent, with permeate conductivity only increasing by 0.32 µS/cm (~0.16 mg/L NaCl), far below reverse osmosis levels (~100mg/L to 300 mg/L) [239–241].

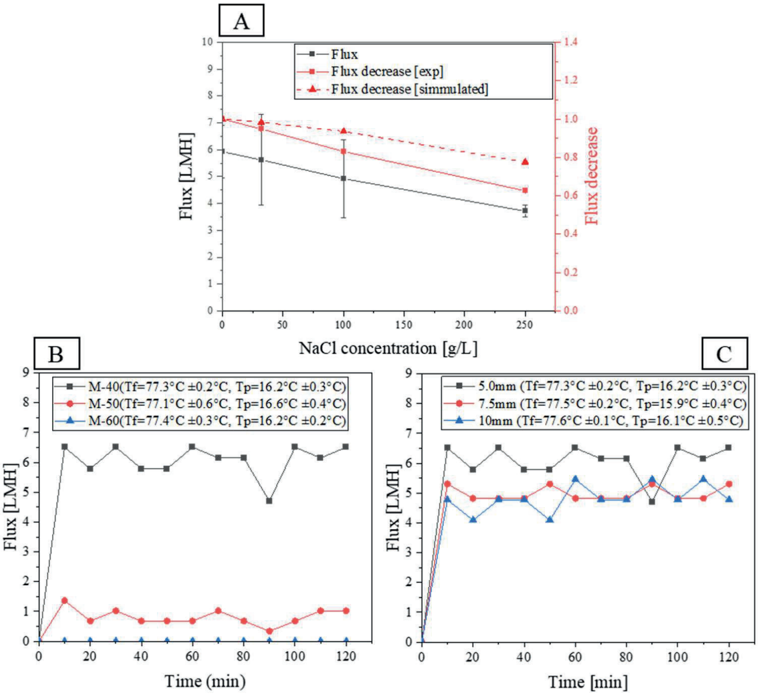

Figure 2-24. A: Flux (Black) of a M-40 membrane at different NaCl as well as a theoretical (solid red) and experiment (dotted red) flux decline in percentages depending on NaCl concentrations. B: flux graphs of M-40, M-50 and M-60 membranes. C: Membrane flux of membranes with different inner tubular diameters.

To assess suitability and competitiveness of the VPP-PIPS membranes for MD/MCr, the M-40 membrane was tested under hypersaline conditions (100 g/L NaCl at 80 °C) and compared to a commercial 0.2 μm (Pall) PTFE membrane (Figure 2-25(A-B)). Although the Pall membrane had higher initial flux (10.24 LMH vs. 5.79 LMH), it eventually failed due to pore wetting and salt breakthrough, indicated by a sudden flux spike and conductivity increase. In contrast, M-40 maintained stable flux and low conductivity, showing superior fouling and wetting resistance, attributed to its greater thickness and thermally resistant thermoset material. Further to test the membrane suitability for ZLD and MCr, a prolonged experiment at elevated concentrations of 250 g/L NaCl feed until crystallization and beyond was done with the standard M-40 membrane (Figure 2-25(C)). The membrane operated stably for 25.6 hours before crystallization caused a sharp flux drop. This is likely due to membrane scaling and resulted from local concentration and temperature polarization promoting early nucleation. Despite scaling, M-40 maintained high salt rejection (>99.99%) and water quality throughout the experiment. These results confirm the membrane's strong potential for MCr and ZLD applications. While scaling ultimately halted flux, further performance gains could be achieved by tuning membrane-crystal interactions via surface topography an approach shown feasible with VPP-PIPS.

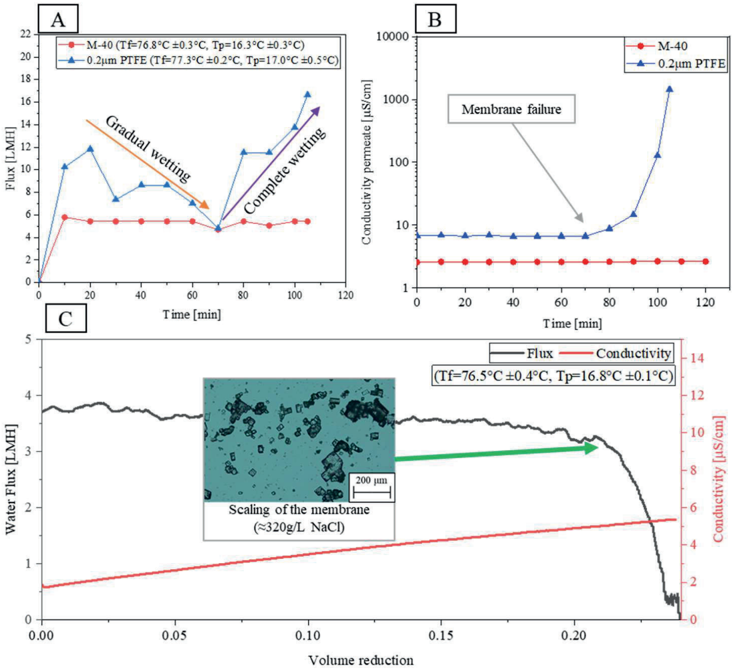

Figure 2-25. A: Comparison of performance between 3D printed VPP-PIPS membrane and a 0.2µm Pall PTFE membrane in the form of a DCMD experiment at 80℃ and 100g/L. B: Permeate conductivity of the two membranes showcasing wetting of the 0.2µm Pall PTFE membrane. C: Long term experiment of M-40 at 80℃ and a starting salinity of 250g/L. Black line depicts membrane flux and red line the permeate conductivity. Picture of produced NaCl crystals is depicted at the point of crystallization [Paper(II)].

2.4.4 Summary

Novel, fully 3D-printed VPP–PIPS hydrophobic tubular membranes were developed in this work. These membranes exhibit tunable porosity and mechanical strength while enabling the fabrication of geometries previously difficult or impossible to achieve. The process was demonstrated to be highly scalable and produced membranes competitive with conventional materials such as PFTE, while remaining PFAS-free. The tubular membranes proved well-suited for desalination of NaCl brines across a range of concentrations, from seawater levels to hypersaline conditions approaching supersaturation. They also showed excellent resistance to wetting even after crystallization, indicating strong potential for ZLD applications. However, the rapid decline in flux to near-zero LMH during operation will need to be addressed to render these membranes fully viable for ZLD processes.

2.5. Enhancing membrane properties with VPP-PIPS topography

Mechanical strength remains a challenge for VPP–PIPS membranes, and fabricating highly complex, fully printed membrane structures is still difficult. However, the potential benefits of 3D printing have not yet been fully explored. Accordingly, the following section investigates an alternative approach: directly printing topographies onto pre-existing membranes to create inherently porous spacers that enhance membrane performance. This work is primarily based on Paper (III).

2.5.1 Porous spacers through VPP-PIPS

From the previous sections VPP-PIPS revealed itself to be suitable for MD/MCr membranes, it was both possible to have a reasonable water flux even when approaching/reaching crystallization point. Though possible to use for desalination and possibly crystallization of NaCl, the material brittleness is still high. Decreasing porogen concentration improves the membrane strength greatly, the flux also lowers to a point where the almost no water passes through. Therefore, membranes made via VPP-PIPS still need some improvements before it is possible to fully print MD/MCr membranes.

Directly printing on already preexisting membranes could overcome this issue, by using the strength from the membrane but retaining the possibility to generate complex topography which can benefit membrane processes by affecting the laminar layer and interfacial tension of the membrane. This could benefit MD/MCr by manipulating crystallization and concentration/temperature polarization. Spacers are known to also have this function and are known to add anti-fouling and increased flux for membrane processes. While spacer's primary function is to maintain separation between membrane sheets, spacers have also been shown to reduce fouling and concentration polarization by disrupting laminar flow and promoting mixing [242,243]. Usually, Spacers are made by making a polymer mesh which can rest on top of the membrane surface. One of the key challenges for spacers is the reduction in water transport at the contact points between the membrane and the spacer [244,245]. To address this, inherently porous spacers have been proposed by Yazan Ibrahim et al [246]. who demonstrated that a porous spacer could function partially as a membrane, facilitating water transport through the contact zones and thereby mitigating the performance loss. With VPP-PIPS it is possible to print porous membranes, which could be used as novel spacers fully integrated with the membrane, with increased control over spacer geometry, porous structure and physicochemical properties. Furthermore, making porous spacers inherent in the membrane via VPP-PIPS could be a steppingstone to generate spacers or advance topography for MD/MCr purposes. However, due to the necessity to dry the porous VPP-PIPS membranes for MD/MCr at ≥100°C, an easier first step to demonstrate these VPP-PIPS spacers/topography in a pressure driven process in order to keep the membrane wetted.

2.5.2 Materials and methods

To fabricate inherently porous spacers, a 1:1 mixture of clear Anycubic resin and decan-1-ol was mixed together. Spacer designs were created in SolidWorks, sliced in Anycubic Photon Workshop, and printed on an Anycubic Photon Mono 2 SLA printer (50 µm layer height; UV exposure: 20 s for base layers, 8 s for others). A magnetic and flexible steel build plate was modified to fixate an Alfa Laval-MFG2 membrane to enable direct printing onto its surface. Depending on the spacer type, either the porous resin mix or standard resin was used. After printing, all membranes (porous, dense, pristine) had to be cleaned in a 1:1 acetone and propan-2-ol solvent for 24 h, then rinsed with deionized water for 30 min. The stepwise method can be seen in Figure 2-26.

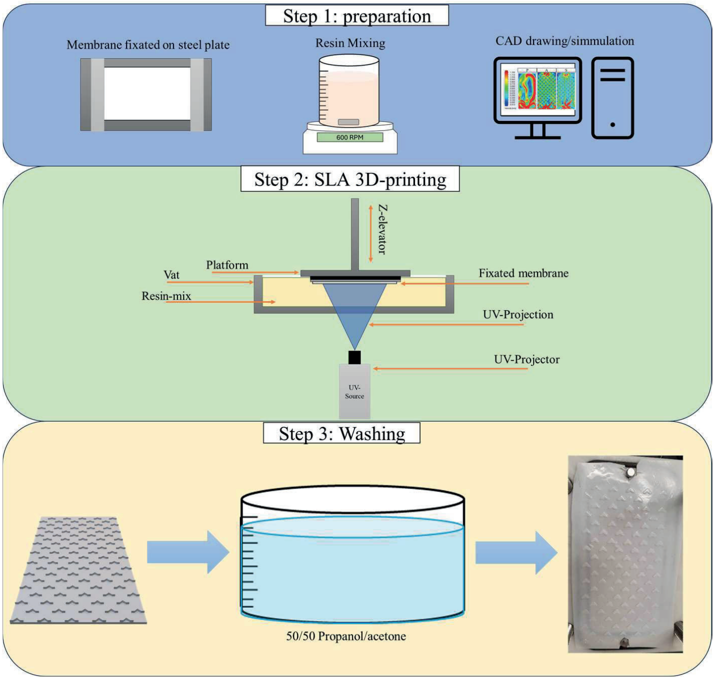

Figure 2-26: Key steps involved in making the inherently integrated spacers on commercial membranes.

With this method it was possible to generate MF-membranes with porous and non-porous (without porogen) spacers. Spacers were chosen based on their Solidworks fluid dynamics simulation and prior art, which suggests these will disrupt laminar flow near the membrane [247,248]. Figure 2-27 shows both fluid dynamics and produced membrane spacers.

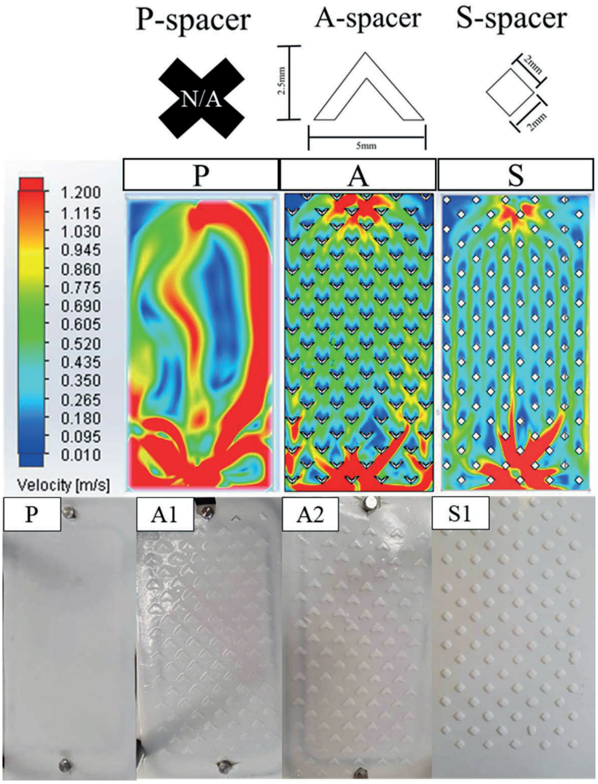

Figure 2-27. Top: illustration of different spacer names P, A and S and their subsequent dimensions. Middle: CFD simulations of membranes with either a P, A and S spacer. Bottom: Picture of P membrane (pristine) and membranes with VPP-PIPS produced spacers, A1 (non-porous arrow), A2(porous arrow) and S1 (porous square) spacer [Paper(III)].

The produced membranes were characterized for their membrane properties; porosity, pore size, micro structure and thickness via wetting/evaporation method, capillary flow porometry (Porelux 1000), electron microscopy(Zeiss evo 60 scanning electron microscope) ,micrometer measurement (Mitutoyo 543-391B micrometer) and dead-end filtration experiment respectively. Pure water flux was determined in a deadend filtration setup (Sterlitech HP4750) tested with DI-water. Crossflow experiments were conducted with a model solution of yeast cells and DI-water which can be seen in Figure 2-28.

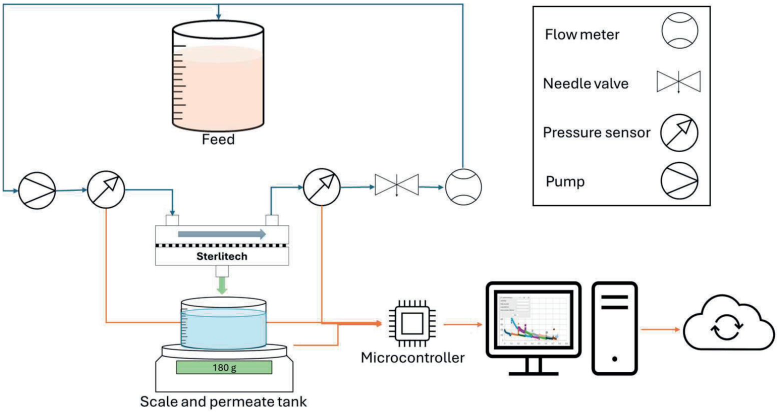

Figure 2-28: Crossflow system with a sterlitech crossflow cell, two pressure meters, a pump, feed tank, scale and online data-logging system [Paper(III)].

2.5.3 VPP-PIPS inherent spacer characteristics

In order to confirm the porous structure of the membranes and their VPP-PIPS produced spacers. Electron microscopy was used. SEM images at 25×, 1000×, and 4000× revealed clear structural differences among the pristine membrane (P), the non-porous spacer (A1), and the porous spacer (A2) (Figure 2-29). P showed large surface pores (~1 µm) transitioning to smaller internal pores (~175 nm), while A1 appeared fully dense with no visible porosity. In contrast, A2 exhibited a sponge-like, interconnected porous network resembling the pristine membrane, though with elongated, fibril-like voids due to its fabrication via polymerization-induced phase separation (PIPS), unlike the circular pores from the NIPS process used for P. These findings confirm that A2 successfully mimics membrane-like porosity, supporting the potential of PIPS-based VPP printing to create integrated, porous spacers that may improve water transport and reduce fouling.

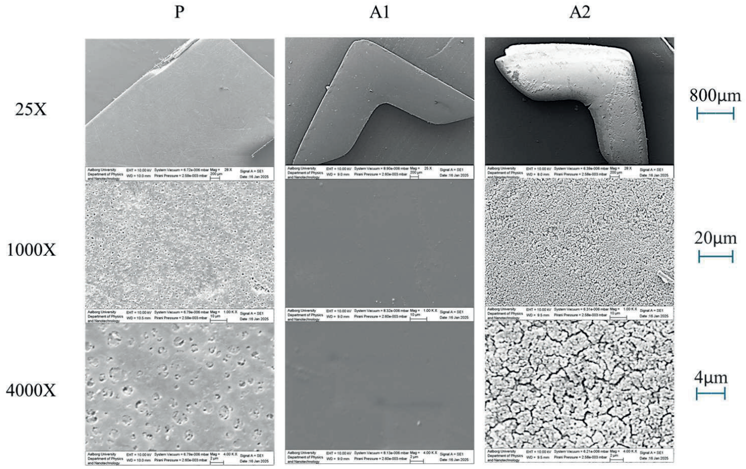

Figure 2-29. SEM pictures of P, A1 and A2 at 25x, 1000x and 4000x zooms [Paper(III)].

Further analysis of the membrane properties of porosity and pore size was also performed to explore the effects of the spacers on these properties as seen in Figure 2-30. The inherent porosity of the membranes was analyzed by a porosity analysis, where it was found that the porosity of the spacers was close to the 42.4 ± 3.7% of the membrane itself (45.2 ± 2.7% ; A1. 50.4 ± 5.8% ; S1). Without porogen it was still possible to print topography, but the porosity would be low at 1.3 ± 0.7%. The pore size of the membranes with and without the added pores were tested by capillary flow porometry. Modified membranes with added spacers showed a decreasing trend in average pore size: 225.5 ± 15.9 nm (P; pristine membrane), 175.9 ± 10.4 nm (A1; non-porous spacer), 155.3 ± 8.7 nm (A2; porous arrow spacer), and 134.5 ± 16.9 nm (S; porous square spacers). While porous spacers generally reduce mean pore size, their broader and overlapping pore size distributions suggest the reduction is directly linked to the porous topography itself. Small shrinkage was observed on the spacers themselves, although spacer height was set to 1000 µm, actual heights were 753 µm (A1), 699 µm (A2), and 646 µm (S). The reduction is likely due to porous structure collapse, membrane gelling, and the use of a 200 µm flexible build plate. Some compensation is therefore necessary for improved spacing control between the spacers.

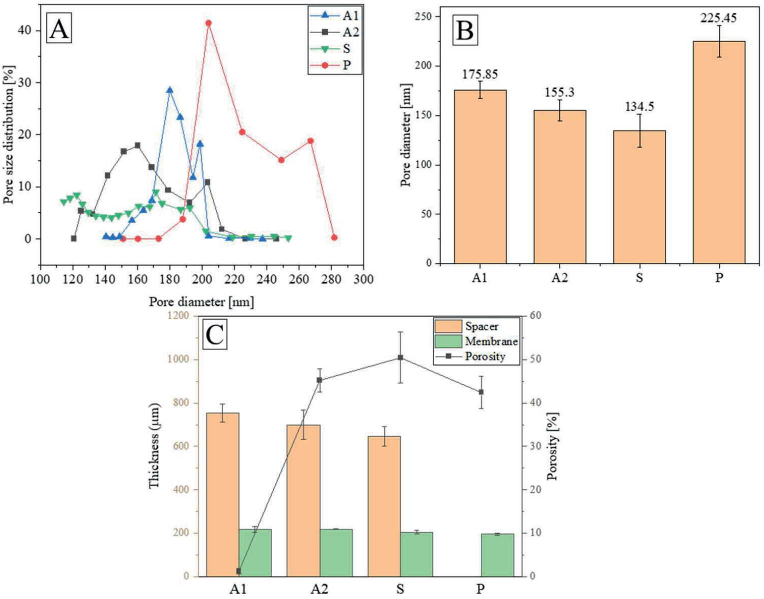

Figure 2-30. A: pore size distribution of A1 (blue), A2 (black), S (green) and P (red). B: Resulting mean pore size of A1, A2, S and P membranes. C: Thickness of membrane (green) and membrane + spacer (orange) of A1, A2, S and P membranes as well as their porosities on the second y-axis.

2.5.4 MF performance with VPP-PIPS made spacers

Membranes P (pristine), A1 (non-porous spacer), and A2 (porous spacer) were tested in MF a crossflow system using a 5 g/L yeast solution to evaluate performance under high fouling conditions (Figure 2-31). All membranes were pre-flushed with demineralized water for one hour for baseline consistency. Permeability dropped significantly due to fouling, with P, A1, and A2 showing values of 247.0, 107.6, and 1758.5 LMH/bar respectively. Corresponding cake resistances were 3.78×10^5, 9.62×10^5, and $0.30 \times 10^5\ \text{m}^{-1}$. These results confirm that fouling heavily impacts performance and that adding a spacer does not automatically improve flux since the dense spacer didn’t improve flux much. The porous spacer initially underperformed compared to the pristine membrane but showed better flux retention over time, reaching 50% volume reduction in 14.07 h vs. 15.55 h for P. In contrast, A2 significantly outperformed both, reaching 50% volume reduction in just 5.32 h, 164% faster than A1 and 192% faster than P. This improvement is attributed to the porous spacer's ability to create favorable flow patterns and reduce fouling, as seen in similar studies. Yeast rejection was high across all membranes. P and A2 achieved >99% rejection, while A1 showed a slight drop to 95.9%, likely due to structural damage. Post-filtration inspection revealed a tear between A1’s rigid spacer and the membrane, caused by high shear stress during crossflow. A2, with its sponge-like, flexible structure, remained intact, deforming along with the membrane and avoiding delamination. The porous structure of A2 not only improved filtration rate and fouling resistance but also maintained strong rejection, highlighting the benefits of using PIPS-based VPP printing for integrated porous spacers.

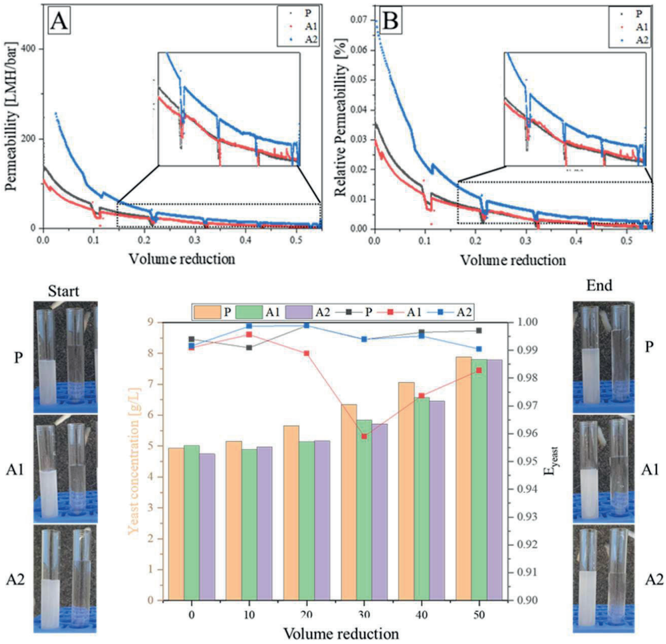

Figure 2-31, A: graph of actual permeability of a 5g/L yeast feed solution over volume reduction for P (gray), A1 (red) and A2 (blue). B: Relative permeability over volume reduction for P (gray), A1(red) and A2 (blue). Bottom: depicts, yeast retentate concentration (yellow axis) and membrane yeast rejection (grey axis) of the different membranes as well as before and after pictures at the filtration start and end [Paper(III)].

Fouling was visibly present on all membranes, forming a brown cake layer, as seen in Figure 2-32. On the pristine membrane (P), fouling was uniformly distributed, while membranes with arrow-shaped spacers (A1 and A2) showed patterned fouling concentrated along flow paths redirected by the arrow tips. These patterns matched CFD simulations, where high-velocity zones between arrows experienced less fouling due to increased turbulence, consistent with findings by Park et al. and Ibrahim et al [249,250]. CFD "red zones" (high flow) aligned with clean regions on the membranes, while fouling was concentrated in low-velocity "dead zones." Notably, the tops of the printed spacers especially the porous A2 design remained relatively clean, helping preserve active membrane area and contributing to A2's superior flux stability.

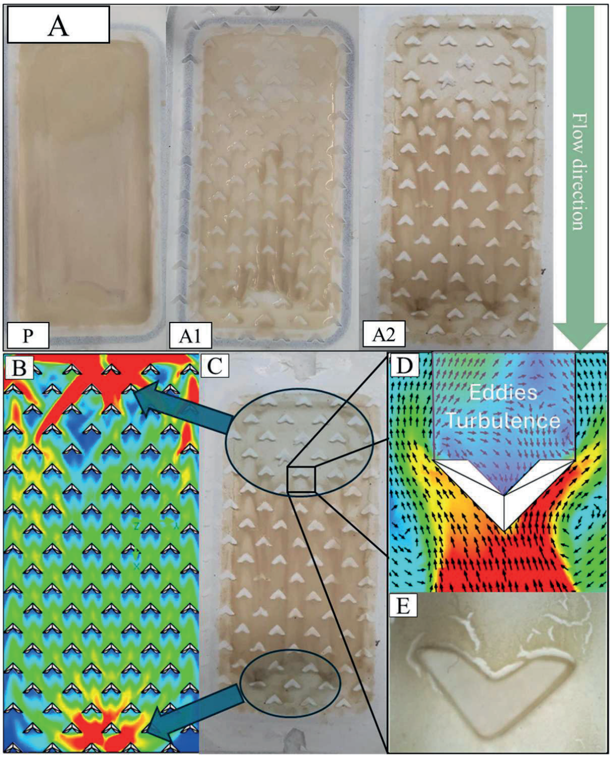

Figure 2-32. A: pictures of fouling layer on P, A1 and A2 membranes after 5g/L yeast filtration. B, C, D and E: depicts comparisons between A2 membrane fouling patterns and CFD simulations [Paper(III)].

2.5.5 Porous spacers printed for MD/MCr

Therefore, generating integrated spacers via VPP-PIPS has shown to be a viable method to improve membrane performance, not only by flow pattern but also due to the porosity in the printed spacers, the topography acts like a membrane itself, opening for mitigation of spacer touch points. The control of the flow pattern demonstrated here induced from this method could be beneficial in MD/MCr as it could help control concentration polarization and temperature polarization, which are important for the crystallization process. Furthermore, the control of porosity, material hydrophilicity/hydrophobicity and microscopic detail which has in this thesis been proven for VPP-PIPS, the porous spacers made via this method could act as crystallization promoters due to the change in porosity and material, this could offer favorable terms for crystallization as explained in section (1.4.3). Following the same method as in previous sections, changing the membrane for a Pall 0.2µm PTFE membrane and changing the VPP-PIPS ink to be tBA based to induce hydrophobicity the membranes with different topographies could be achieved. These membranes were further dried at 100°C to the final product seen in Figure 2-33. These membranes are ready to test in MD/MCr. These experiments have yet to be finished and are highly relevant for future studies.

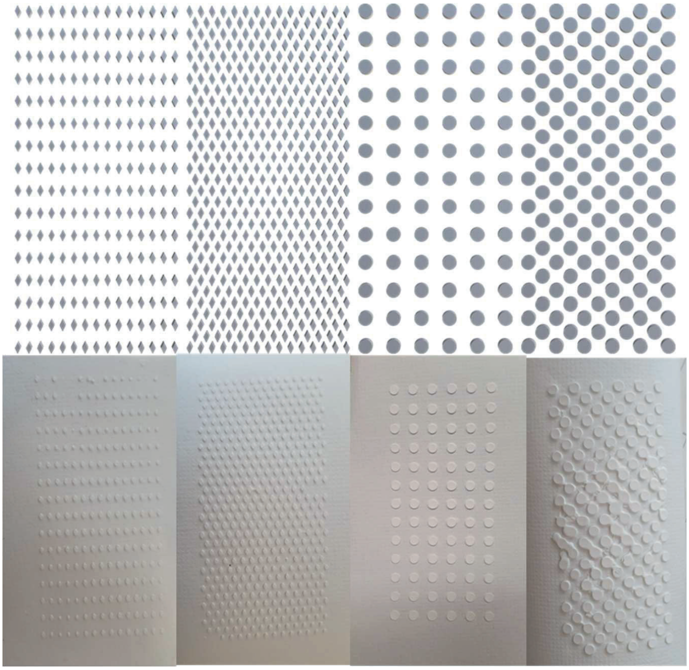

Figure 2-33. Top: CAD of membrane topography. Bottom:Pictures of different hydrophobic (ink three) VPP-PIPS printed topologies on 0.2µm Pall PTFE membrane with different patterns [A2].

2.5.6 Summary

To address some of the limitations associated with fully 3D-printing membranes via VPP–PIPS, this section explores an alternative approach in which membrane topographies are printed directly onto pre-existing membranes without significantly altering their intrinsic properties. This method proved effective in modifying flow patterns across the membrane surface and substantially mitigating fouling-induced flux decline, thereby increasing productivity in a microfiltration system. Additionally, the technique was successfully applied to hydrophobic MD membranes, which were dried using the hydrophobic ink described in Sections 2.3 and 2.4. The precise control over membrane properties, resolution, and physicochemical characteristics afforded by VPP–PIPS could have a significant impact on crystallization dynamics and ultimately improve brine management.

2.6. Summary and Perspectives of AM for membranes and MD/MCr

Producing membranes directly via AM is impractical due to the current scale/resolution tradeoff and therefore porous printing seems like a good alternative to achieve some of the benefits offered by the geometric control offered by AM methods. It was here proven that a new AM method for producing MD/MCr membranes with complex geometry suitable for processing brine to crystallization point for ZLD and brine mining was possible. This method utilizes the AM method with the highest processing resolution VPP and a phase inversion method not commonly used for conventional membrane production PIPS. This method VPP-PIPS has here been proven to have many beneficial qualities for membranes on top of the printing resolution, qualities such as high chemical stability, thermal stability and physicochemical tuning via copolymerization. Furthermore, promising results as a spacer for membrane cell perfusion was also demonstrated advancing the VPP-PIPS method beyond desalination membrane technology and into next gen of incorporated spacers for improved flux and anti-fouling.

Limitations and future

Though this is a step towards next geneneration membranes for membrane processes including MCr membranes for ZLD and brine mining, some obstacles and questions remain. The clear obstacle is the fragility of the membrane manufacturing methods, the membranes need extreme care and are prone to fracture and brakeage. Copolymerization seems to be a possible solution to this but needs further research. Another solution could be printing directly on other preexisting membranes which is both a less fragile method but also more scalable. Furthermore, questions still remain if this method even can mitigate the 3 overall problems explained in section (1.7.):

- Scaling/fouling mitigation
- Selectivity in multi-solute systems
- Recoverability of produced crystals

Therefore VPP-PIPS offers a lot of benefits, but it needs further research if it is to be a viable solution for ZLD and brine mining.

Chapter 3. Percrystallization

The development of next-generation MCr membranes using additive manufacturing was explored in Chapter 2. While these membranes show considerable promise, further research is required to address the remaining challenges facing MCr. Improving membrane performance is one strategy for advancing ZLD and brine mining technologies. An alternative approach focuses on the MCr process itself. Among emerging methods, percrystallization has shown potential. This chapter will examine percrystallization as a novel ZLD brine mining technique.

3.1. Percrystallization principles (Permeation, Evaporation, Crystallization)

The term *percrystallization* was first introduced in 1917 by Philip Adolph Kober [151], who defined it as the point at which saturation and crystallization occur on the exterior surface of a membrane as a result of pervaporation. The name itself is a portmanteau of *pervaporation–crystallization*, with *pervaporation* combining *permeation* and *evaporation* [251]. In essence, percrystallization describes a process in which a liquid permeates a semipermeable barrier (typically a membrane), evaporates on the permeate side, and concentrates any solutes to the point of crystallization. While the principle is longstanding, similar to mechanisms employed in evaporative coolers, such as the Spanish *botijo*, where water permeates and evaporates through porous clay walls, leaving salt crystals behind [252], percrystallization specifically refers to this process when applied with synthetic membranes. Other natural and engineered analogues include efflorescence in porous building materials like concrete and wood [253] and salt excretion in mangrove trees, where residual salts are deposited on leaves through evaporative processes [254,255]. Although the concept is over a century old, percrystallization has only recently gained attention as a ZLD desalination strategy. Motuzas et al. [256] were the first since Kober to demonstrate percrystallization experimentally in 2018. Since then, relatively few studies have been published, with most contributions originating from the same research groups [256–258]. As a result, development in this field remains limited.

Understanding percrystallization requires familiarity with its mass transport mechanisms, which are analogous to those in pervaporation and are typically described as a two-step process: (1) transport through the membrane and (2) evaporation. The first step can here be characterized by liquid flow through porous media, commonly described by Darcy's law (Equation (3-1)), while the second is governed by evaporation kinetics (Equation (3-2)) [259,260].

Darcy Flow: $$J_{darcy} = \frac{k}{\mu * L} * \Delta P_h \tag{3-1}$$

Evaporation: $$J_e = B_{vap}(\Delta P_{vap}) \tag{3-2}$$

J_{darcy}, k, μ, L and ΔP_h is the liquid flux, permeability coefficient, dynamic viscosity, membrane thickness and hydraulic pressure difference between feed and permeate. For the evaporative part J_e, B and ΔP_{vap} is the vapor flux, vapor permeability coefficient and the vapor pressure difference between the liquid film and the permeate. Evaporation is arguably the most important mass transport, as it needs to be equal or greater than the liquid flow through the membrane in order to avoid the system flooding, but enough to supply the evaporation process.

$$J_e \geq J_{darcy} \tag{3-3}$$

To optimize percrystallization performance, Darcy flow through the membrane must be controlled. One approach is to eliminate hydraulic pressure gradients across the system. If this is not feasible, membrane characteristics can be modified, for example, by increasing the membrane thickness (L) to raise resistance or reducing permeability (k), which depends on properties such as pore size, porosity, and geometry, as described by the Hagen–Poiseuille and Kozeny–Carman equations [261,262].

The evaporative flux (J_e) can also be increased by raising the temperature at the membrane surface to enhance vapor pressure or by reducing permeate-side pressure through vacuum application. This likely explains why most percrystallization studies have employed vacuum operation to achieve higher fluxes, typically in the range of 9.43–33 LMH [256–258,260,263]. However, it is important to note that applying vacuum also induces transmembrane flow and increases the hydraulic pressure difference (ΔP_h), thereby raising the risk of membrane flooding, a major problem seen in percrystallization. Solute transport through the membrane during percrystallization is assumed to resemble the diffusion-dominated transport observed in other membrane processes. This diffusion can be described by Fick's law (Equation (3-4)) [264].

Solute transport:
$$J_{solute} = \frac{K_s * D}{L} * \Delta c \tag{3-4}$$

Here J_{solute}, K_s, D and Δc are the solute flux, a sorption constant, diffusion constant and the concentration difference between the feed and permeate membrane interphase respectively. Since evaporation occurs at the permeate side of the membrane, this will lead to a higher concentration and therefore a solute transport direction from permeate to retentate, similare to the reverse solute flux observed in FO [265]. This means there is also a conncetion between evaporation intensity and the crystallization occuring. Too low will lead to solutes migrating back to the feed. Since percrystallization is able to use size exclusion membranes, an advantage which percrystallization has over conventional MCr. An expression for the rejection of specific solutes is commonly utillized here. This is usually expressed via a rejection coefficient (R), and is expressed as Equation (3-5). However since the permeate is further evaporated from the side of the permeate, an R of the solutes permeating the membrane can be expressed as in Equation (3-6) based on the change in feed concentration.

$$R = 1 - \left(\frac{c_p}{c_f}\right) \tag{3-5}$$

$$R = 1 - \left(\frac{c_{f(i)} * V_{f(i)} - c_{f(t)} * V_{f(t)}}{c_{f(i)} * V_{f(i)}}\right) \tag{3-6}$$

c_p is the permeate concentration c_f, and V_f is the concentration and volume on the feed respectively. (i) and (t) subscripts decribe initial value or value at time t respectively. If *R* is 1, means the rejection of a specific solute is 100% and no solutes pass into the permeate side, if it is 0 rejection is 0% and the solute passes unhindered to the permeate side. It also needs to be stated that there is a difference between solute rejection of the membrane and the total system. The membrane itself may have little rejection and solutes passes to the permeate side of the membrane, due to only vapors leaving the permeate side the final produced water can still be solute free though *R* of the membrane is low.

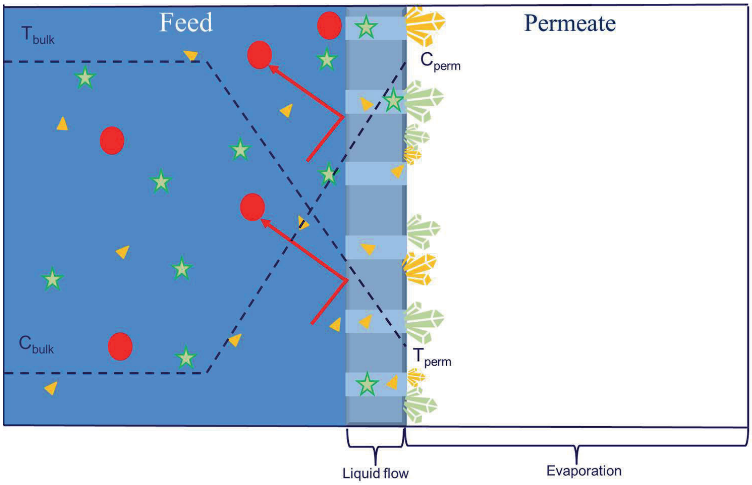

Figure 3-1, illustration of percrystallization with flow through the membrane, and selective rejection of red solute.

Although percrystallization is a thermal evaporative process, it differs fundamentally from MD in that membrane permeation occurs in liquid form rather than as vapor. This distinction introduces several advantages over MD which can largely be summarized as:

- **Membrane Material:** Because liquid permeation drives the process, membranes do not need to be hydrophobic, enabling the use of a wider range of materials.

- **Wetting Mitigation:** Unlike MD, where hydrophobicity is essential, percrystallization requires wetting, making it inherently more robust to wetting compounds such as surfactants.

- **Membrane Selectivity:** In addition to vapor-phase selectivity, the membrane itself provides active transport selectivity, potentially influencing which volatiles and ions are transferred and crystallized.

- **Crystal Collectability:** Percrystallization produces dry crystals on the permeate side, facilitating easier collection compared to MD-based MCr.

However, several disadvantages exist in percrystallization relative to MD/MCr:

- **Flooding:** Flow through the membrane must be precisely controlled to prevent leakage, as there is no liquid entry pressure threshold like in MD.

- **Limited Tuneability:** Increasing temperature or vacuum to boost flux can also increase flooding risk, complicating operational adjustments.

These are some of the main advantages and drawbacks compared to MD, but given how nascent the field is, further research may reveal additional considerations.

3.2.1 Future of percrystallization

Percrystallization appears to be a promising new method for ZLD and brine mining, combining desalination with continuous crystal recovery. It has demonstrated versatility across a range of solutes, from NaCl to pharmaceuticals like paracetamol, suggesting strong potential as a next-generation MCr technique. However, because the field has only recently been revisited, important questions remain [256–258,260,263]:

- **Robustness:** While percrystallization could be more resistant to fouling and wetting than conventional MD, its performance with real-world brines remains underreported.
- **Available materials:** While percrystallization has been proven, almost exclusively done on hydrophobic modified tubular membranes. However, in theory percrystallization should function on any membrane where the conditions of higher evaporation vs liquid flow is met.
- **Retentate Composition:** Although often described as a ZLD process, the composition of the retentate after treatment has not been thoroughly characterized.
- **Selectivity:** The potential for membrane-based selectivity in crystallization has been largely unexplored.

3.2. Our Percrystallization method

The percrystallization system developed in this thesis used a 3D-printed module (Figure 3-2) measuring 10 × 8 × 1 cm to accommodate flat-sheet membranes. The internal frame (6 × 4 cm) provided an active area of 48 cm^2 and an internal volume of 24 cm^3. To prevent leakage, 1 mm silicone gaskets were placed on each side of the membrane.

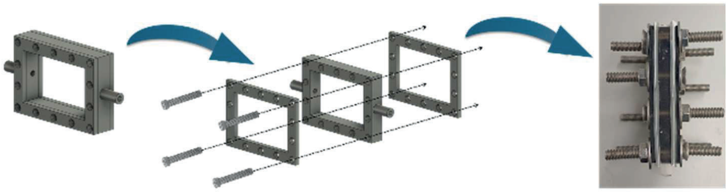

Figure 3-2, schematic of fully 3D printed percrystallization module, fully assembled – disassembled and picture of module with membrane respectively.

The percrystallization system consists of three main subsystems: a feed system, a permeate gas system, and a condensation system. The feed circuit employed a peristaltic pump to deliver the feed solution through a heater, into the membrane module, and back into the feed reservoir. The permeate side utilized a sweeping gas, either compressed air (CA) or CO_2, with flow regulated by a flowmeter. The sweeping gas was then directed into a condensation tube submerged in a chilled liquid bath, cooled by a recirculating water loop driven by a peristaltic pump and a water chiller. A schematic of the non-vacuum-assisted percrystallization setup is shown in Figure 3-3.

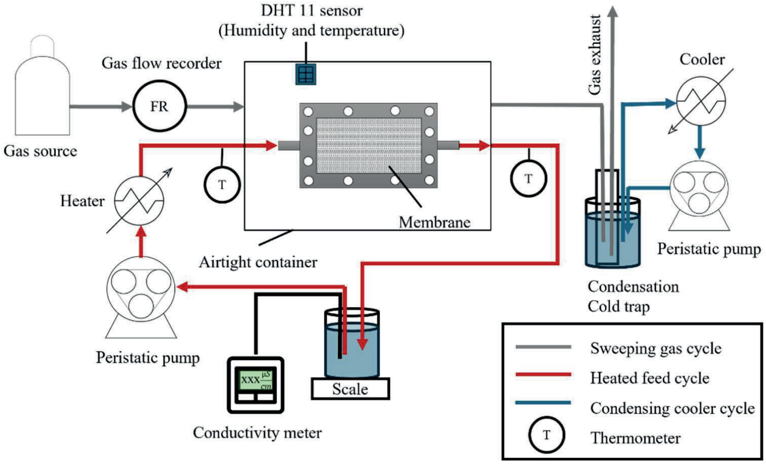

Figure 3-3, Illustration of percrystallization using sweeping gas. Sensors pumps and other unit operations are depicted as well as the three cycles, sweeping gas(grey), feed(red) and cooling(blue).

3.3. Percrystallization for Seawater desalination

As previously described, percrystallization has demonstrated strong potential as a desalination method capable of simultaneously producing highly pure water and recoverable crystalline solids, thus achieving ZLD. However, prior studies have predominantly focused on synthetic brines. In this section, percrystallization was applied to treat natural seawater for ZLD and mineral recovery, building on the work presented in Papers (IV and V).

3.3.1 Materials and methods

The experiments were conducted in the setup as explained in section 3.2. As the permeation rate is strongly influenced by membrane structure, two commercial Alfa Laval membranes, one ultrafiltration (UF) and one nanofiltration (NF), were evaluated to assess the impact of pore size and porosity. Membranes with smaller pores, such as microfiltration (MF) membranes, were excluded to avoid flooding during operation. The specifications of the membranes can be found in Table 3-1.

Table 3-1, Alfa Laval membranes used in these studies and their specifications [Paper IV]

	NF99HF	**ETNA01PP**
Support	Polyester	Polypropylene
Selective layer	Composite	Fluro polymer
Rejection (pore size)	99% $MgSO_4$ (≈0.1203kDa)	1000 kDa

The phase composition of the crystals produced in the various experiements were determined using X-ray diffraction (Empyrean, Malvern PANalytical). Atomic Absorption Spectroscopy (PerkinElmer, PinAAcle 900F) was done for quantification of ions present in seawater and crystals, such as sodium (Na), calcium (Ca), magnesium (Mg), and lithium (Li). The crystal size and morphology were investigated with an electron microscope (FEI QEMSCAN 650F). The seawater used was collected from Hanstholm Harbor on the North Sea coast of Denmark. Its measured properties included a conductivity of 56.2 ± 0.2 mS/cm, water activity of 0.983 ± 0.00, and pH of 7.78. The dry matter content was 3.25 wt%, comprising 2.78 wt% inorganic and 0.47 wt% organic matter. The ionic composition of the predominant cations, Na, Mg, Ca, and trace amounts of valuable Li is presented in Table 3-2 and aligns with typical seawater compositions [266].

Table 3-2, Na, Ca, Mg and Li composition of the seawater from Hanstholm harbor, coast of Denmark at the North sea.

Water from Hanstholm Havn			
Na[mg/L]	Ca[mg/L]	Mg[mg/L]	Li[mg/L]
10320±110	370.26±0.74	1290±10	0.12±0.1

3.3.2 Percrystallization characterization

Percrystallization remains underreported, particularly in non-vacuum configurations, and involves complex mass transport governed by both liquid permeation and evaporation. Therefore, a series of thermal experiments were conducted to characterize performance. Limited knowledge is developed on the membrane properties and feed conditions in regards to the end water flux. Therefore, to show the effects of temperature and membrane type on the water flux in this proposed system, tests were carried out with deionized water at feed temperatures of 60 °C, 70 °C, and 80 °C. Due to the low system flow rate (10 L/h), actual membrane inlet temperatures were lower than target setpoints: 43.78 °C ± 0.28, 52.32 °C ± 0.23, and 58.6 °C ± 0.27 for the NF membrane, and 45.38 °C ± 0.32, 51.53 °C ± 0.88, and 58.91 °C ± 1.08 for the UF membrane. As shown in Figure 3-4, the more porous UF membrane exhibited higher flux compared to the NF membrane. Specifically, UF achieved water fluxes of 3.73 ± 0.32 LMH, 5.12 ± 0.88 LMH, and 7.38 ± 1.08 LMH at the three respective temperatures, while NF fluxes were 0.73 ± 0.28 LMH, 1.30 ± 0.23 LMH, and 3.25 ± 0.27 LMH. This is related to the high liquid flow through UF membranes compared to NF, opening for higher amounts of evaporation. Similar trend between porosity and evaporation have been reported on porous solar evaporators Yan et al, who saw an increase 0.76LMH to 1.10LMH by increasing porosity from 0.8 to 0.9 respectively [267].

Despite the use of hydrophilic membranes and the absence of vacuum assistance, relatively high fluxes were obtained. Notably, the performance compares favorably to DCMD systems such as that reported by Aamer et al. [268], who observed 3.86 LMH at a 56 °C feed and 15 °C permeate. In this study, UF membranes consistently outperformed NF membranes, demonstrating higher promise even at modest temperatures. For comparison, other studies using similar non-vacuum percrystallization methods have reported fluxes of 2.1 LMH and as low as 0.02 LMH [269,270]. Flux increased with feed temperature for both membranes, consistent with the rise in vapor pressure characteristic of thermal-driven processes like MD. Using the vapor pressure difference between feed and permeate (sweeping gas), the permeability coefficient (B) was calculated as 17.07 ± 4.85 LMH/bar for NF and 58.38 ± 2.09 LMH/bar for UF. The nearly constant permeabillity (B) indicates that evaporation can be reliably predicted as a function of temperature, similar to MD.

This contrasts with findings by Nielsen et al. [263], who observed no overall increase in vaporization with higher feed temperature, likely due to the complications introduced by vacuum operation in their setup. Their reported permeabillity (4.67–18.13 LMH/bar) are comparable to the NF results here, while the UF membranes in this study exhibited substantially higher permeability.

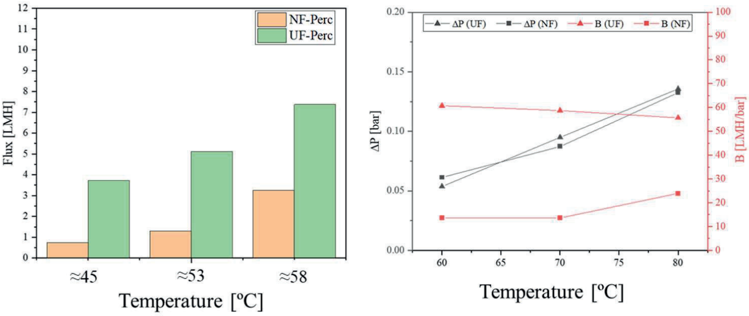

Figure 3-4. Left: Bar graph of pure water flux for a UF (green) and NF (orange) membrane at different inlet temperatures. Right: The Vapor pressure(black) and overall permeability(red) of the UF and NF membrane. [Paper (V)]

Therefore, it was confirmed that membrane properties and temperature had a positive correlation with water flux as well as the reported vacuum in vacuum driven percrystallization systems. This confirms the versatility of the percrystallization method and the competitiveness compared to conventional MD systems.

3.3.3 Preliminary seawater testing

To evaluate the suitability of percrystallization for ZLD, experiments were conducted as described in Section 3.2. The setup employed a commercial Alfa Laval NF99HF membrane with the heater set to 80 °C, yielding an actual feed temperature of 61.8 ± 2.8 °C.

Using compressed air at 10 L/min, the system operated continuously for 18.5 hours, achieving a 52.2% volume reduction. An average flux of 3.19 ± 0.05 LMH was recorded. Initial flux peaked near 15 LMH during system stabilization but remained relatively steady thereafter. The membrane module exhibited a temperature drop of 12.2 ± 3.2 °C, consistent with convective and evaporative losses typical of MD. Although air humidity declined slightly, it did not significantly impact flux. Crystallization began on the membrane surface after ~2 hours, initially as isolated nucleation sites that gradually expanded. Visual changes plateaued after 9 hours, suggesting most crystal growth occurred early. Unlike conventional MD, membrane scaling did not reduce performance, likely because percrystallization does not rely on dry hydrophobic surfaces [271]. Analysis of the retentate showed increased dry matter (5.67 wt%), conductivity (81.7 ± 0.64 mS/cm), and water activity (0.967 ± 0.13). This increase suggests some back diffusion or membrane selectivity, though this mechanism has not been thoroughly examined in prior studies. Overall, this preliminary experiment demonstrates that percrystallization is a promising thermal desalination technique capable of achieving high salinity and significant volume reduction while producing dry crystals on the permeate side.

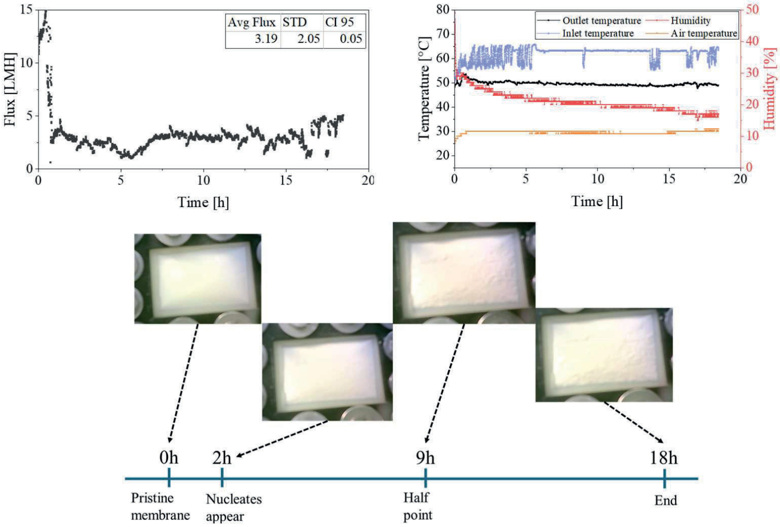

Figure 3-5. Top left: Water flux of NF99HF membrane in percrystallization mode using seawater. Top right: Temperature and humidity of input and outlet streams in the percrystallization experiment. Bottom picture: Pictures of permeate side of the membrane in chronological order. [Paper (IV)]

3.3.4 Membrane selection

As previously observed, switching to a UF membrane improved water flux performance, and similar results were obtained during seawater desalination. The UF membrane achieved an average flux of 4.91 ± 0.03 LMH (Figure 3-6). Despite a lower inlet feed temperature (57.4 ± 1.3 °C for UF vs. 61.8 ± 2.8 °C for NF), the UF membrane delivered 1.72 LMH higher flux.

This improved flux performance likely results from differences in membrane properties (pore size, porosity), where the UF has a more porous structure than the NF allowing more uninhibited flow through the membrane as discussed earlier. Differences in material and surface properties further influenced crystallization behaviour. As shown in Figure 3-6, both membranes developed crystals, but with distinct deposition patterns. On UF, crystallization was more localized, likely due to hydrophobicity, resulting in nucleation only at wetting points. These regions appeared as dark spots, suggesting localized pore wetting. In contrast, the hydrophilic NF membrane showed more uniform crystal distribution, consistent with full wetting and even salt migration across the surface.

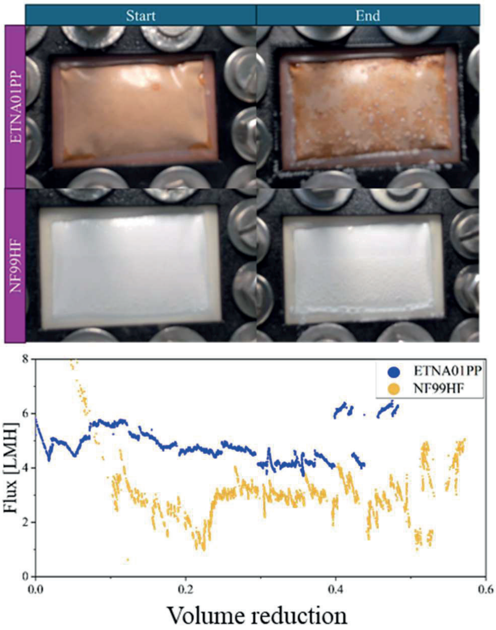

Figure 3-6, desalination of seawater with UF membrane ETNA01PP and NF membrane NF99HF. Top picture depicts membrane surface on the permeate side at the beginning and end of the run. [Paper(IV)]

3.3.5 Sweeping gas flow and composition

Percrystallization relies on feed evaporation, and here requiring dry ambient sweeping gas to sustain vapor transport. To evaluate the impact of gasflow, compressed air was supplied at 5L/min, 10L/min, and 15L/min. All conditions reduced seawater volume, yielding fluxes of 2.69 LMH ± 0.02 LMH, 3.19 LMH ± 0.05 LMH, and 2.71 LMH ± 0.06 LMH, respectively (Figure 3-7). Dry matter flux decreased with higher airflow: 28.89 $g/m^2 \cdot h$, 17.80 $g/m^2 \cdot h$, and 16.62 $g/m^2 \cdot h$ for 5 L/min, 10 L/min, and 15 L/min, paralleling the water flux trend and suggesting reduced dry matter permeability.

No clear trend in water flux emerged despite progressively lower humidity levels (40.5%, 20.9%, 16.9%), suggesting that in these experiments the sweeping gas flowrate wasn't the limiting factor. This explaination is reflected by Basini et al. who found an positive flux increase in SGMD with flowrate at low flowrates while at high flowrates membrane resistance becomes the limiting step [272]. Beyond facilitating evaporation, sweeping gas composition may influence interfacial reactions. Literature suggests that the pressence of CO_2 can promote carbonate precipitation with cations such as Li^+, Mg^{2+}, and Ca^{2+} [273], offering potential for increased selective crystallization. To test the effects of CO_2 as sweeping gas, 99.9% CO_2 was introduced at 5L/min, 10L/min, and 15L/min. As with compressed air, no consistent trend was observed in flux with increasing CO_2 flow. Water fluxes were 4.12LMH ± 0.02LMH, 6.76LMH ± 0.20LMH, and 4.38LMH ± 0.03LMH, while dry matter fluxes reached 81.27g/m²·h, 60.74g/m²·h, and 82.73 g/m²·h, respectively (Figure 3-7). Notably, both water and dry matter fluxes were significantly higher than with compressed air, with dry matter flux more than doubling. Despite higher humidity under CO_2, evaporation increased, suggesting CO_2 may enhance water transport by mechanisms not yet fully understood.

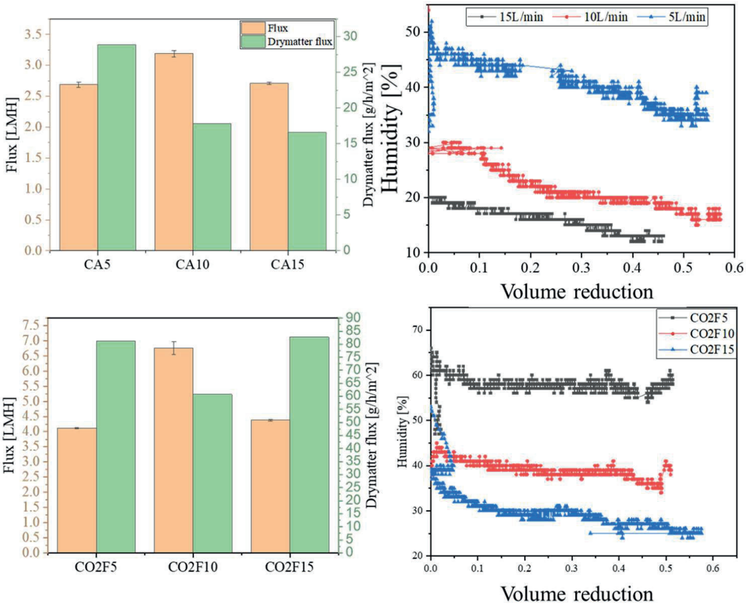

Figure 3-7, Top graphs are of water flux (orange) and drymatter flux (green) at different compressed air used as sweeping gas at different flows. Top Right: humidity (percentage water vapor pressure compared to saturation) of the sweeping gas at different compressed air flows. Bottom graphs depicts similar but for CO_2 gas as sweeping gas. [Paper(IV)]

Crystals obtained from various experiments, with different sweeping gas gas flowrates and gas compostions were analyzed by XRD (Figure 3-8) to determine the crystal composition. Distinct peaks at 27.56°, 31.91°, 45.65°, 56.67°, 75.45°, and 84.19° 2θ were characteristic of NaCl, confirming that sodium chloride was the predominant phase formed. When CO_2 was used as the sweeping gas (Figure 3-8), additional peaks emerged, notably at 14.5° and 29.6° 2θ, corresponding to $CaCO_3$. This indicates that CO_2 promotes calcium carbonate precipitation, supporting the potential for enhanced selective crystallization at the membrane interface of carbonates. However, the $CaCO_3$ peaks remained significantly less intense than those of NaCl, suggesting that selectivity via CO_2 alone remains limited. Some $CaCO_3$ peaks were also observed under compressed air, although they were less pronounced, implying that CO_2 is not essential for carbonate formation but substantially improves its precipitation. Overall, these findings suggest that the process can operate with both ambient air and CO_2-enriched industrial gas streams, with CO_2 providing improved mineralization performance. Though XRD results, showed a difference in the composition of the crystals produced, elemental analysis of the retentate water showed little difference in regars to compostion between when CO_2 and CA was used as sweeping gasses. However, considereing the rejection coefficient of the different solutes of the membrane, there was a trend that when CO_2 was utillized higher degree of solute migration and subsequent crystal formation was observed (Figure 3-8). This could be due to the higher evaporation rate, which would lead to higher concentrations at the permeate and subsequently less time for the solutes to diffuse back to the retentate. Furthermore, the increased availability of CO_2 could initiate precipitation of carbonates which has a lower solubillity compared to other precipitate types. Nevertheless, a difference in rejection of the solutes were observed.

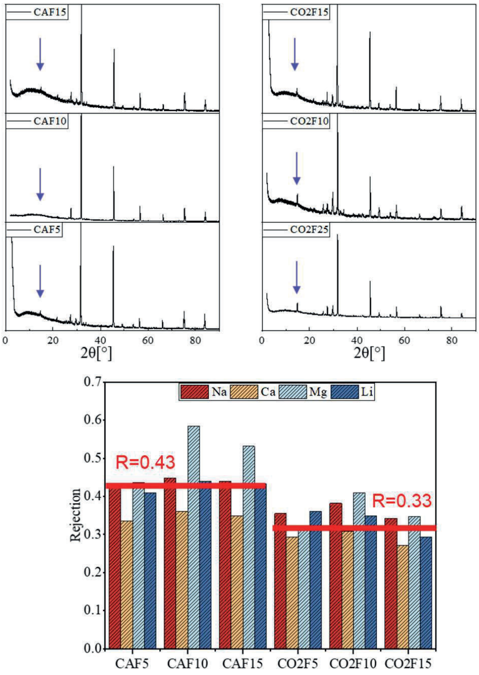

Figure 3-8: Top: XRD graphs of the produced crystals from the percrystallization experiments at different Compressed air flow (CA stands for compressed air and Fxx is for flow in L/min) and different CO_2 gas flows. Clear Carbonate peaks occur more prominently when CO_2 is utilized (arrows at prominent $CaCO_3$ 14.5° peak). Bottom: Bar graph of membrane rejection of the components Mg, Ca, Mg and Li at the different sweeping gas compositions and flows [Paper(IV)].

3.3.6 Full continuous ZLD seawater desalination system with mineral recovery

A key metric for desalination success is not only achieving ZLD but maintaining stable long-term operation. For example, RO desalination of seawater typically requires extensive pretreatment to prevent membrane damage, fouling, and scaling [274,275], increasing process complexity and reducing system lifetime. To evaluate percrystallization's suitability as a simpler high-salinity desalination approach, a prolonged experiment was conducted using an NF membrane. The feed seawater was heated to 59.67 ± 1.85 °C with a pump flow rate of 10 L/h. A semi-batch protocol was followed: 500 mL of seawater was replenished each time the volume dropped to ~250 mL. This cycle was repeated six times, processing a total of 3 L down to 249 mL, achieving a volume reduction of 91.7%. The system operated continuously for 163 hours and was stopped only upon reaching the target volume, not due to failure, demonstrating potential for extended operation. As shown in Figure 3-9, water flux declined gradually from 4.50 LMH to 2.49 LMH, while conductivity increased from 56.2 mS/cm to 198.5 mS/cm. To evaluate the impact of scaling, crystals were manually removed from the membrane surface at 71.7 hours. Water flux remained unchanged afterward, indicating that crystal accumulation did not significantly affect performance. This robustness highlights percrystallization's suitability as a continuous ZLD process. This behavior contrasts with membrane distillation (MD), which typically experiences severe fouling under prolonged high-salinity operation, and reverse osmosis, which is limited to salinities below ~72,000 ppm [276–278]. Moreover, the collected permeate had high purity, with conductivity measured at 81.4 μS/cm, making it suitable for applications such as electrolysers or ultrapure water production [279,280]. Although crystal formation removed some ions, the rising conductivity suggests substantial back-diffusion of solutes throughout the deslination. Flux reduction was partly attributable to decreased water activity in the bulk feed (from 0.98 to 0.87), though localized concentration gradients on the permeate side likely further lowered water activity. Notably, performance did not show the typical abrupt declines associated with fouling, and the system continued to function effectively as salinity increased.

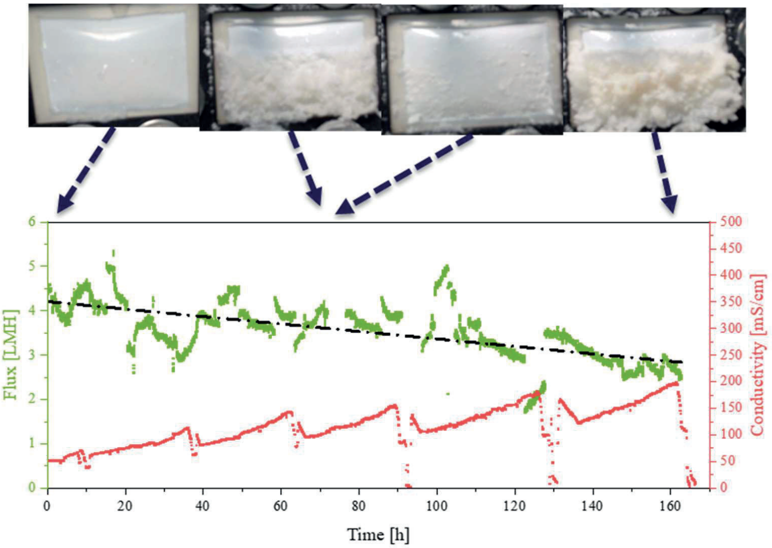

Figure 3-9, Plot of water flux (green) and feed conductivity (red) of an seawater desalination experiment with 5 cycles of refilling reaching 91.7% volume reduction. Pictures of permeate side of membrane at different time are depicted, at 71.8h both before and after crystal recovery is shown [Paper(IV)].

Solid flux was calculated for each cycle and is shown in Figure 3-10. Unlike the declining water flux, solid flux increased with recovery, reaching 36.15, 64.56, 101.27, 108.50, and 107.05 g/m²·h from Cycles 1 to 5, suggesting that crystallization accelerated with rising saturation and reached steady-state conditions by Cycle 3. From the composition of the permeate and retentate, it was seen that selectivity was not absolute and the crystals achieved were a mix of ions (Na^+, Ca^{2+}, Mg^{2+} etc). While complete ion separation was not achieved through membrane rejection alone, post-treatment options are available. For example, prior studies have demonstrated that stepwise pH adjustment with NaOH can selectively precipitate Mg and Ca from brines [281]. Similar results were obtained in this work: incremental pH increases in cycles adding 0.4g to 100ml in increments until precipitation would seize which would happen in the second cycle of addition. This led to a pH of ~9.38 and the precipitate was found to be (97.2%) Mg compounds. Continuing the cycles would lead to additional precipitate which was found to be (95.1%) Ca compounds and the precipitate would end around pH of ~12.30. Consequently, residual brine from percrystallization can be further valorized through targeted chemical precipitation.

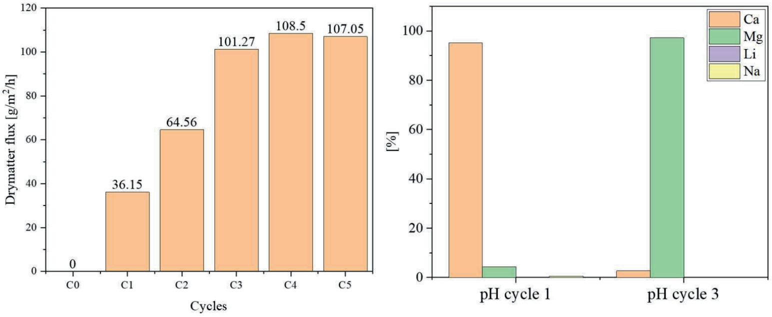

Figure 3-10, Left: Drymatter flux between each feed refilling cycle. Right: Relative weight percentage of Ca, Mg, Li and Na in the precipitating crystals at different pH treatment cycles [Paper(IV)].

3.3.7 Summary

The data demonstrate that this membrane crystallizer is a reliable and adaptable method for salt removal. Selectivity wasn't as high as would have been expected with the membranes, membrane selectivity improved by introducing CO_2 as sweeping gas via carbonate precipitation. In the 163-hour staged experiment, untreated seawater was processed at ~60 °C, conditions achievable using waste heat from solar, industrial, or geothermal sources [282–284]. Water flux declined gradually from ~4.50 LMH to ~2.49 LMH as salinity increased to 150 g/L, while dry matter flux rose from 36.15 $g/m^2 \cdot h$ to 107.08 $g/m^2 \cdot h$. The process produced highly desalinated water (conductivity ~81.4 µS/cm), which can be further refined to ultrapure water (<0.055 µS/cm) [285] for applications in green hydrogen production, semiconductor manufacturing, potable water, or beverages [286,287]. The precipitated crystals simultaneously enable CO_2 sequestration and the concentration of valuable elements such as lithium, which is important for battery manufacturing [288], though additional refining is required for extraction.

Following crystallization, the concentrated brine can be treated with NaOH to remove nearly all calcium and magnesium [289–291]. These byproducts have applications in concrete, food, pharmaceuticals, and carbon capture [292–294]. While this treatment step requires NaOH input, the sodium-rich retentate can be electrolyzed to regenerate NaOH and produce hydrogen gas [295]. The resulting dilute NaOH can be recycled or concentrated for reuse. Overall, this percrystallizer simultaneously produces purified water and solid mineral byproducts while demonstrating high stability and fouling resistance. Unlike conventional processes, it offers the potential for economically viable carbon capture with minimal performance degradation over extended operation. A conceptual diagram of a fully self-sufficient desalination and brine mining plant is shown in Figure 3-11.

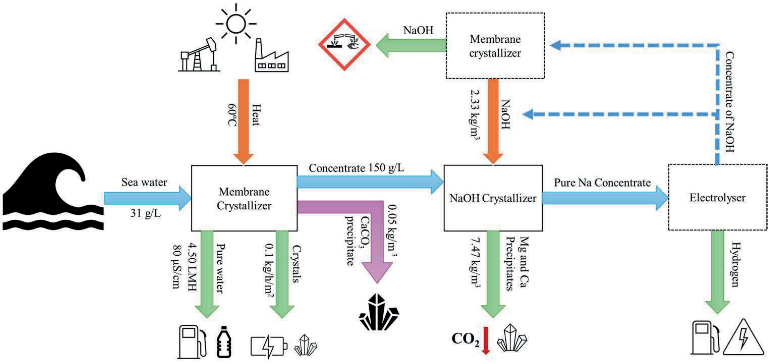

Figure 3-11: Process diagram illustrating seawater treatment, beginning with the percrystallization step in a crystallizer, followed by pH adjustment using NaOH. Process streams are shown in blue, direct outputs in green, indirect outputs in purple, and inputs in orange [Paper(IV)].

3.4. Percrystallization of industrial wastewater (anodizing industry)

Percrystallization was proven in the previous section (3.3) to be a robust and stable desalination method for seawater, capable of achieving high volume reductions without the typical challenges of RO and MD, such as high osmotic pressure and severe scaling or fouling. While seawater is relatively clean and primarily composed of NaCl, desalination applications extend well beyond this feed source. Madsen et al. [257], demonstrated vacuum-assisted percrystallization of $NiSO_4$ as a simulated industrial case for enhanced recovery and valorization of waste streams. However, simulated brines do not reflect the full complexity of real industrial wastewater. To advance the technology's readiness level, it is necessary to evaluate performance on actual waste streams. The anodizing industry is a significant sector, providing corrosion resistance, durability, and aesthetics to metal surfaces and supporting applications in aerospace, automotive, and construction [296–299]. Anodizing processes generate substantial wastewater containing toxic heavy metals that must be effectively removed [300]. Accordingly, to demonstrate the versatility of percrystallization, this section focuses on treating real anodizing wastewater, drawing primarily on data from Papers IV and V. The wastewater was supplied by Danish Anodizing Industry Ltd. (DAI) in Thisted, Denmark.

3.4.1 Materials and methods

The specific composition of the wastewater from DAI or rather their reject "color water" used in this section is presented in Table 3-3.

Table 3-3, Composition of spent anodized color water from DAI (Olsen et Al. [301])

Color bath	Measurement	Std
pH	5.7	N/a
Conductivity [µS/cm]	$7.64*10^3$	N/a
Water activity	0.9928	0.0021
Dry matter [%]	98.93	0.00
Organic fraction [%]	0.50	0.01
Inorganic fraction [%]	0.56	0.02
Cd [µg/L]	31.67	±2.51
Cr [µg/L]	$145.12*10^3$	$\pm1.81*10^3$
Cu [µg/L]	1650.0	±59.99
Ni [µg/L]	1179	±9.84
Pb [µg/L]	347.0	±62.81
Zn [µg/L]	354.7	±4.61

The percrystallization experiments were conducted in the setup as explained in section 3.2. Furthermore to compare percrystallization performance against other methods (pressure driven, DMCD), the same membranes used here in percrystallization ETNA01PP (UF) and NF99HF (NF), were also used in a dead-end pressure filtration setup. To further compare to DCMD, data from Olsen et al. [301] was used which utillizes polypropylene hollow fiber membranes to treat the same color wastewater from DAI. The phase composition of the crystals produced in the various experiements were determined using X-ray diffraction (Empyrean, Malvern PANalytical). Atomic Absorption Spectroscopy (PerkinElmer, PinAAcle 900F) was done for quantification of heavy metal ions present in DAI waste water and crystals produced, such as Copper (Cu) and Chromium (Cr). A relative concentration of the color compound was analysed spectrophotometrically(Helios Epsilon, ThemoSpectroscopy).

3.4.2 Wastewater treatment

Section 3.3 demonstrated that both NF and UF membranes can desalinate seawater, with UF providing higher flux but lower solute rejection. Building on this, we evaluated both membrane types for anodizing wastewater desalination. Anodizing involves acid rinsing (~40 °C), anodizing (~70 °C), and coating (>95 °C) [302–304], generating effluent that often exceeds the 45 °C discharge limit [305,306]. To mimic waste-heat recovery in a circular economy, experiments were conducted at ~60 °C, with measured inlet temperatures of 55.67 ± 3.97 °C (UF) and 56.29 ± 1.37 °C (NF). Runs were performed at 10 L/h and terminated at 90% volume reduction.

As shown in Figure 3-12, UF consistently yielded higher flux than NF, decreasing from ~5 to ~2 LMH versus NF's decline from ~2 to <0.5 LMH. Flux reduction can be attributed to lowered water activity at high solute concentrations and fouling from deposition of feed solutes on the membrane. Condensate conductivities remained <100 µS/cm, indicating high-purity produced with a quality higher than that of potable water (<1500 µS/cm). Visual inspection revealed blue compounds accumulating on NF membranes, forming oily agglomerates, suggesting partial rejection of colorants. Since the permeated fraction formed a removable oily residue, zero-liquid discharge (ZLD) remained feasible.

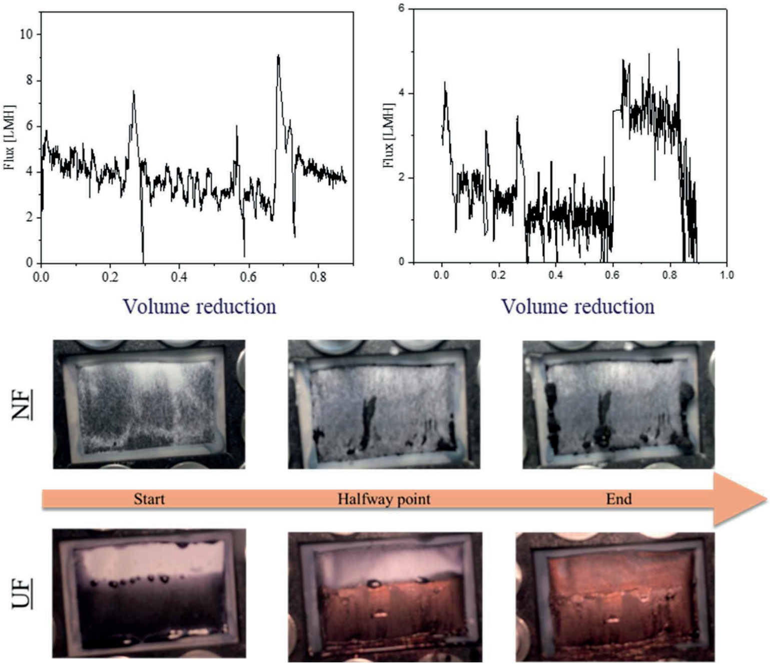

Figure 3-12. Water flux Percrystallization of color water from anodized wastewater industry using either an UF or NF membrane. Bottom pictures are permeate side of the membranes in chronological order from start to midway to end experiment. [Paper(V)].

For comparison, the same anodizing wastewater was treated with NF and UF membranes in pressure-driven mode, as well as by DCMD (from Olsen et al. [301]), all operated to ~90% volume reduction. Pressure-driven filtration was conducted in a stirred cell (600 RPM), while DCMD employed hydrophobic polypropylene hollow fibers (Membrana Accurel® PP S6/2) at 20.78 L/h, with feed and permeate temperatures of 77.4 ± 0.3 °C and 21.8 ± 2.1 °C, respectively. As shown in Figure 3-12, DCMD maintained a stable flux of 3.13 ± 0.47 LMH, comparable to percrystallization but lower despite operating >10 °C hotter. Unlike percrystallization, DCMD exhibited sudden flux increase and color breakthrough at ~90% water recovery, confirmed by a rise in permeate conductivity (142 → 166 µS/cm), at which point cleat blue tint was observed in the permeate, indicating membrane wetting and a practical recovery limit. This highlights percrystallization as more stable at high recovery, achieving higher flux at lower temperatures, though with greater sensitivity to concentration-driven flux decline. Pressure-driven membranes showed more severe performance losses. UF began at 31.61 LMH/bar (17.9% below pure water) and declined steadily to 14.07 LMH/bar at 90.6% recovery, a 63.4% loss. NF retained solutes more effectively but suffered sharper decline, from 4.12 to 0.51 LMH/bar (87.6% reduction). Thus, while percrystallization and DCMD provided more stable high-purity water recovery, pressure-driven NF/UF were limited by progressive cake resistance.

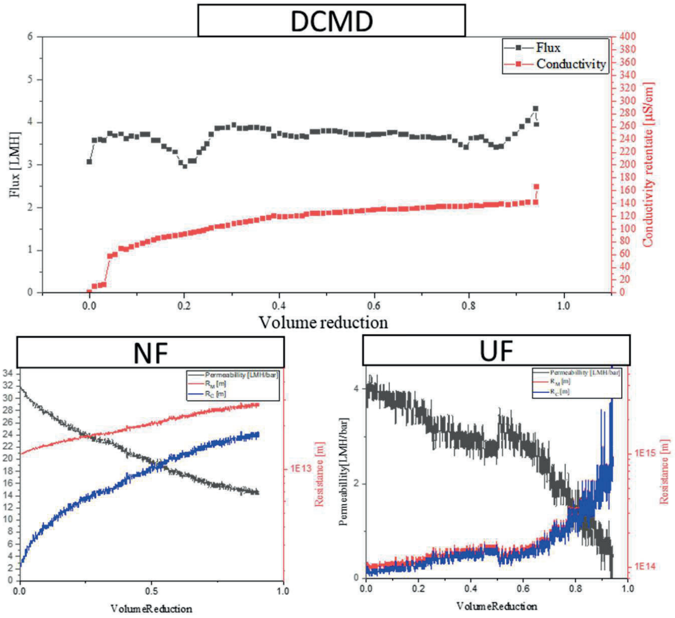

Figure 3-13: Top: Flux (red) and permeate conductivity of a DCMD experiment on color wastewater as a function of volume reduction (Olsen et al. [301]) Bottom Left: Permeability (black), membrane resistance (red) and cake resistance (blue) of pressure

filtration with NF membrane. Bottom right: Permeability (black), membrane resistance (red) and cake resistance (blue) of pressure filtration with UF membrane [Paper(V)].

3.4.3 Process selectivity

Building on these flux and stability comparisons, percrystallization also proved to be a robust ZLD method for anodizing wastewater, producing high-quality water with greater operational stability than DCMD. Since flux performance alone does not capture treatment efficacy, selectivity was further assessed for both NF and UF membranes (Figure 3-14). Given its smaller pore size and lower molecular weight cut-off, NF generally provides higher rejection of multivalent ions than UF. Accordingly, rejection of trace metals (Cu, Cr), color, and dry matter was analyzed under both pressure-driven and percrystallization modes. Under pressure-driven operation, NF outperformed UF across most parameters, except for Cr where both experienced similar rejections. In percrystallization, NF again showed higher overall rejection, though its selectivity decreased relative to pressure-driven operation, consistent with the known effects of elevated temperature reducing rejection in dense membranes [306,307]. Conversely, UF rejection of dry matter improved in percrystallization compared to pressure-driven mode, likely due to solute back diffusion back into the feed, consistent with earlier observations (section 3.3). These observations are analogous to the effects observed in FO systems termed reverse solute flux [307,308]. Here solutes diffuse back into the feed due to increased concentrations on the draw (permeate) side. XRD analysis of recovered crystals further underscored these differences. NF-derived solids exhibited distinct $AlPO_4$ and CrO_2 peaks at 9.0°, 23.0°, and 34.0° 2θ, reflecting the anodizing industry wastewater composition (high in Cr and Al). UF crystals contained the same phases but also additional peaks at 27.3°, 31.1°, and 32.2° 2θ, indicating greater compositional diversity and lower selectivity. Overall, while NF consistently provided superior solute rejection, membrane choice influenced both concentration-based selectivity and the crystalline phases formed, suggesting opportunities for controlled selective crystallization.

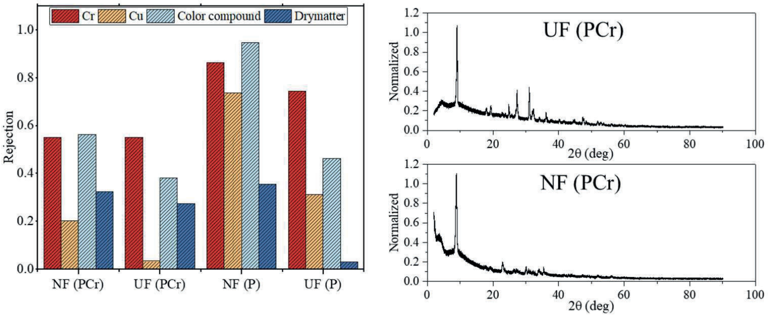

Figure 3-14. Left: Membrane rejection in percrystallization and pressure driven system for Cr, Cu, color compound and drymatter. Right: XRD graph of percrystallization crystals for either UF or NF membrane. Nb: PCr=percrystallization and P=pressure driven [Paper(V)].

3.4.4 Summary

This work demonstrated that industrial wastewater can be effectively treated using percrystallization. The process achieved fluxes comparable to conventional DCMD or better while operating at feed temperatures >10 °C lower, resulting in significantly higher permeability. Additionally, the percrystallization setup proved more robust, as the MD system experienced membrane wetting and feed leakage into the permeate. Membrane selectivity was notably reduced during percrystallization compared to pressure-driven operation, but showed some selectivity in the produced crystals. Nevertheless, both UF and NF membranes were suitable for treating the wastewater, whereas under pressure only the NF membrane achieved substantial desalination. Although overall selectivity was lower, measurable differences between NF and UF performance were observed, indicating that membrane choice influences outcomes. This aspect warrants further investigation to better understand and optimize selectivity in percrystallization processes.

3.5. Percrystallization of food industry wastewater (Sugar-beet washwater)

In the previous section, percrystallization successfully achieved ZLD on anodization wastewater at temperatures comparable to the industry's own waste heat streams. Biorefineries, which refine biomass for applications ranging from food production to fuels, represent a rapidly growing sector [309]. However, biorefinery effluents pose significant challenges for membrane processes due to high levels of suspended solids, large organic molecules, and surfactants, all of which contribute to fouling and, in conventional MD, increase the risk of wetting [310–312]. Employing a low-pressure thermal separation process with hydrophilic membranes offers a promising alternative to conventional membrane methods in this context. Among biorefinery operations, sugar refining is particularly known for generating substantial wastewater volumes rich in suspended solids and organic matter [313]. Furthermore, due to most sugar refineries relying on evaporative crystallization, there is a relatively high amount of thermal energy wasted from the process which could be used in thermal desalination processes, such as MD or Percrystallization. Accordingly, this section investigates percrystallization applied to real sugar-beet wash water sourced from the Nordzucker plant in Denmark, to further demonstrate the method's versatility as a one-step thermal treatment capable of handling highly contaminated feed streams. The results presented here are primarily based on Appendix 3 [A3].

3.5.1 Wash water processing

In sugar refineries, there are multiple water streams. In the Nordzucker's plant in Nakskov, Denmark, 2.5 million tons of sugar beets are processed each year [314]. And since sugar beets contain about 75% water this generates up to 1.9 million tons of water which needs to be treated annually. At the specific plant at Nakskov up to 90% of the water is recycled as mostly washwater for the process of washing the sugar beets before processing [314]. Therefore, most of the reject water from these plants are in the form of wash water reject. This effluent is known to have a high content of organic(biopolymers, oils and grease) and aswell as inorganic compounds [315,316]. These organic compounds are known to inhibit MD processes by changing the surface charge of the membrane and result in wetting [317]. Furthermore, this washwater not only contains a lot of dissolved compounds, but a large fraction is also suspended solids usually >85NTU [315]. In this study the wastewater was measured to be much higher than what was reported, here it was 78.6 NTU when diluted 1:100. Furthermore the drymatter content was measured to be 2.01%. A picture of the feed water can be seen in Figure 3-15.

Figure 3-15. Picture of sugar beet wash water from Nordzucker plant Nakskov, Denmark, depicting high concentration of suspended solids [A3].

The sugar-beet wash water was subsequently processed using an NF99HF membrane at a flow rate of 10 L/h and an inlet temperature of 61.16 ± 1.31 °C. Thirteen batches were run until a cumulative volume reduction of 98% was achieved over 600 hours, representing the long stability even with this hard to process feed. The system maintained a relatively stable average flux of 2.55 ± 0.50 LMH as seen in Figure 3-16. Crystallization was observed almost immediately on the membrane surface, consistent with results for anodization wastewater and seawater, again demonstrating percrystallization's ability to produce solid permeate at any stage. As expected, feed concentration increased over time, reflected by rising conductivity. However, during the 11th cycle, conductivity began to decline and eventually stabilized. This pattern resembles the characteristic drop associated with supersaturation and the onset of bulk precipitation [318,319]. Despite likely precipitation on the feed side, water transport remained unaffected, further underscoring the robustness of percrystallization under demanding conditions.

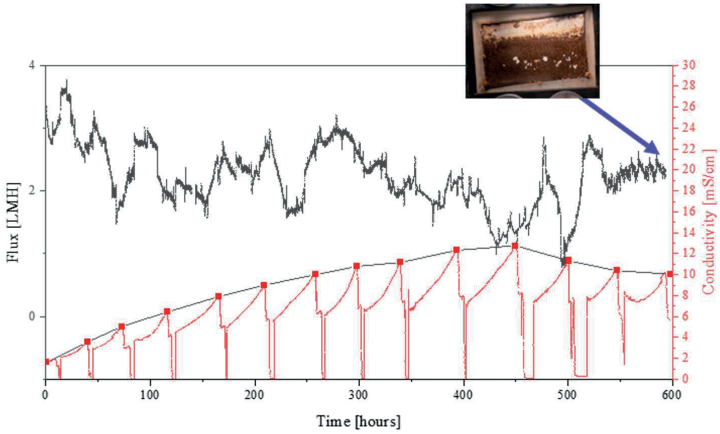

Figure 3-16: Plot of water flux (black) and feed conductivity (red) of sugar beet wash water desalination experiment over 600h with 13 cycles of refilling reaching 96% volume reduction. Additionally, a picture of membrane surface after experiment with crystals. [A3].

Phosphorous was detected in the feed wash water. Further analysis of the phosphorous content in the feed, showed that the feed has a 10.3 mg/L concentration, which when processed to 96% volume reduction would result in 15.2 mg/L, leading to a crystallization of 65.1 mg phosophorus or 97% recovery of phosophorous. Phosphorous is one of the critical elements considered by the EU as mentioned in section(1.1.3). By using percrystallization, it is thereby possible to extract the phosphorus from waste streams which could be used as or further refined into high quality fertilizer. This could beneficially further be explored and the retentate and permeate be quantified for fertilizer quality.

3.5.2 Summary

These results demonstrate that percrystallization can function as a one-step ZLD solution for highly contaminated biorefinery wastewater, maintaining relatively high fluxes even at 98% volume reduction and using low grade heat. The process achieved continuous percrystallization, operating successfully for over 600 hours and highlighting the method's maturity and robustness. The output of the method showed promise as a source of phosphorous further valorizing the process. Furthermore, the batch based evaporative crystallization in sugar refineries could possibly be exchanged to a percrystallization method, which could provide possibly provide a continuous one step method for producing sugar crystals. However, these findings are preliminary, and further studies are warranted to explore the full potential of percrystallization in biorefinery applications.

3.6. General summary and perspective on percrystallization

This thesis proposes a new percrystallization system using inexpensive, commercially available polymeric membranes, commonly applied in pressure-driven separations, to desalinate brines. The method effectively concentrated feed streams while producing pure water and recoverable crystals. Water fluxes were comparable to, or slightly higher than, conventional MD, and the process demonstrated robust, low-fouling performance across diverse feeds, from seawater and industrial wastewater to muddy wash water, with continuous operation exceeding 600 hours. Percrystallization also enables selective solute transport, although selectivity was limited under the modest temperatures and pressures used here. Introducing reactive sweeping gases, such as CO_2, enhanced selective crystallization at the membrane interface. Other reactive gases, like ammonia, could be explored for this purpose. Volume reductions up to 98% were achieved, with flux ranging from 2 to 7.38 LMH, strongly influenced by feed composition, membrane type, and temperature. A summary of flux, permeability, and volume reduction results, including MD and pressure-driven UF and NF benchmarks, as well as literature data, is provided in Table 3-4. While vacuum-assisted percrystallization achieves higher fluxes (9.43–32 LMH), the permeability values observed here (3.8–58.38 LMH/bar) are comparable to vacuum-assisted systems (10.27–30 LMH/bar), suggesting similar transport mechanisms. This indicates that applying vacuum to UF membranes could further enhance evaporation.

However, vacuum operation introduces drawbacks: higher flooding risk, increased system complexity and system pressure requirements. Moreover, vacuum systems require more electrical energy, whereas non-vacuum configurations can potentially operate solely on thermal energy, such as industrial waste heat. Finally, vacuum may exacerbate fouling by driving contaminants deeper into membrane pores, similar to pressure-driven processes.

Overall, this study should not be seen as competing with vacuum-assisted percrystallization but as expanding the range of potential configurations. The optimal percrystallization approach will depend on feed characteristics and operational constraints. Importantly, this work demonstrates that using standard polymeric flat-sheet membranes offers a more scalable alternative to the specialized membranes commonly reported in the literature, which simultaneously show competitive water permeability (Table 3-4).

Table 3-4, Table of desalintation types compared to percrytallization results (Process type, membrane type, flux, permeabillity, Volume reduction/operation time)

Process type (membrane type)	Feed type	Water flux [LMH] (Permeability) [LMH/bar]	Volume reduction	Literature
Percrystallization (NF)	Deionized water	3.25 (17.07)	NA (6h)	Paper(V)
Percrystallization (UF)	Deionized water	7.38 (58.38)	NA (6h)	Paper(V)
Percrystallization (NF)	Seawater	4.50-2.50 (18.29)	91.7%	Paper(IV)
Percrystallization (UF)	Seawater	4.91 (35.12)	50%	Paper(IV)
Percrystallization (NF)	Color wastewater	~2 to ~0.5 (15 – 3.8)	90%	Paper(V)
Percrystallization (UF)	Color wastewater	~5 to ~2 (39 - 16)	90%	Paper(V)
Pressure (NF)	Color wastewater	24.72 (4.12)	90%	Paper(V)
Pressure (UF)	Color wastewater	94.95 (31.65)	90%	Paper(V)

DCMD (MF)	Color wastewater	3.13 (7.56)	90%	[301]
DCMD (VPP-PIPS)	Deionized water	5.93 (14.59)	NA	Paper(II)
Percrystallization (NF)	Sugar beet wash water	2.55 (15.27)	98% (+600h)	[A3]
Vacuum percrystallization (Modified)	NaCl solution	9.43 (10.27)	NA	[263]
Vacuum percrystallization (Modified)	NaCl solution	32 (30)	NA (120h)	[258]
Vacuum percrystallization (Modified)	Na_2SO_4 solution	22 (~22)	NA	[257]

Limitations and Future Perspectives

Percrystallization represents a promising alternative to conventional thermal desalination, offering high flux, recoverable crystals, broad membrane compatibility, and operational robustness that in some respects surpass conventional MD. However, challenges remain. For example, packing density may be more difficult to optimize in percrystallization due to the permeate-side area needed for crystal deposition.

Permeate Heating: This study employed feed-side heating, which effectively demonstrates compatibility with waste heat. However, temperature polarization can cause the membrane surface temperature to be significantly lower than the bulk feed temperature. This limitation could potentially be mitigated by heating the permeate side via air heaters or heat lamps.

Heat Recovery: Like other evaporation-based processes, percrystallization is inherently limited by the latent heat of vaporization, making it energy-intensive if "free" heat sources (solar, geothermal, industrial) are unavailable. To improve competitiveness relative to pressure-driven processes, future implementations could integrate heat recovery through multistage configurations or mechanical vapor compression.

Selectivity: Though some selectivity was here demonstrated, selectivity remains a challenge. While percrystallization can remove selectively remove larger compounds such as colloids and debris, membranes alone offer limited ion selectivity. Chemical treatment, as demonstrated by selective Mg and Ca precipitation, or pre-treatment with pressure-driven membranes could improve separation efficiency. Percrystallization could then serve as a final polishing step for brine mining and ZLD.

New Membranes: This work showed that membrane properties can influence selective crystallization, though selectivity was lower compared to pressure-driven operation. Developing membranes specifically tailored for low-pressure, elevated-temperature environments will be critical to achieving efficient selective crystallization. Improving selectivity could significantly enhance percrystallization's viability and help offset thermal desalination costs.

Additionally, optimizing membrane permeability is essential for maximizing flux. For example, UF membranes demonstrated substantially higher throughput. Recent advances in VPP–PIPS have shown that 3D-printed membranes can achieve highly controlled permeability [182]. Fully printing membranes also enables precise control over thickness, which was found to correlate linearly with permeability. Increased thickness could also amplify concentration polarization, potentially promoting earlier crystallization.

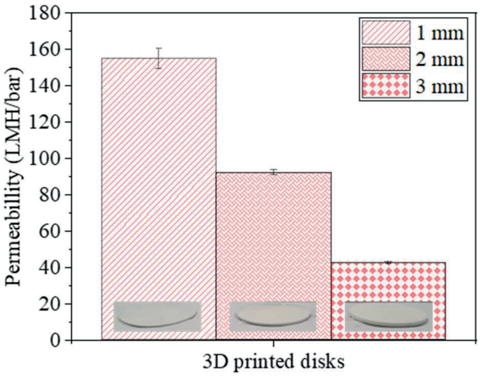

Figure 3-17, Permeability of VPP-PIPS, 3D printed disks with different thicknesses, showcasing the control of liquid flow (Kirkebæk et, al. [182].)

This approach enables the use of membranes with MF-scale pore sizes and the fabrication of surfaces with tailored geometries. Such designs could increase the effective evaporation area, similar to the enhanced heat transfer observed in heat sinks [320]. Membranes of this type were produced during this PhD work and were successfully tested in percrystallization, as shown in Figure 3-18. However, due to the mechanical strength limitations described in Chapter 2, further use of these membranes was deferred until more robust materials can be developed.

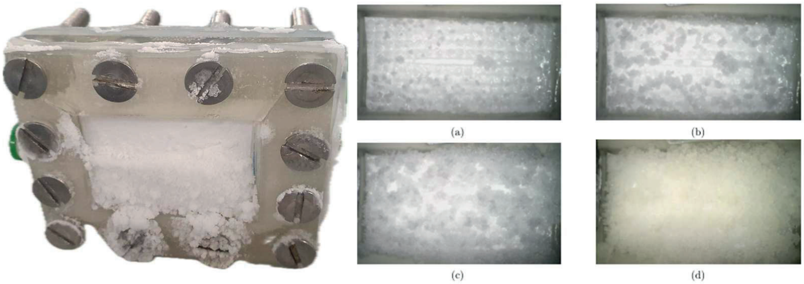

Figure 3-18, VPP-PIPS printed MF membranes, left: full membrane module and membrane with precipitating NaCl crystals. Right: 3D printed membrane topography a, b, c and d pictures of precipitation over time (Steen A, et Al. [321]).

Chapter 4 Expanded thesis summary

Zero liquid discharge (ZLD) is critical both to minimize liquid waste, which can have severe environmental impacts and increase production costs, and to enable brine mining, which can recover valuable resources and help address raw material scarcity. Membrane technologies are at the forefront of water treatment due to their reliable performance, cost effectiveness, and high solute selectivity. However, most conventional membrane methods, including RO, FO and ED, are limited by parameters such as high salinity and cannot independently achieve ZLD. Thermally driven membrane crystallization (MCr) remains among the most promising solutions for treating high-salinity brines and achieving ZLD while producing distillate grade pure water, often exceeding the quality obtainable by RO and ED. Nonetheless, MCr is a relatively recent development, and challenges such as membrane wetting, fouling, and limited selectivity must be addressed to enable effective ZLD and brine mining.

This thesis addresses these issues through two primary strategies:

1. Developing additive manufacturing (AM) methods for advanced MD/MCr membranes

2. Further advancing and evaluating percrystallization for real seawater and industrial brines

Additive Manufacturing

In this work, VPP–PIPS was employed to overcome the trade-off between resolution and build size characteristic of AM techniques. VPP–PIPS preserves the geometric precision and resolution of VPP while enabling tunable porosity and pore size through phase separation, similar to conventional phase inversion. Membranes with adjustable physicochemical properties, including contact angle, thermal stability, and mechanical strength were fabricated by copolymerizing polyurethane acrylate (PUA), hydroxyethyl methacrylate (HEMA), and tert-butyl acrylate (tBA). This approach yielded materials spanning from highly hydrophilic to highly hydrophobic, with mechanical strength and thermal stability suitable for applications ranging from pressure filtration to MD. The advantages of VPP were further demonstrated by producing microscale surface features via DLP printing, which increased the contact angle in accordance with the Wenzel model. Fully 3D-printed VPP–PIPS hydrophobic tubular membranes based on tert-butyl acrylate were successfully produced, exhibiting high temperature resistance and demonstrating potential for new geometries, such as internal riffling, to improve mixing, although the benefits of such designs require further validation. These membranes demonstrated tunable geometries and porosity reflected in their permeation performance, showing competitive flux and PFAS-free alternatives to conventional PTFE membranes, with stable operation even near NaCl saturation. However, scaling remained a challenge affecting flux stability. To further improve processability while retaining AM benefits, porous topographies were directly printed onto commercial membranes, enhancing surface area and hydrodynamics. These integrated structures mitigated permeability decline due to fouling and caking, achieving up to 192% higher flux. Similar porous spacers were printed onto MD membranes to explore their impact on MCr, particularly regarding nucleation control and contact angle effects.

Percrystallization

Conventional MD and MCr face persistent limitations, particularly fouling, wetting, limited selectivity, and challenges with crystal recovery. This thesis investigated percrystallization as a novel membrane crystallization process capable of achieving ZLD and simultaneous mineral recovery. A custom percrystallization system was designed and built to process real seawater and industrial wastewater under thermal driving forces without applied vacuum. Experimental results demonstrated continuous volume reduction and production of dry, recoverable crystals with minimal fouling. Stable fluxes comparable to membrane distillation were maintained over extended operations exceeding 160 hours for seawater and over 600 hours for biorefinery wastewater, consistently producing ultrapure permeate water even at high salinity. Selective crystallization mechanisms were explored, including the influence of membrane pore structure and material on solute transport and nucleation. The effect of sweeping gas composition, such as introducing CO_2 to promote selective carbonate precipitation, was also examined to enhance resource recovery. Comparative analyses with conventional MD and pressure-driven processes highlighted percrystallization’s advantages in fouling resistance, mineral selectivity, and operational simplicity. Overall, percrystallization is presented as a promising low-pressure thermal desalination technology that complements additive-manufactured membranes, advancing the field toward more sustainable ZLD and brine mining solutions.

Chapter 5 Future works

Although novel VPP–PIPS membranes with microstructured topographies were successfully produced in this work, these membranes remain in the early stages of development. Further research is needed to elucidate how the superior control over membrane properties and high-resolution geometries afforded by VPP–PIPS influence crystallization behavior. Additionally, scaling up the process will be essential to enable practical implementation in real-world applications. Furthermore, due to the direct synthesis of the membrane polymer many new possible membrane materials can be produced which include the possibillity of doping with particulates including catalysts. Relevant for further investigation for next generation membranes.

Percrystallization demonstrated significant improvements in addressing challenges commonly faced by MD/MCr, processing a wide range of feed streams while yielding recoverable solids. Although some evidence of selective crystallization was observed, overall selectivity remained limited. This is likely attributable to the use of commercial membranes operating at high temperatures and low pressures, conditions that can reduce membrane selectivity. Accordingly, evaluating membrane performance under lower temperature and pressure conditions is warranted.

Furthermore, exploring membrane geometries beyond conventional flat-sheet configurations could be advantageous for percrystallization. Integrating VPP–PIPS membranes into percrystallization systems represents a promising direction for future investigation.

Chapter 6 Other works

6.1. Published works

I. Xianzheng Ma, Lana Flanjak, XinXin Chen, Carmelo Morgante, **Bastian Stiem Kirkebæk,** Vittorio Boffa, Cejna Anna Quist-Jensen, Aamer Ali, Valter Maurino, Peter Roslev, Efficient treatment of high-salinity aquaculture effluents through synergistic membrane distillation and VUV/UVC photolysis. Journal of Water Process Engineering, Volume 66, September 2024, 106042 (2024)
II. Mohammad Mahdi A. Shirazi, **Bastian S. Kirkebæk**, Aamer Ali, Cejna A. Quist-Jensen. Membrane crystallization for resource recovery from brine towards sustainability and circular economy. Science Talks, (2024)
III. Chimanlal, Indira; Nthunya, Lebea N.; Mahlangu, Oranso T.; **Kirkebæk, Bastian**; Ali, Aamer; Quist-Jensen, Cejna A.; Richards, Heidi. Nanoparticle-Enhanced PVDF Flat-Sheet Membranes for Seawater Desalination in Direct Contact Membrane Distillation. Membranes (2023)
IV. **Bastian Kirkebæk**, Gustav Simoni, Ingrid Lankveld, Martin Poulsen, Morten Christensen, Cejna Anna Quist-Jensen, Donghong Yu, Aamer Ali. Oleic acid-coated magnetic particles for removal of oil from produced water. Journal of Petroleum Science and Engineering (2022)
V. Gustav Simoni, **Bastian Stiem Kirkebæk**, Cejna Anna Quist-Jensen, Morten Lykkegaard Christensen, Aamer Ali. A comparison of vacuum and direct contact membrane distillation for phosphorus and ammonia recovery from wastewater. Journal of Water Process Engineering (2021)

6.2. Conference Proceedings

I. **Bastian Stiem Kirkebæk**, Cejna Anna Quist-Jensen, Aamer Ali, Breaking limitations of conventional 3D printing for membrane synthesis, Nordic Filtration symposium (2022)
II. **Bastian Stiem Kirkebæk**, Cejna Anna Quist-Jensen, Aamer Ali, 3D printing in the field of membrane distillation and membrane crystallization, Network of young membrains (2022)
III. **Bastian Stiem Kirkebæk**, Cejna Anna Quist-Jensen, Aamer Ali, New routes for 3D printing of membranes with controlled properties, Euromembrane conference (2022)
IV. **Bastian Stiem Kirkebæk** Aamer Ali, Magnetic micro vehicles to pickup small oil droplets from water, DWF 16th Annual water research conference (2022)
V. **Bastian Stiem Kirkebæk**, Anders Emuel Olsen, Cejna Anna Quist-Jensen, Aamer Ali, Advancements in 3D printing of membranes, Nordic Filtration symposium (2024)
VI. **Bastian Stiem Kirkebæk**, Cejna Anna Quist-Jensen, Aamer Ali, 3D Printed Membranes For Water And Wastewater Treatment, IWA World Water Congress and exhibition (2024)
VII. **Bastian Stiem Kirkebæk**, Cejna Anna Quist-Jensen, Aamer Ali, Anders Emuel Olsen, Percrystallization: A versatile Approach for Desalination and Zero Liquid Discharge, DWF water conference (2025)

Literature list

[1] Forecast of global water demand | European Environment Agency's home page, (n.d.). https://www.eea.europa.eu/en/analysis/maps-and-charts/forecast-of-global-water-demand (accessed November 15, 2024).

[2] A. Boretti, L. Rosa, Reassessing the projections of the World Water Development Report, Npj Clean Water 2019 2:1 2 (2019) 1–6. https://doi.org/10.1038/s41545-019-0039-9.

[3] World water demand 2040 | Statista, (n.d.). https://www.statista.com/statistics/216527/global-demand-for-water/ (accessed November 15, 2024).

[4] Goal 6 | Department of Economic and Social Affairs, (n.d.). https://sdgs.un.org/goals/goal6 (accessed November 15, 2024).

[5] Water Science School, How Much Water is There on Earth?, Https://Www.Usgs.Gov/Special-Topics/Water-Science-School/Science/How-Much-Water-There-Earth (2019).

[6] Water Facts - Worldwide Water Supply | ARWEC| CCAO | Area Offices | California-Great Basin | Bureau of Reclamation, (n.d.). https://www.usbr.gov/mp/arwec/water-facts-ww-water-sup.html (accessed April 24, 2025).

[7] Annual freshwater withdrawals, total (billion cubic meters) | Data, (n.d.). https://data.worldbank.org/indicator/ER.H2O.FWTL.K3 (accessed June 30, 2025).

[8] Y.A.C. Jande, M.B. Minhas, W.S. Kim, Ultrapure water from seawater using integrated reverse osmosis-capacitive

deionization system, Desalination Water Treat 53 (2015) 3482–3490. https://doi.org/10.1080/19443994.2013.873352.

[9] Ultrapure Water Market, Industry Size Forecast Trends Report, [Latest], (n.d.). https://www.marketsandmarkets.com/Market-Reports/ultrapure-water-market-88839327.html (accessed May 4, 2025).

[10] A. Panagopoulos, K.J. Haralambous, Environmental impacts of desalination and brine treatment - Challenges and mitigation measures, Mar Pollut Bull 161 (2020) 111773. https://doi.org/10.1016/J.MARPOLBUL.2020.111773.

[11] M.O. Saeed, M.M. Ershath, I.A. Al-Tisan, Perspective on desalination discharges and coastal environments of the Arabian Peninsula, Mar Environ Res 145 (2019) 1–10. https://doi.org/10.1016/J.MARENVRES.2019.02.005.

[12] THE 17 GOALS | Sustainable Development, (n.d.). https://sdgs.un.org/goals (accessed May 8, 2025).

[13] F. Nakhaei, J. Corchado-Albelo, L. Alagha, M. Moats, N. Munoz-Garcia, Progress, challenges, and perspectives of critical elements recovery from sulfide tailings, Sep Purif Technol 354 (2025) 128973. https://doi.org/10.1016/J.SEPPUR.2024.128973.

[14] History of the European Union – 1945-59 | European Union, (n.d.). https://european-union.europa.eu/principles-countries-history/history-eu/1945-59_en (accessed July 30, 2025).

[15] European Coal and Steel Community (ECSC) | Britannica, (n.d.). https://www.britannica.com/topic/European-Coal-and-Steel-Community (accessed July 30, 2025).

[16] COMMISSION OF THE EUROPEAN COMMUNITIES, The raw materials initiative-meeting our critical needs for growth and jobs in Europe, 2008. http://ec.europa.eu/enterprise/non_energy_extractive_industries/raw_materials.htm.

[17] Critical raw materials - European Commission, (n.d.). https://single-market-economy.ec.europa.eu/sectors/raw-materials/areas-specific-interest/critical-raw-materials_en (accessed August 4, 2025).

[18] M.L. Vera, W.R. Torres, C.I. Galli, A. Chagnes, V. Flexer, Environmental impact of direct lithium extraction from brines, Nature Reviews Earth & Environment 2023 4:3 4 (2023) 149–165. https://doi.org/10.1038/s43017-022-00387-5.

[19] A. del Villar, J. Melgarejo, M. García-López, P. Fernández-Aracil, B. Montano, The economic value of the extracted elements from brine concentrates of Spanish desalination plants, Desalination 560 (2023) 116678. https://doi.org/10.1016/J.DESAL.2023.116678.

[20] B.K. Pramanik, L.D. Nghiem, F.I. Hai, Extraction of strategically important elements from brines: Constraints and opportunities, Water Res 168 (2020) 115149. https://doi.org/10.1016/J.WATRES.2019.115149.

[21] J. Lee, S. Lee, Challenges, opportunities, and technological advances in desalination brine mining: a mini review, Advances in Industrial and Engineering Chemistry 2025 1:1 1 (2025) 1–16. https://doi.org/10.1007/S44405-025-00007-Y.

[22] L. ALI, ABOUT THE MAINTENANCE OF THE HEAT FLOW EXCHANGERS FROM ENERGETICALLY NAVAL SYSTEMS, Scientific Bulletin of Naval Academy 19 (2016) 139–146. https://doi.org/10.21279/1454-864X-16-I1-023.

[23] International trade in critical raw materials - Statistics Explained - Eurostat, (n.d.). https://ec.europa.eu/eurostat/statistics-explained/index.php?title=International_trade_in_critical_raw_materials#Magnesium (accessed May 5, 2025).

[24] Jan. Post, P. de. Jong, Matthew. Mallory, Mathieu. Doussineau, Ales. Gnamus, Smart specialisation in the context of blue economy : analysis of desalination sector, Publications Office of the European Union, 2021.

[25] L.A. Papp, J. Cardinali-Rezende, W.A. de S. Júdice, M.B. Sanches, W.L. Araújo, Total phosphorus contents currently found in the raw wastewater – Problems and technical solutions for its removal in full-scale wastewater treatment plants, Resour Conserv Recycl 196 (2023) 107026. https://doi.org/10.1016/J.RESCONREC.2023.107026.

[26] P. Panagos, J. Köningner, C. Ballabio, L. Liakos, A. Muntwyler, P. Borrelli, E. Lugato, Improving the phosphorus budget of European agricultural soils, Science of the Total Environment 853 (2022). https://doi.org/10.1016/j.scitotenv.2022.158706.

[27] European Union Lithium carbonates imports | 2023 | Data, (n.d.). https://wits.worldbank.org/trade/comtrade/en/country/EUN/year/2023/tradeflow/Imports/partner/WLD/product/283691?utm_source=chatgpt.com (accessed June 30, 2025).

[28] B. Sanjuan, B. Gourcerol, R. Millot, D. Rettenmaier, E. Jeandel, A. Rombaut, Lithium-rich geothermal brines in Europe: An up-date about geochemical characteristics and implications for potential Li resources, Geothermics 101 (2022) 102385. https://doi.org/10.1016/J.GEOTHERMICS.2022.102385.

[29] M.M.A. Shirazi, B.S. Kirkebæk, A. Ali, C.A. Quist-Jensen, Membrane crystallization for resource recovery from brine towards sustainability and circular economy, Science Talks 11 (2024) 100367. https://doi.org/10.1016/J.SCTALK.2024.100367.

[30] R.M. DuChanois, N.J. Cooper, B. Lee, S.K. Patel, L. Mazurowski, T.E. Graedel, M. Elimelech, Prospects of metal recovery from wastewater and brine, Nature Water 1 (2023) 37–46. https://doi.org/10.1038/S44221-022-00006-Z;SUBJMETA=166,172,639,704;KWRD=ENGINEERING,ENVIRONMENTAL+SCIENCES.

[31] B.Z. Asli, N. McIntyre, S. Djordjevic, R. Farmani, L. Pagliero, A closer look at the history of the desalination industry: the evolution of the practice of desalination through the course of time, Water Supply 23 (2023) 2517–2526. https://doi.org/10.2166/WS.2023.135.

[32] A. Abdulsalam, A. Idris, T. A. Mohamed, A. Ahsan, The development and applications of solar pond: a review, Desalination Water Treat 53 (2015) 2437–2449. https://doi.org/10.1080/19443994.2013.870710.

[33] H.A. Kooijman, E. Sorensen, Recent advances and future perspectives on more sustainable and energy efficient distillation processes, Chemical Engineering Research and Design 188 (2022) 473–482. https://doi.org/10.1016/J.CHERD.2022.10.005.

[34] J. Woodward, M.J. Siegert, A.M. Smith, N. Ross, Latent Heat of Vaporization/Condensation, Encyclopedia of Earth Sciences Series Part 3 (2011) 703–703. https://doi.org/10.1007/978-90-481-2642-2_327.

[35] A. Al-Karaghouli, L.L. Kazmerski, Energy consumption and water production cost of conventional and renewable-energy-powered desalination processes, Renewable and Sustainable Energy Reviews 24 (2013) 343–356. https://doi.org/10.1016/J.RSER.2012.12.064.

[36] B.Z. Asli, N. McIntyre, S. Djordjevic, R. Farmani, L. Pagliero, A closer look at the history of the desalination industry: the evolution of the practice of desalination through the course of time, Water Supply 23 (2023) 2517–2526. https://doi.org/10.2166/WS.2023.135.

[37] T.A. Geleta, I.V. Maggay, Y. Chang, A. Venault, Recent Advances on the Fabrication of Antifouling Phase-Inversion Membranes by Physical Blending Modification Method, Membranes 2023, Vol. 13, Page 58 13 (2023) 58. https://doi.org/10.3390/MEMBRANES13010058.

[38] M.N. Kleinberg, C. Thamaraiselvan, C.D. Powell, C.J. Arnusch, Preserved subsurface morphology in NIPS and VIPS laser-induced graphene membranes affects electrically-dependent microbial decontamination, J Memb Sci 673 (2023) 121481. https://doi.org/10.1016/J.MEMSCI.2023.121481.

[39] L.D. Tijing, J.R.C. Dizon, I. Ibrahim, A.R.N. Nisay, H.K. Shon, R.C. Advincula, 3D printing for membrane separation, desalination and water treatment, Appl Mater Today 18 (2020) 100486. https://doi.org/10.1016/J.APMT.2019.100486.

[40] R. Kamalesh, S. Karishma, A. Saravanan, P.R. Yaashikaa, Emerging breakthroughs in membrane filtration techniques and their application in agricultural wastewater treatment: Reusability aspects, Sustainable Chemistry for the Environment 8 (2024) 100183. https://doi.org/10.1016/J.SCENV.2024.100183.

[41] J.G. Wijmans, R.W. Baker, The solution-diffusion model: a review, J Memb Sci 107 (1995) 1–21. https://doi.org/10.1016/0376-7388(95)00102-I.

[42] A. Imbrogno, J.I. Calvo, M. Breida, R. Schwaiger, A.I. Schäfer, Molecular weight cut off (MWCO) determination in ultra- and nanofiltration: Review of methods and implications on organic matter removal, Sep Purif Technol 354 (2025) 128612. https://doi.org/10.1016/J.SEPPUR.2024.128612.

[43] Factors affecting the SEC of SWRO plants, Seawater Reverse Osmosis (SWRO) Desalination (2023) 73–84. https://doi.org/10.2166/9781789061215_0073.

[44] J. Kim, K. Park, D.R. Yang, S. Hong, A comprehensive review of energy consumption of seawater reverse osmosis desalination plants, Appl Energy 254 (2019) 113652. https://doi.org/10.1016/J.APENERGY.2019.113652.

[45] L. Saleh, M. al Zaabi, T. Mezher, Estimating the social carbon costs from power and desalination productions in UAE, Renewable and Sustainable Energy Reviews 114 (2019) 109284. https://doi.org/10.1016/J.RSER.2019.109284.

[46] E. Jones, M. Qadir, M.T.H. van Vliet, V. Smakhtin, S. mu Kang, The state of desalination and brine production: A global outlook, Science of The Total Environment 657 (2019) 1343–1356. https://doi.org/10.1016/J.SCITOTENV.2018.12.076.

[47] J.M. Gohil, A.K. Suresh, Chlorine attack on reverse osmosis membranes: Mechanisms and mitigation strategies, J Memb Sci 541 (2017) 108–126. https://doi.org/10.1016/J.MEMSCI.2017.06.092.

[48] B.C. Ricci, C.D. Ferreira, L.S. Marques, S.S. Martins, B.G. Reis, M.C.S. Amaral, Assessment of the chemical stability of

nanofiltration and reverse osmosis membranes employed in treatment of acid gold mining effluent, Sep Purif Technol 174 (2017) 301–311. https://doi.org/10.1016/J.SEPPUR.2016.11.007.

[49] M.A. Ahmed, S. Amin, A.A. Mohamed, Fouling in reverse osmosis membranes: monitoring, characterization, mitigation strategies and future directions, Heliyon 9 (2023) e14908. https://doi.org/10.1016/J.HELIYON.2023.E14908.

[50] W. Bai, L. Samineni, P. Chirontoni, I. Krupa, P. Kasak, A. Popelka, N.B. Saleh, M. Kumar, Quantifying and reducing concentration polarization in reverse osmosis systems, Desalination 554 (2023) 116480. https://doi.org/10.1016/J.DESAL.2023.116480.

[51] S.F. Anis, R. Hashaikeh, N. Hilal, Reverse osmosis pretreatment technologies and future trends: A comprehensive review, Desalination 452 (2019) 159–195. https://doi.org/10.1016/J.DESAL.2018.11.006.

[52] F. Yusefi, M.M. Zahedi, M. Ziyaadini, Evaluation for the optimization of two conceptual 200,000 m3/day capacity RO desalination plant with different intake seawater of Oman Sea and Caspian Sea, Appl Water Sci 11 (2021) 12. https://doi.org/10.1007/S13201-020-01338-5.

[53] E.R. Cornelissen, D.J.H. Harmsen, B. Blankert, L.P. Wessels, W.G.J. van der Meer, Effect of minimal pre-treatment on reverse osmosis using surface water as a source, Desalination 509 (2021) 115056. https://doi.org/10.1016/J.DESAL.2021.115056.

[54] L. Masse, D.I. Massé, Y. Pellerin, J. Dubreuil, Osmotic pressure and substrate resistance during the concentration of manure nutrients by reverse osmosis membranes, J Memb Sci

348 (2010) 28–33. https://doi.org/10.1016/J.MEMSCI.2009.10.038.

[55] C. Kleffner, G. Braun, S. Antonyuk, High-Pressure Reverse Osmosis for Industrial Water Recycling: Permeate-Sided Pressure Drop as Performance-Limiting Factor, Chem Ing Tech 93 (2021) 1352–1358. https://doi.org/10.1002/CITE.202100021;PAGEGROUP:STRING:PUBLICATION.

[56] T. Tong, M. Elimelech, The Global Rise of Zero Liquid Discharge for Wastewater Management: Drivers, Technologies, and Future Directions, Environ Sci Technol 50 (2016) 6846–6855. https://doi.org/10.1021/ACS.EST.6B01000/ASSET/IMAGES/LARGE/ES-2016-01000H_0005.JPEG.

[57] I.S. Al-Mutaz, A comparative study of RO and MSF desalination plants, Desalination 106 (1996) 99–106. https://doi.org/10.1016/S0011-9164(96)00097-5.

[58] I.S. Al-Mutaz, MSF challenges and survivals, Desalination Water Treat 177 (2020) 14–22. https://doi.org/10.5004/DWT.2020.24908.

[59] J.B. Tonner, J. Tonner, Desalination and Energy Use, Encyclopedia of Energy (2004) 791–799. https://doi.org/10.1016/B0-12-176480-X/00403-4.

[60] H. Strathmann, Electrodialysis, a mature technology with a multitude of new applications, Desalination 264 (2010) 268–288. https://doi.org/10.1016/J.DESAL.2010.04.069.

[61] R.L. McGinnis, N.T. Hancock, M.S. Nowosielski-Slepowron, G.D. McGurgan, Pilot demonstration of the NH3/CO2 forward osmosis desalination process on high salinity brines,

Desalination 312 (2013) 67–74. https://doi.org/10.1016/J.DESAL.2012.11.032.

[62] W.V. Anderson, C.M. Cheng, T.S. Butalia, L.K. Weavers, Forward osmosis−membrane distillation process for zero liquid discharge of flue gas desulfurization wastewater, Energy and Fuels 35 (2021) 5130–5140. https://doi.org/10.1021/ACS.ENERGYFUELS.0C03415/SUPPL_FILE/EF0C03415_SI_001.PDF.

[63] S. Yadav, I. Ibrar, A. Altaee, A.K. Samal, R. Ghobadi, J. Zhou, Feasibility of brackish water and landfill leachate treatment by GO/MoS2-PVA composite membranes, Science of The Total Environment 745 (2020) 141088. https://doi.org/10.1016/J.SCITOTENV.2020.141088.

[64] T. Alejo, M. Arruebo, V. Carcelen, V.M. Monsalvo, V. Sebastian, Advances in draw solutes for forward osmosis: Hybrid organic-inorganic nanoparticles and conventional solutes, Chemical Engineering Journal 309 (2017) 738–752. https://doi.org/10.1016/J.CEJ.2016.10.079.

[65] J.R. McCutcheon, R.L. McGinnis, M. Elimelech, Desalination by ammonia–carbon dioxide forward osmosis: Influence of draw and feed solution concentrations on process performance, J Memb Sci 278 (2006) 114–123. https://doi.org/10.1016/J.MEMSCI.2005.10.048.

[66] C. Ju, C. Park, T. Kim, S. Kang, H. Kang, Thermo-responsive draw solute for forward osmosis process; poly(ionic liquid) having lower critical solution temperature characteristics, RSC Adv 9 (2019) 29493–29501. https://doi.org/10.1039/C9RA04020J.

[67] N.M. Mazlan, D. Peshev, A.G. Livingston, Energy consumption for desalination — A comparison of forward

osmosis with reverse osmosis, and the potential for perfect membranes, Desalination 377 (2016) 138–151. https://doi.org/10.1016/J.DESAL.2015.08.011.

[68] J.O. Kessler, C.D. Moody, Drinking water from sea water by forward osmosis, Desalination 18 (1976) 297–306. https://doi.org/10.1016/S0011-9164(00)84119-3.

[69] W. Suwaileh, N. Pathak, H. Shon, N. Hilal, Forward osmosis membranes and processes: A comprehensive review of research trends and future outlook, Desalination 485 (2020) 114455. https://doi.org/10.1016/J.DESAL.2020.114455.

[70] S. Lee, Performance Comparison of Spiral-Wound and Plate-and-Frame Forward Osmosis Membrane Module, Membranes (Basel) 10 (2020) 318. https://doi.org/10.3390/MEMBRANES10110318.

[71] A. Samadi, T. Ni, E. Fontananova, G. Tang, H. Shon, S. Zhao, Engineering antiwetting hydrophobic surfaces for membrane distillation: A review, Desalination 563 (2023) 116722. https://doi.org/10.1016/J.DESAL.2023.116722.

[72] A. Boubakri, S.A.-T. Bouguecha, A. Hafiane, A. Boubakri, S.A.-T. Bouguecha, A. Hafiane, Membrane Distillation Process: Fundamentals, Applications, and Challenges, Solvents - Dilute, Dissolve, and Disperse - Insights on Green Solvents and Distillation (2024). https://doi.org/10.5772/INTECHOPEN.1002375.

[73] M.R.S. Kebria, A. Rahimpour, M.R.S. Kebria, A. Rahimpour, Membrane Distillation: Basics, Advances, and Applications, Advances in Membrane Technologies (2020). https://doi.org/10.5772/INTECHOPEN.86952.

[74] R.C. Rodgers, G.E. Hill, EQUATIONS FOR VAPOUR PRESSURE VERSUS TEMPERATURE: DERIVATION AND USE OF THE ANTOINE EQUATION ON A HAND-HELD PROGRAMMABLE CALCULATOR, Br J Anaesth 50 (1978) 415–424. https://doi.org/10.1093/BJA/50.5.415.

[75] M. Mathlouthi, Water content, water activity, water structure and the stability of foodstuffs, Food Control 12 (2001) 409–417. https://doi.org/10.1016/S0956-7135(01)00032-9.

[76] Sigma-Aldrich, Sodium chloride (Halite, Common Salt or Table Salt, Rock Salt), (2018).

[77] M. Omerspahic, H. Al-Jabri, S.A. Siddiqui, I. Saadaoui, Characteristics of Desalination Brine and Its Impacts on Marine Chemistry and Health, With Emphasis on the Persian/Arabian Gulf: A Review, Front Mar Sci 9 (2022) 845113. https://doi.org/10.3389/FMARS.2022.845113/BIBTEX.

[78] D.J. Johnson, W.A. Suwaileh, A.W. Mohammed, N. Hilal, Osmotic's potential: An overview of draw solutes for forward osmosis, Desalination 434 (2018) 100–120. https://doi.org/10.1016/J.DESAL.2017.09.017.

[79] OECD, SIAM 32, (2011).

[80] M. Quilaqueo, G. Seriche, C. González, G. Piaggio, L. Barros, F. Gallardo, S. Díaz-Quezada, D. Zamora, B. Barraza, R. Ruby-Figueroa, S. Santoro, E. Curcio, H. Estay, Membrane distillation-crystallization applied to a multi-ion hypersaline lithium brine for water recovery and crystallization of potassium and magnesium salts, Desalination 586 (2024) 117895. https://doi.org/10.1016/J.DESAL.2024.117895.

[81] C.A. Quist-Jensen, A. Ali, S. Mondal, F. Macedonio, E. Drioli, A study of membrane distillation and crystallization for lithium recovery from high-concentrated aqueous solutions, J Memb Sci 505 (2016) 167–173. https://doi.org/10.1016/J.MEMSCI.2016.01.033.

[82] M. Ahmad, P. Williams, Assessment of desalination technologies for high saline brine applications — Discussion Paper, Desalination Water Treat 30 (2011) 1–15. https://doi.org/10.5004/DWT.2011.1374.

[83] M. Ben Sik Ali, A. Mnif, B. Hamrouni, Modelling of the limiting current density of an electrodialysis process by response surface methodology, Ionics (Kiel) 24 (2018) 617–628. https://doi.org/10.1007/S11581-017-2214-7/FIGURES/10.

[84] L. Wang, C. Violet, R.M. Duchanois, M. Elimelech, Derivation of the Theoretical Minimum Energy of Separation of Desalination Processes, J Chem Educ 97 (2020) 4361–4369. https://doi.org/10.1021/ACS.JCHEMED.0C01194/SUPPL_FILE/ED0C01194_SI_003.PDF.

[85] Chapter 4 Operating principle of electrodialysis and related processes, Membrane Science and Technology 9 (2004) 147–225. https://doi.org/10.1016/S0927-5193(04)80035-4.

[86] J.O. Valderrama, R.A. Campusano, A.S. Toro, Correlation and prediction of saline solution properties for their use in mineral processing using artificial neural networks, Journal of Water Reuse and Desalination 5 (2015) 454–464. https://doi.org/10.2166/WRD.2015.132.

[87] M.M. Generous, N.A.A. Qasem, B.A. Qureshi, S.M. Zubair, A Comprehensive Review of Saline Water Correlations and Data-Part I: Thermodynamic Properties, Arab J Sci Eng 45

(2020) 8817–8876. https://doi.org/10.1007/S13369-020-05019-Y/METRICS.

[88] A. Al-Karaghouli, L.L. Kazmerski, Energy consumption and water production cost of conventional and renewable-energy-powered desalination processes, Renewable and Sustainable Energy Reviews 24 (2013) 343–356. https://doi.org/10.1016/J.RSER.2012.12.064.

[89] G.J. Doornbusch, M. Tedesco, J.W. Post, Z. Borneman, K. Nijmeijer, Experimental investigation of multistage electrodialysis for seawater desalination, Desalination 464 (2019) 105–114. https://doi.org/10.1016/J.DESAL.2019.04.025.

[90] W. Jantaporn, A. Ali, P. Aimar, Specific energy requirement of direct contact membrane distillation, Chemical Engineering Research and Design 128 (2017) 15–26. https://doi.org/10.1016/J.CHERD.2017.09.031.

[91] M.R. Qtaishat, F. Banat, Desalination by solar powered membrane distillation systems, Desalination 308 (2013) 186–197. https://doi.org/10.1016/J.DESAL.2012.01.021.

[92] N. Dow, S. Gray, J. de Li, J. Zhang, E. Ostarcevic, A. Liubinas, P. Atherton, G. Roeszler, A. Gibbs, M. Duke, Pilot trial of membrane distillation driven by low grade waste heat: Membrane fouling and energy assessment, Desalination 391 (2016) 30–42. https://doi.org/10.1016/J.DESAL.2016.01.023.

[93] W. Wang, Y. Shi, C. Zhang, S. Hong, L. Shi, J. Chang, R. Li, Y. Jin, C. Ong, S. Zhuo, P. Wang, Simultaneous production of fresh water and electricity via multistage solar photovoltaic membrane distillation, Nat Commun 10 (2019) 1–9. https://doi.org/10.1038/S41467-019-10817-

6;TECHMETA=128,129;SUBJMETA=4072,4077,4079,639;KWRD=ENERGY+HARVESTING,ENERGY+STORAGE.

[94] T. Moghadamfar, J. López, J.L. Cortina, L.J. del Valle, M. Reig, Optimized ion selectivity in semiaromatic based nanofiltration membranes via PDADMAC and PSS layer-by-layer self-assembly, Sep Purif Technol 365 (2025) 132696. https://doi.org/10.1016/J.SEPPUR.2025.132696.

[95] Y. Song, X. Gao, C. Gao, Evaluation of scaling potential in a pilot-scale NF–SWRO integrated seawater desalination system, J Memb Sci 443 (2013) 201–209. https://doi.org/10.1016/J.MEMSCI.2013.04.048.

[96] X. Sun, H. Zhang, F. Sun, L. Xu, L. Lin, J. Xu, Concept and investigation of Selective Forward Osmosis (SFO) for Salt-Salt Separation as a Pretreatment of Seawater for Resource Utilization, Water Res 258 (2024) 121753. https://doi.org/https://doi.org/10.1016/j.watres.2024.121753.

[97] M. Tian, T. Ma, K. Goh, Z. Pei, J.Y. Chong, Y.-N. Wang, Forward Osmosis Membranes: The Significant Roles of Selective Layer, Membranes (Basel) 12 (2022). https://doi.org/10.3390/membranes12100955.

[98] V. Montiel, V. García-García, E. Expósito, J.M. Ortiz, A. Aldaz, Membrane Processes, Electrodialysis, Encyclopedia of Applied Electrochemistry (2014) 1224–1229. https://doi.org/10.1007/978-1-4419-6996-5_123.

[99] J. Ying, M. Luo, Y. Jin, J. Yu, Selective separation of lithium from high Mg/Li ratio brine using single-stage and multi-stage selective electrodialysis processes, Desalination 492 (2020) 114621. https://doi.org/10.1016/J.DESAL.2020.114621.

[100] G. Simoni, B.S. Kirkebæk, C.A. Quist-Jensen, M.L. Christensen, A. Ali, A comparison of vacuum and direct contact membrane distillation for phosphorus and ammonia recovery from wastewater, Journal of Water Process Engineering 44 (2021) 102350. https://doi.org/10.1016/J.JWPE.2021.102350.

[101] F. Macedonio, C.A. Quist-Jensen, O. Al-Harbi, H. Alromaih, S.A. Al-Jlil, F. Al Shabouna, E. Drioli, Thermodynamic modeling of brine and its use in membrane crystallizer, Desalination 323 (2013) 83–92. https://doi.org/10.1016/J.DESAL.2013.02.009.

[102] M.M.A. Shirazi, A. Ali, C.A. Quist-Jensen, Membrane crystallization for recovery of lithium carbonate crystals: Study on process parameters and salts effect for Li2CO3-NaCl-KCl-LiCl solutions, Desalination 571 (2024) 117109. https://doi.org/10.1016/J.DESAL.2023.117109.

[103] M. Hernández-Suárez, F.A. León, Indirect calculation of Langelier saturation index and sodium adsorption ratio for remineralised waters from data on electrical conductivity and pH prior to and following remineralisation, Desalination Water Treat 230 (2021) 33–37. https://doi.org/10.5004/DWT.2021.27464.

[104] L. Martínez-Díez, M.I. Vázquez-González, Temperature and concentration polarization in membrane distillation of aqueous salt solutions, J Memb Sci 156 (1999) 265–273. https://doi.org/10.1016/S0376-7388(98)00349-4.

[105] H. Liu, K.I. Jacob, Y. Wang, Scaling in membrane distillation (MD): Current state of art insight on mechanisms and Membrane design, Desalination 581 (2024) 117539. https://doi.org/10.1016/J.DESAL.2024.117539.

[106] A. Jones, S. Rigopoulos, R. Zauner, Crystallization and precipitation engineering, Comput Chem Eng 29 (2005) 1159–1166. https://doi.org/10.1016/J.COMPCHEMENG.2005.02.022.

[107] (PDF) Determination of Ksp, ΔG°, ΔH°, and ΔS° for the Dissolution of Calcium Hydroxide in Water a General Chemistry Experiment, (n.d.). https://www.researchgate.net/publication/252787534_Determination_of_Ksp_DG_DH_and_DS_for_the_Dissolution_of_Calcium_Hydroxide_in_Water_a_General_Chemistry_Experiment (accessed August 6, 2025).

[108] Mineral Solubility and Saturation Index, (n.d.). https://www.aqion.de/site/168 (accessed August 6, 2025).

[109] H. Yang, A.J. Florence, Relating induction time and metastable zone width, CrystEngComm 19 (2017) 3966–3978. https://doi.org/10.1039/C7CE00770A.

[110] R.P. Sear, Nucleation: theory and applications to protein solutions and colloidal suspensions, Journal of Physics: Condensed Matter 19 (2007) 033101. https://doi.org/10.1088/0953-8984/19/3/033101.

[111] A.M. Schwartz, A.S. Myerson, Solutions and solution properties, Handbook of Industrial Crystallization (2002) 1–31. https://doi.org/10.1016/B978-075067012-8/50003-3.

[112] Q. Chen, M. Burhan, M.W. Shahzad, D. Ybyraiymkul, F.H. Akhtar, Y. Li, K.C. Ng, A zero liquid discharge system integrating multi-effect distillation and evaporative crystallization for desalination brine treatment, Desalination 502 (2021) 114928. https://doi.org/10.1016/J.DESAL.2020.114928.

[113] A. Ali, C.A. Quist-Jensen, F. Macedonio, E. Drioli, Optimization of module length for continuous direct contact membrane distillation process, Chemical Engineering and Processing: Process Intensification 110 (2016) 188–200. https://doi.org/10.1016/J.CEP.2016.10.014.

[114] M.M.A. Shirazi, A. Ali, C.A. Quist-Jensen, Membrane crystallization for recovery of lithium carbonate crystals: Study on process parameters and salts effect for Li2CO3-NaCl-KCl-LiCl solutions, Desalination 571 (2024) 117109. https://doi.org/10.1016/J.DESAL.2023.117109.

[115] J. Phattaranawik, R. Jiraratananon, A.G. Fane, Heat transport and membrane distillation coefficients in direct contact membrane distillation, J Memb Sci 212 (2003) 177–193. https://doi.org/10.1016/S0376-7388(02)00498-2.

[116] E. Curcio, E. Drioli, Membrane distillation and related operations - A review, Separation and Purification Reviews 34 (2005) 35–86. https://doi.org/10.1081/SPM-200054951;SUBPAGE:STRING:ACCESS.

[117] X. Zhang, R. Koirala, B. Pramanik, L. Fan, Y. Zhang, A. Date, V. Jegatheesan, Performance of membrane distillation assisted crystallization and crystal characteristics for resource recovery from desalination brine, Desalination 574 (2024) 117244. https://doi.org/10.1016/J.DESAL.2023.117244.

[118] J. Kim, J. Kim, S. Hong, Recovery of water and minerals from shale gas produced water by membrane distillation crystallization, Water Res 129 (2018) 447–459. https://doi.org/10.1016/J.WATRES.2017.11.017.

[119] F. Edwie, T.S. Chung, Development of simultaneous membrane distillation–crystallization (SMDC) technology for

treatment of saturated brine, Chem Eng Sci 98 (2013) 160–172. https://doi.org/10.1016/J.CES.2013.05.008.

[120] A. Ali, C.A. Quist-Jensen, F. Macedonio, E. Drioli, Application of Membrane Crystallization for Minerals' Recovery from Produced Water, Membranes 2015, Vol. 5, Pages 772-792 5 (2015) 772–792. https://doi.org/10.3390/MEMBRANES5040772.

[121] M.C. Sparenberg, S. Chergaoui, V. Sang Sefidi, P. Luis, Crystallization control via membrane distillation-crystallization: A review, Desalination 519 (2021) 115315. https://doi.org/10.1016/J.DESAL.2021.115315.

[122] G. Di Profio, S. Tucci, E. Curcio, E. Drioli, Selective glycine polymorph crystallization by using microporous membranes, Cryst Growth Des 7 (2007) 526–530. https://doi.org/10.1021/CG0605990/ASSET/IMAGES/MEDIUM/CG0605990N00001.GIF.

[123] C.A. Quist-Jensen, A. Ali, S. Mondal, F. Macedonio, E. Drioli, A study of membrane distillation and crystallization for lithium recovery from high-concentrated aqueous solutions, J Memb Sci 505 (2016) 167–173. https://doi.org/10.1016/J.MEMSCI.2016.01.033.

[124] F. Macedonio, C.A. Quist-Jensen, O. Al-Harbi, H. Alromaih, S.A. Al-Jlil, F. Al Shabouna, E. Drioli, Thermodynamic modeling of brine and its use in membrane crystallizer, Desalination 323 (2013) 83–92. https://doi.org/10.1016/J.DESAL.2013.02.009.

[125] G.Ashel. Lane, Crystallization, (2018) 115–152. https://doi.org/10.1201/9781351076753-4.

[126] V.I. Kalikmanov, Classical Nucleation Theory, (2013) 17–41. https://doi.org/10.1007/978-90-481-3643-8_3.

[127] E. Drioli, G. Di Profio, E. Curcio, Membrane-assisted crystallization technology, Membrane-Assisted Crystallization Technology 2 (2015) 1–232. https://doi.org/10.1142/P912/SUPPL_FILE/P912_CHAP01.PDF.

[128] S. Luryi, E. Suhir, New approach to the high quality epitaxial growth of lattice-mismatched materials, Appl Phys Lett 49 (1986) 140–142. https://doi.org/10.1063/1.97204.

[129] D.J. Gunn, Effect of surface roughness on the nucleation and growth of calcium sulphate on metal surfaces, J Cryst Growth 50 (1980) 533–537. https://doi.org/10.1016/0022-0248(80)90104-9.

[130] J. Nývlt, The Ostwald Rule of Stages, Crystal Research and Technology 30 (1995) 443–449. https://doi.org/10.1002/CRAT.2170300402.

[131] H. Yang, C.L. Song, Y.X.S. Lim, W. Chen, J.Y.Y. Heng, Selective crystallisation of carbamazepine polymorphs on surfaces with differing properties, CrystEngComm 19 (2017) 6573–6578. https://doi.org/10.1039/C7CE01317E.

[132] A. Ali, C.A. Quist-Jensen, M.K. Jørgensen, A. Siekierka, M.L. Christensen, M. Bryjak, C. Hélix-Nielsen, E. Drioli, A review of membrane crystallization, forward osmosis and membrane capacitive deionization for liquid mining, Resour Conserv Recycl 168 (2021) 105273. https://doi.org/10.1016/J.RESCONREC.2020.105273.

[133] I. Chimanlal, L.N. Nthunya, C. Quist-Jensen, H. Richards, Membrane distillation crystallization for water and mineral

recovery: The occurrence of fouling and its control during wastewater treatment, Frontiers in Chemical Engineering 4 (2022) 1066027. https://doi.org/10.3389/FCENG.2022.1066027/TEXT.

[134] B. Kim, H. Cho, J. Choi, J. Sohn, S. Lee, Fouling-induced wetting of membranes in membrane distillation (MD) systems, Desalination Water Treat 157 (2019) 360–371. https://doi.org/10.5004/DWT.2019.24105.

[135] A.W. Bryson, D. Glasser, W.F. Lutz, Crystallization of ammonium paratungstate — a comparison between batch and continuous crystallizers, Hydrometallurgy 2 (1976) 185–191. https://doi.org/10.1016/0304-386X(76)90027-X.

[136] J.S. Wey, P.H. Karpinski, Batch crystallization, Handbook of Industrial Crystallization (2002) 231–248. https://doi.org/10.1016/B978-075067012-8/50012-4.

[137] M.R.S. Kebria, A. Rahimpour, M.R.S. Kebria, A. Rahimpour, Membrane Distillation: Basics, Advances, and Applications, Advances in Membrane Technologies (2020). https://doi.org/10.5772/INTECHOPEN.86952.

[138] K.W. Lawson, D.R. Lloyd, Membrane distillation, J Memb Sci 124 (1997) 1–25. https://doi.org/10.1016/S0376-7388(96)00236-0.

[139] D.W. Phelps, L. V. Parkinson, J.M. Boucher, J. Muncke, B. Geueke, Per- and Polyfluoroalkyl Substances in Food Packaging: Migration, Toxicity, and Management Strategies, Environ Sci Technol 58 (2024) 5670–5684. https://doi.org/10.1021/ACS.EST.3C03702/ASSET/IMAGES/LARGE/ES3C03702_0002.JPEG.

[140] H.T. Nguyen, H.M. Bui, Y.F. Wang, S.J. You, Non-fluoroalkyl functionalized hydrophobic surface modifications used in membrane distillation for cheaper and more environmentally friendly applications: A mini-review, Sustain Chem Pharm 28 (2022) 100714. https://doi.org/10.1016/J.SCP.2022.100714.

[141] I. Chimanlal, L.N. Nthunya, O.T. Mahlangu, B. Kirkebæk, A. Ali, C.A. Quist-Jensen, H. Richards, Nanoparticle-Enhanced PVDF Flat-Sheet Membranes for Seawater Desalination in Direct Contact Membrane Distillation, Membranes (Basel) 13 (2023) 317. https://doi.org/10.3390/MEMBRANES13030317/S1.

[142] S. Sinha Ray, H. Dommati, J.C. Wang, H.K. Lee, Y.I. Park, H. Park, I.C. Kim, S.S. Chen, Y.N. Kwon, Facile approach for designing a novel micropatterned antiwetting membrane by utilizing 3D printed molds for improved desalination performance, J Memb Sci 637 (2021) 119641. https://doi.org/10.1016/J.MEMSCI.2021.119641.

[143] J. Fischer, M. Wegener, Three-dimensional optical laser lithography beyond the diffraction limit, Laser Photon Rev 7 (2013) 22–44. https://doi.org/10.1002/LPOR.201100046.

[144] S.B. Khan, S. Irfan, S.S. Lam, X. Sun, S. Chen, 3D printed nanofiltration membrane technology for waste water distillation, Journal of Water Process Engineering 49 (2022) 102958. https://doi.org/10.1016/J.JWPE.2022.102958.

[145] S. Roy Barman, P. Gavit, S. Chowdhury, K. Chatterjee, A. Nain, 3D-Printed Materials for Wastewater Treatment, JACS Au 3 (2023) 2930–2947. https://doi.org/10.1021/JACSAU.3C00409/ASSET/IMAGES/LARGE/AU3C00409_0007.JPEG.

[146] B.G. Thiam, A. El Magri, H.R. Vanaei, S. Vaudreuil, 3D Printed and Conventional Membranes—A Review, Polymers (Basel) 14 (2022) 1023. https://doi.org/10.3390/POLYM14051023/S1.

[147] N. Thomas, J. Swaminathan, G. Zaragoza, R.K. Abu Al-Rub, J.H. Lienhard V, H.A. Arafat, Comparative assessment of the effects of 3D printed feed spacers on process performance in MD systems, Desalination 503 (2021) 114940. https://doi.org/10.1016/J.DESAL.2021.114940.

[148] C.D. Ho, M.S. Chiang, C.A. Ng, Performance Analysis of DCMD Modules Enhanced with 3D-Printed Turbulence Promoters of Various Hydraulic Diameters, Membranes 2025, Vol. 15, Page 144 15 (2025) 144. https://doi.org/10.3390/MEMBRANES15050144.

[149] T. Zou, G. Kang, M. Zhou, M. Li, Y. Cao, Submerged vacuum membrane distillation crystallization (S-VMDC) with turbulent intensification for the concentration of NaCl solution, Sep Purif Technol 211 (2019) 151–161. https://doi.org/10.1016/J.SEPPUR.2018.09.072.

[150] Z. Liu, Y. Zhang, X. Lu, X. Wang, X. Zhao, Study of the bubble membrane crystallization process for zero-brine discharge, J Memb Sci 563 (2018) 584–591. https://doi.org/10.1016/J.MEMSCI.2018.06.021.

[151] P.A. Kober, Pervaporation, perstillation and percrystallization, J Memb Sci 100 (1995) 61–64. https://doi.org/10.1016/0376-7388(94)00234-P.

[152] Z.-X.N. Low, Y. Chua, B. Ray, D. Mattia, I. Metcalfe, D. Patterson, Perspective on 3D printing of separation membranes and comparison to related unconventional fabrication

techniques, J Memb Sci 523 (2016). https://doi.org/10.1016/j.memsci.2016.10.006.

[153] L.D. Tijing, J.R.C. Dizon, I. Ibrahim, A.R.N. Nisay, H.K. Shon, R.C. Advincula, 3D printing for membrane separation, desalination and water treatment, Appl Mater Today 18 (2020) 100486. https://doi.org/10.1016/j.apmt.2019.100486.

[154] S.H. Maruf, L. Wang, A.R. Greenberg, J. Pellegrino, Y. Ding, Use of nanoimprinted surface patterns to mitigate colloidal deposition on ultrafiltration membranes, J Memb Sci 428 (2013) 598–607. https://doi.org/10.1016/J.MEMSCI.2012.10.059.

[155] S.H. Maruf, A.R. Greenberg, J. Pellegrino, Y. Ding, Critical flux of surface-patterned ultrafiltration membranes during cross-flow filtration of colloidal particles, J Memb Sci 471 (2014) 65–71. https://doi.org/10.1016/J.MEMSCI.2014.07.071.

[156] S.Y. Jung, Y.J. Won, J.H. Jang, J.H. Yoo, K.H. Ahn, C.H. Lee, Particle deposition on the patterned membrane surface: Simulation and experiments, Desalination 370 (2015) 17–24. https://doi.org/10.1016/J.DESAL.2015.05.014.

[157] N. Lu, W. Zhang, Y. Weng, X. Chen, Y. Cheng, P. Zhou, Fabrication of PDMS surfaces with micro patterns and the effect of pattern sizes on bacteria adhesion, Food Control 68 (2016) 344–351. https://doi.org/10.1016/J.FOODCONT.2016.04.014.

[158] S. Hou, H. Gu, C. Smith, D. Ren, Microtopographic Patterns Affect Escherichia coli Biofilm Formation on Poly(dimethylsiloxane) Surfaces, 27 (2011) 2686–2691. https://doi.org/10.1021/la1046194.

[159] Y. Ding, J. Sun, H.W. Ro, Z. Wang, J. Zhou, N.J. Lin, M.T. Cicerone, C.L. Soles, L.G. Sheng, Thermodynamic underpinnings of cell alignment on controlled topographies, Advanced Materials 23 (2011) 421–425. https://doi.org/10.1002/ADMA.201001757.

[160] M. Ochs, R. Mohammadi, N. Vogel, A. Andrieu-Brunsen, M. Ochs, A. Andrieu-Brunsen, R. Mohammadi, N. Vogel, Wetting-Controlled Localized Placement of Surface Functionalities within Nanopores, Small 16 (2020) 1906463. https://doi.org/10.1002/SMLL.201906463.

[161] K.Y. Kim, R.P. Srivastava, D.Y. Khang, Oleophilic to oleophobic wettability switching of isoporous through-hole membranes by surface structure control for low-voltage electrowetting-based oil-water separation, J Memb Sci 646 (2022). https://doi.org/10.1016/J.MEMSCI.2022.120281.

[162] J.W. Koo, J.S. Ho, J. An, Y. Zhang, C.K. Chua, T.H. Chong, A review on spacers and membranes: Conventional or hybrid additive manufacturing?, Water Res 188 (2021) 116497. https://doi.org/10.1016/J.WATRES.2020.116497.

[163] A. Khalil, F.E. Ahmed, N. Hilal, The emerging role of 3D printing in water desalination, Science of The Total Environment 790 (2021) 148238. https://doi.org/10.1016/J.SCITOTENV.2021.148238.

[164] L. Zhou, J. Miller, J. Vezza, M. Mayster, M. Raffay, Q. Justice, Z. Al Tamimi, G. Hansotte, L.D. Sunkara, J. Bernat, Additive Manufacturing: A Comprehensive Review, Sensors 2024, Vol. 24, Page 2668 24 (2024) 2668. https://doi.org/10.3390/S24092668.

[165] R.D. Crapnell, C. Kalinke, L.R.G. Silva, J.S. Stefano, R.J. Williams, R.A. Abarza Munoz, J.A. Bonacin, B.C. Janegitz,

C.E. Banks, Additive manufacturing electrochemistry: An overview of producing bespoke conductive additive manufacturing filaments, Materials Today 71 (2023) 73–90. https://doi.org/10.1016/J.MATTOD.2023.11.002.

[166] B.G. Thiam, A. El Magri, H.R. Vanaei, S. Vaudreuil, 3D Printed and Conventional Membranes—A Review, Polymers (Basel) 14 (2022) 1023. https://doi.org/10.3390/POLYM14051023/S1.

[167] A.L. Zydney, High Performance Ultrafiltration Membranes: Pore Geometry and Charge Effects, Membrane Science and Technology 14 (2011) 333–352. https://doi.org/10.1016/B978-0-444-53728-7.00015-X.

[168] K.J. Hwang, T.T. Lin, Effect of morphology of polymeric membrane on the performance of cross-flow microfiltration, J Memb Sci 199 (2002) 41–52. https://doi.org/10.1016/S0376-7388(01)00675-5.

[169] Y. Bougdid, Z. Sekkat, Voxels Optimization in 3D Laser Nanoprinting, Sci Rep 10 (2020) 1–8. https://doi.org/10.1038/s41598-020-67184-2.

[170] K.B. Fritzler, V.Ya. Prinz, 3D printing methods for micro- and nanostructures, Uspekhi Fizicheskih Nauk 189 (2019) 55–71. https://doi.org/10.3367/ufnr.2017.11.038239.

[171] P. Fiedor, J. Ortyl, A new approach to micromachining: High-precision and innovative additive manufacturing solutions based on photopolymerization technology, Materials 13 (2020) 1–25. https://doi.org/10.3390/ma13132951.

[172] Q. Ge, Z. Li, Z. Wang, K. Kowsari, W. Zhang, X. He, J. Zhou, N.X. Fang, Projection micro stereolithography based 3D printing and its applications, International Journal of Extreme

Manufacturing 2 (2020) 022004. https://doi.org/10.1088/2631-7990/AB8D9A.

[173] D.E. Marschner, S. Pagliano, P.H. Huang, F. Niklaus, A methodology for two-photon polymerization micro 3D printing of objects with long overhanging structures, Addit Manuf 66 (2023) 103474. https://doi.org/10.1016/J.ADDMA.2023.103474.

[174] M.Y. Sim, J.B. Park, D.Y. Kim, H.Y. Kim, J.M. Park, Dimensional accuracy and surface characteristics of complete-arch cast manufactured by six 3D printers, Heliyon 10 (2024) e30996. https://doi.org/10.1016/J.HELIYON.2024.E30996.

[175] E. Kluska, P. Gruda, N. Majca-Nowak, The Accuracy and the Printing Resolution Comparison of Different 3D Printing Technologies, Transactions on Aerospace Research 2018 (2018) 69–86. https://doi.org/10.2478/TAR-2018-0023.

[176] A. Al-Shimmery, S. Mazinani, J. Ji, Y.M.J. Chew, D. Mattia, 3D printed composite membranes with enhanced anti-fouling behaviour, J Memb Sci 574 (2019) 76–85. https://doi.org/10.1016/J.MEMSCI.2018.12.058.

[177] E. Koh, Y.T. Lee, Development of an embossed nanofiber hemodialysis membrane for improving capacity and efficiency via 3D printing and electrospinning technology, Sep Purif Technol 241 (2020) 116657. https://doi.org/10.1016/J.SEPPUR.2020.116657.

[178] S. Yuan, D. Strobbe, X. Li, J.P. Kruth, P. Van Puyvelde, B. Van der Bruggen, 3D printed chemically and mechanically robust membrane by selective laser sintering for separation of oil/water and immiscible organic mixtures, Chemical Engineering Journal 385 (2020) 123816. https://doi.org/10.1016/J.CEJ.2019.123816.

[179] G. Flodberg, H. Pettersson, L. Yang, Pore analysis and mechanical performance of selective laser sintered objects, Addit Manuf 24 (2018) 307–315. https://doi.org/10.1016/J.ADDMA.2018.10.001.

[180] S.M.H. Hojjatzadeh, N.D. Parab, W. Yan, Q. Guo, L. Xiong, C. Zhao, M. Qu, L.I. Escano, X. Xiao, K. Fezzaa, W. Everhart, T. Sun, L. Chen, Pore elimination mechanisms during 3D printing of metals, Nat Commun 10 (2019) 1–8. https://doi.org/10.1038/S41467-019-10973-9;TECHMETA=123;SUBJMETA=1023,1026,1032,301,639,930;KWRD=DESIGN.

[181] Z. Dong, H. Cui, H. Zhang, F. Wang, X. Zhan, F. Mayer, B. Nestler, M. Wegener, P.A. Levkin, 3D printing of inherently nanoporous polymers via polymerization-induced phase separation, Nature Communications 2021 12:1 12 (2021) 1–12. https://doi.org/10.1038/s41467-020-20498-1.

[182] B.S. Kirkebæk, A. Ali, C.A. Quist-Jensen, Masked stereolithography and polymerization induced phase separation for 3D printing of membranes, Sci Rep 15 (2025) 1–12. https://doi.org/10.1038/S41598-025-03527-1;SUBJMETA=166,455,638,639,898,959;KWRD=CHEMICAL+ENGINEERING,POLYMERIZATION+MECHANISMS.

[183] D. Godec, A. Pilipović, T. Breški, J. Ureña, O. Jordá, M. Martínez, J. Gonzalez-Gutierrez, S. Schuschnigg, J.R. Blasco, L. Portolés, Introduction to Additive Manufacturing, Springer Tracts in Additive Manufacturing Part F3252 (2024) 1–44. https://doi.org/10.1007/978-3-031-05863-9_1/FIGURES/23.

[184] A. Thorbole, C. Bodhak, P. Sahu, R.K. Gupta, Green ink revolution: Pioneering eco-friendly 3D printing with vegetable oil-derived inks, Polym Eng Sci 64 (2024) 5879–5902.

https://doi.org/10.1002/PEN.26974;WGROUP:STRING:PUBLICATION.

[185] T. Pirman, M. Ocepek, B. Likozar, Radical Polymerization of Acrylates, Methacrylates, and Styrene: Biobased Approaches, Mechanism, Kinetics, Secondary Reactions, and Modeling, Ind Eng Chem Res 60 (2021) 9347–9367. https://doi.org/10.1021/ACS.IECR.1C01649/ASSET/IMAGES/LARGE/IE1C01649_0007.JPEG.

[186] S. Subedi, S. Liu, W. Wang, S.M. Abu, N. Shovon, X. Chen, H. Oliver, T. Ware, Multi-material vat photopolymerization 3D printing: a review of mechanisms and applications, Npj Advanced Manufacturing 2024 1:1 1 (2024) 1–17. https://doi.org/10.1038/s44334-024-00005-w.

[187] S. Tisato, G. Vera, A. Mani, T. Chase, D. Helmer, An easy-to-build, accessible volumetric 3D printer based on a liquid crystal display for rapid resin development, Addit Manuf 87 (2024) 104232. https://doi.org/10.1016/J.ADDMA.2024.104232.

[188] H. Shafique, V. Karamzadeh, G. Kim, M.L. Shen, Y. Morocz, A. Sohrabi-Kashani, D. Juncker, High-resolution low-cost LCD 3D printing for microfluidics and organ-on-a-chip devices, Lab Chip 24 (2024) 2774–2790. https://doi.org/10.1039/D3LC01125A.

[189] J. Nam, M. Kim, Advances in materials and technologies for digital light processing 3D printing, Nano Convergence 2024 11:1 11 (2024) 1–25. https://doi.org/10.1186/S40580-024-00452-3.

[190] A.M.G. Cheadle, E. Maier, W.M. Palin, P.L. Tomson, G. Poologasundarampillai, M.A. Hadis, The impact of modifying 3D printing parameters on mechanical strength and physical

properties in vat photopolymerisation, Sci Rep 15 (2025) 1–12. https://doi.org/10.1038/S41598-025-97294-8;SUBJMETA=1005,1007,1032,12,301,639,930;KWRD=CHARACTERIZATION+AND+ANALYTICAL+TECHNIQUES,DESIGN.

[191] N. Butler, Y. Zhao, S. Lu, S. Yin, Effects of light exposure intensity and time on printing quality and compressive strength of β-TCP scaffolds fabricated with digital light processing, J Eur Ceram Soc 44 (2024) 2581–2589. https://doi.org/10.1016/J.JEURCERAMSOC.2023.11.046.

[192] X. Zhou, Y. Hou, J. Lin, A review on the processing accuracy of two-photon polymerization, AIP Adv 5 (2015) 30701. https://doi.org/10.1063/1.4916886/279889.

[193] L. Florea, E. Blasco, V. Mattoli, New Frontiers in Materials and Technologies for 3D Two Photon Polymerization, Adv Funct Mater 33 (2023) 2305697. https://doi.org/10.1002/ADFM.202305697;SUBPAGE:STRING:FULL.

[194] A.I. Bunea, N. del Castillo Iniesta, A. Droumpali, A.E. Wetzel, E. Engay, R. Taboryski, Micro 3D Printing by Two-Photon Polymerization: Configurations and Parameters for the Nanoscribe System, Micro 1 (2021) 164–180. https://doi.org/10.3390/MICRO1020013/S1.

[195] J. Wen, G. Nayyar, E.R. Crater, R.H. Bean, R. Zhang, R.B. Moore, T.E. Long, Vat photopolymerization of olefinic elastomers from sulfonated ethylene-propylene-diene monomer (EPDM) latexes, Addit Manuf 91 (2024) 104359. https://doi.org/10.1016/J.ADDMA.2024.104359.

[196] C.A. Figg, R.N. Carmean, K.C. Bentz, S. Mukherjee, D.A. Savin, B.S. Sumerlin, Tuning Hydrophobicity To Program

Block Copolymer Assemblies from the Inside Out, Macromolecules 50 (2017) 935–943. https://doi.org/10.1021/ACS.MACROMOL.6B02754/SUPPL_FILE/MA6B02754_SI_001.PDF.

[197] A.L. Ruiz Deance, B. Siersema, L.E.A.C. Yoe, F.R. Wurm, H. Gojzewski, Copolymerizing Lignin for Tuned Properties of 3D-Printed PEG-Based Photopolymers, ACS Appl Polym Mater 5 (2023) 10021–10031. https://doi.org/10.1021/ACSAPM.3C01875/ASSET/IMAGES/LARGE/AP3C01875_0004.JPEG.

[198] H.R. Zuo, P. Shi, M. Duan, A review on thermally stable membranes for water treatment: Material, fabrication, and application, Sep Purif Technol 236 (2020) 116223. https://doi.org/10.1016/J.SEPPUR.2019.116223.

[199] S. Bano, M. Pednekar, S. Rameshkumar, D. Borah, M.A. Morris, R.B. Padamati, N. Cronly, Fabrication and Evaluation of Filtration Membranes from Industrial Polymer Waste, Membranes (Basel) 13 (2023) 445. https://doi.org/10.3390/MEMBRANES13040445/S1.

[200] Y. Tang, Y. Lin, D.M. Ford, X. Qian, M.R. Cervellere, P.C. Millett, X. Wang, A review on models and simulations of membrane formation via phase inversion processes, J Memb Sci 640 (2021) 119810. https://doi.org/10.1016/J.MEMSCI.2021.119810.

[201] J. Stampfl, A. Wöß, S. Seidler, H. Fouad, A. Pisaipan, F. Schwager, R. Liska, Water Soluble, Photocurable Resins for Rapid Prototyping Applications, Macromol Symp 217 (2004) 99–108. https://doi.org/10.1002/MASY.200451308.

[202] W. Rao, X. Lu, C. Liu, Y. Xu, Y. He, Effect of concentration of water-soluble phenolic resin on the properties of carbon

paper for gas diffusion layer, Ceram Int 50 (2024) 2556–2564. https://doi.org/10.1016/J.CERAMINT.2023.09.337.

[203] P.K. Chan, A.D. Rey, A numerical method for the nonlinear Cahn-Hilliard equation with nonperiodic boundary conditions, Comput Mater Sci 3 (1995) 377–392. https://doi.org/10.1016/0927-0256(94)00076-O.

[204] A. Novick-Cohen, L.A. Segel, Nonlinear aspects of the Cahn-Hilliard equation, Physica D 10 (1984) 277–298. https://doi.org/10.1016/0167-2789(84)90180-5.

[205] E. Do, A. Soares, A.G. Barreto, F.W. Tavares, Exponential Integrators for Phase-Field Equations using Pseudo-spectral Methods: A Python Implementation, (2023). https://arxiv.org/pdf/2305.08998 (accessed July 1, 2025).

[206] R.L. Cosse, T. van der Most, V.S.D. Voet, R. Folkersma, K. Loos, Improving the Long-Term Mechanical Properties of Thermoplastic Short Natural Fiber Compounds by Using Alternative Matrices, Biomimetics 10 (2025) 46. https://doi.org/10.3390/BIOMIMETICS10010046/S1.

[207] M.J. Mullins, D. Liu, H.J. Sue, Mechanical properties of thermosets, Thermosets: Structure, Properties, and Applications: Second Edition (2018) 35–68. https://doi.org/10.1016/B978-0-08-101021-1.00002-2.

[208] X. Lu, B. Jiang, Glass transition temperature and molecular parameters of polymer, Polymer (Guildf) 32 (1991) 471–478. https://doi.org/10.1016/0032-3861(91)90451-N.

[209] A. Stoddart, W.J. Feast, S.P. Rannard, Synthesis and thermal studies of aliphatic polyurethane dendrimers: A geometric approach to the Flory-Fox equation for dendrimer glass

transition temperature, Soft Matter 8 (2012) 1096–1108. https://doi.org/10.1039/C1SM06725G/.

[210] S. Capponi, F. Alvarez, D. Račko, Free volume in a PVME polymer–water solution, Macromolecules 53 (2020) 4770–4782. https://doi.org/10.1021/ACS.MACROMOL.0C00472/ASSET/IMAGES/MEDIUM/MA0C00472_0009.GIF.

[211] H. Li, L. Liang, W. Zeng, Y. Deng, N. Ge, W. Shan, 3D printing polyurethane acrylate(PUA) based elastomer and its mechanical behavior, Mater Res Express 10 (2023) 055306. https://doi.org/10.1088/2053-1591/ACD740.

[212] S. Han, Y. Wang, Y. Xu, J. Wu, Preparation of foam material via co-sintering of NaCl and PTFE for oil/water separation, Journal of Porous Materials 31 (2024) 1005–1014. https://doi.org/10.1007/S10934-023-01539-8/FIGURES/9.

[213] B.S. Kirkebæk, M. Artemeva, J.L. Navas, A.H. Danielak, D.B. Pedersen, A. Ali, C.A. Quist-Jensen, Tunable physicochemical properties of 3D printed membranes via copolymerization and micropatterning, J Memb Sci 735 (2025) 124483. https://doi.org/10.1016/J.MEMSCI.2025.124483.

[214] F. Wang, L. Ratke, H. Zhang, P. Altschuh, B. Nestler, A phase-field study on polymerization-induced phase separation occasioned by diffusion and capillary flow—a mechanism for the formation of porous microstructures in membranes, J Solgel Sci Technol 94 (2020) 356–374. https://doi.org/10.1007/S10971-020-05238-7/FIGURES/15.

[215] B. Nagendra, A. Cozzolino, C. Daniel, P. Rizzo, G. Guerra, High Surface Area Nanoporous-Crystalline Polymer Films, Macromolecules 55 (2022) 2983–2990. https://doi.org/10.1021/acs.macromol.2c00271.

[216] S. Zhang, Surface roughness and membrane fouling, Nature Water 1 (2023) 132. https://doi.org/10.1038/s44221-023-00045-0.

[217] Z. Zhong, D. Li, B. Zhang, W. Xing, Membrane surface roughness characterization and its influence on ultrafine particle adhesion, Sep Purif Technol 90 (2012) 140–146. https://doi.org/https://doi.org/10.1016/j.seppur.2011.09.016.

[218] J. Liao, N. Brosse, A. Pizzi, S. Hoppe, X. Xi, X. Zhou, Polypropylene Blend with Polyphenols through Dynamic Vulcanization: Mechanical, Rheological, Crystalline, Thermal, and UV Protective Property, Polymers 2019, Vol. 11, Page 1108 11 (2019) 1108. https://doi.org/10.3390/POLYM11071108.

[219] Y. Zhang, B. Yang, K. Li, D. Hou, C. Zhao, J. Wang, Electrospun porous poly(tetrafluoroethylene-: Co - hexafluoropropylene- co -vinylidene fluoride) membranes for membrane distillation, RSC Adv 7 (2017) 56183–56193. https://doi.org/10.1039/C7RA09932K.

[220] M. Hassan, R.E.A. Zeid, W.S. Abou-Elseoud, E. Hassan, L. Berglund, K. Oksman, Effect of unbleached rice straw cellulose nanofibers on the properties of polysulfone membranes, Polymers (Basel) 11 (2019). https://doi.org/10.3390/POLYM11060938.

[221] W. Wei, H. Xu, Q. You, Q. Cheng, C. Liu, L. Zou, X. Liu, J. Liu, Y.C. Cao, G. Zheng, Preparation of quantum dot luminescent materials through the ink approach, Mater Des 91 (2016) 165–170. https://doi.org/10.1016/J.MATDES.2015.11.077.

[222] V.K. Thakur, E.J. Tan, M.F. Lin, P.S. Lee, Poly(vinylidene fluoride)-graft-poly(2-hydroxyethyl methacrylate): a novel

material for high energy density capacitors, J Mater Chem 21 (2011) 3751–3759. https://doi.org/10.1039/C0JM02408B.

[223] H.-R. Zuo, P. Shi, M. Duan, A review on thermally stable membranes for water treatment: Material, fabrication, and application, Sep Purif Technol 236 (2020) 116223. https://doi.org/https://doi.org/10.1016/j.seppur.2019.116223.

[224] L. Ni, Q. Shi, M. Wu, J. Ma, Y. Wang, Fouling behavior and mechanism of hydrophilic modified membrane in anammox membrane bioreactor: Role of gel layer, J Memb Sci 620 (2021) 118988. https://doi.org/https://doi.org/10.1016/j.memsci.2020.118988.

[225] T.K. Hussein, N.A. Jasim, A.-S.T. Al-Madhhachi, The Performance of Microfiltration Using Hydrophilic and Hydrophobic Membranes for Phenol Extraction from a Water Solution, ChemEngineering 7 (2023). https://doi.org/10.3390/chemengineering7020026.

[226] D. Murakami, H. Jinnai, A. Takahara, Wetting transition from the cassie-baxter state to the wenzel state on textured polymer surfaces, Langmuir 30 (2014) 2061–2067. https://doi.org/10.1021/LA4049067/SUPPL_FILE/LA4049067_SI_004.AVI.

[227] H. Li, X. Feng, K. Zhang, Study of the Classical Cassie Theory and Wenzel Theory Used in Nanoscale, J Bionic Eng 18 (2021) 398–408. https://doi.org/10.1007/s42235-021-0029-8.

[228] M.A. Zaman, S. Wang, Experimental investigation of surface roughness/wettability pattern effect on crystallization fouling over falling-film flow, Desalination 575 (2024) 117324. https://doi.org/https://doi.org/10.1016/j.desal.2024.117324.

[229] E. Curcio, G. Di Profio, Continuous Membrane Crystallization, in: N. Yazdanpanah, Z.K. Nagy (Eds.), The Handbook of Continuous Crystallization, The Royal Society of Chemistry, 2020: p. 0. https://doi.org/10.1039/9781788013581-00321.

[230] L.N. Nthunya, K.C. Chong, S.O. Lai, W.J. Lau, E.A. López-Maldonado, L.M. Camacho, M.M.A. Shirazi, A. Ali, B.B. Mamba, M. Osial, P. Pietrzyk-Thel, A. Pregowska, O.T. Mahlangu, Progress in membrane distillation processes for dye wastewater treatment: A review, Chemosphere 360 (2024) 142347. https://doi.org/https://doi.org/10.1016/j.chemosphere.2024.142347.

[231] O.M.A. Shahlol, H. Isawi, M.G. El-Malky, A.E.-H.M. Al-Aassar, A. El zwai, Performance evaluation of the different nano-enhanced polysulfone membranes via membrane distillation for produced water desalination in Sert Basin-Libya, Arabian Journal of Chemistry 13 (2020) 5118–5136. https://doi.org/https://doi.org/10.1016/j.arabjc.2020.02.011.

[232] A. Samadi, T. Ni, E. Fontananova, G. Tang, H. Shon, S. Zhao, Engineering antiwetting hydrophobic surfaces for membrane distillation: A review, Desalination 563 (2023) 116722. https://doi.org/https://doi.org/10.1016/j.desal.2023.116722.

[233] K. Chen, W. Zhang, A.L. Yarin, B. Pourdeyhimi, Polymer melting temperatures and crystallinity at different pressure applied, J Appl Polym Sci 138 (2021) 50936. https://doi.org/https://doi.org/10.1002/app.50936.

[234] Z. Liu, P. Maréchal, R. Jérôme, Melting and crystallization of poly(vinylidene fluoride) blended with polyamide 6, Polymer (Guildf) 38 (1997) 5149–5153.

https://doi.org/https://doi.org/10.1016/S0032-3861(97)00047-5.

[235] T.-W. Shyr, W.-C. Chung, W.-L. Lu, A.-J. Lin, Unusually high temperature transition and microporous structure of polytetrafluoroethylene fibre prepared through film fibrillation, Eur Polym J 72 (2015) 50–63. https://doi.org/https://doi.org/10.1016/j.eurpolymj.2015.08.017.

[236] K. Pochivalov, A. Basko, M. Yurov, T. Lebedeva, M. Shalygin, V. Lavrentyev, A. Yushkin, T. Anokhina, A. Volkov, Polypropylene membranes prepared via non-solvent/thermally induced phase separation: Effect of non-solvent nature, J Memb Sci 703 (2024) 122839. https://doi.org/https://doi.org/10.1016/j.memsci.2024.122839.

[237] L. Eykens, I. Hitsov, K. De Sitter, C. Dotremont, L. Pinoy, I. Nopens, B. Van der Bruggen, Influence of membrane thickness and process conditions on direct contact membrane distillation at different salinities, J Memb Sci 498 (2016) 353–364. https://doi.org/10.1016/J.MEMSCI.2015.07.037.

[238] A. Jenkins, G.G. Wells, R. Ledesma-Aguilar, D. Orejon, S. Armstrong, G. McHale, Suppression of crystallization in saline drop evaporation on pinning-free surfaces, J Chem Phys 158 (2023) 124708. https://doi.org/10.1063/5.0139448.

[239] T.K. Das, M. Folley, P. Lamont-Kane, C. Frost, Performance of a SWRO membrane under variable flow conditions arising from wave powered desalination, Desalination 571 (2024) 117069. https://doi.org/10.1016/J.DESAL.2023.117069.

[240] A.J. Schunke, G.A. Hernandez Herrera, L. Padhye, T.A. Berry, Energy Recovery in SWRO Desalination: Current Status and

New Possibilities, Frontiers in Sustainable Cities 2 (2020) 513595. https://doi.org/10.3389/FRSC.2020.00009/BIBTEX.

[241] L.G. Palacin, F. Tadeo, C. de Prada, J. Salazar, Scheduling of the membrane module rotation in RO desalination plants, Desalination Water Treat 51 (2013) 352–359. https://doi.org/10.1080/19443994.2012.715077.

[242] S. Kerdi, A. Qamar, J.S. Vrouwenvelder, N. Ghaffour, Effect of localized hydrodynamics on biofilm attachment and growth in a cross-flow filtration channel, Water Res 188 (2021) 116502. https://doi.org/10.1016/J.WATRES.2020.116502.

[243] W. Ni, Y. Li, G. Zhang, X. Du, Study of spacer structure on the enhancement of heat and mass transfer in direct contact membrane distillation modules, Desalination 530 (2022) 115617. https://doi.org/10.1016/J.DESAL.2022.115617.

[244] N. Sreedhar, N. Thomas, O. Al-Ketan, R. Rowshan, R.K. Abu Al-Rub, S. Hong, H.A. Arafat, Impacts of feed spacer design on UF membrane cleaning efficiency, J Memb Sci 616 (2020) 118571. https://doi.org/https://doi.org/10.1016/j.memsci.2020.118571.

[245] C.P. Koutsou, A.J. Karabelas, A novel retentate spacer geometry for improved spiral wound membrane (SWM) module performance, J Memb Sci 488 (2015) 129–142. https://doi.org/https://doi.org/10.1016/j.memsci.2015.03.064.

[246] Y. Ibrahim, N. Hilal, Enhancing ultrafiltration membrane permeability and antifouling performance through surface patterning with features resembling feed spacers, NPJ Clean Water 6 (2023) 60. https://doi.org/10.1038/s41545-023-00277-3.

[247] J.W. Koo, J.S. Ho, J. An, Y. Zhang, C.K. Chua, T.H. Chong, A review on spacers and membranes: Conventional or hybrid additive manufacturing?, Water Res 188 (2021) 116497. https://doi.org/https://doi.org/10.1016/j.watres.2020.116497.

[248] S.K. Karode, A. Kumar, Flow visualization through spacer filled channels by computational fluid dynamics I.: Pressure drop and shear rate calculations for flat sheet geometry, J Memb Sci 193 (2001) 69–84. https://doi.org/https://doi.org/10.1016/S0376-7388(01)00494-X.

[249] Y. Ibrahim, N. Hilal, Enhancing ultrafiltration membrane permeability and antifouling performance through surface patterning with features resembling feed spacers, NPJ Clean Water 6 (2023) 60. https://doi.org/10.1038/s41545-023-00277-3.

[250] S. Park, Y.D. Jeong, J.H. Lee, J. Kim, K. Jeong, K.H. Cho, 3D printed honeycomb-shaped feed channel spacer for membrane fouling mitigation in nanofiltration, J Memb Sci 620 (2021) 118665. https://doi.org/https://doi.org/10.1016/j.memsci.2020.118665.

[251] C. Cannilla, G. Bonura, F. Frusteri, Potential of Pervaporation and Vapor Separation with Water Selective Membranes for an Optimized Production of Biofuels—A Review, Catalysts 2017, Vol. 7, Page 187 7 (2017) 187. https://doi.org/10.3390/CATAL7060187.

[252] A. Martínez de Azagra, J. Del Río, World map of potential areas for the use of water cooling pitchers (botijos), J Maps 11 (2015) 240–244. https://doi.org/10.1080/17445647.2014.935499.

[253] D.E. Veinot, K.B. Langille, D.T. Nguyen, J.O. Bernt, Efflorescence of soluble silicate coatings, J Non Cryst Solids 127 (1991) 221–226. https://doi.org/10.1016/0022-3093(91)90146-W.

[254] Y. Wang, J. Lee, J.R. Werber, M. Elimelech, Capillary-driven desalination in a synthetic mangrove, Sci Adv 6 (2020). https://doi.org/10.1126/SCIADV.AAX5253/SUPPL_FILE/AAX5253_SM.PDF.

[255] P. Krishnamurthy, P.A. Jyothi-Prakash, L. Qin, J. He, Q. Lin, C.S. Loh, P.P. Kumar, Role of root hydrophobic barriers in salt exclusion of a mangrove plant Avicennia officinalis, Plant Cell Environ 37 (2014) 1656–1671. https://doi.org/10.1111/PCE.12272/SUPPINFO.

[256] J. Motuzas, C. Yacou, R.S.K. Madsen, W. Fu, D.K. Wang, A. Julbe, J. Vaughan, J.C. Diniz da Costa, Novel inorganic membrane for the percrystallization of mineral, food and pharmaceutical compounds, J Memb Sci 550 (2018) 407–415. https://doi.org/10.1016/J.MEMSCI.2017.12.077.

[257] R.S.K. Madsen, J. Motuzas, A. Julbe, J. Vaughan, J.C. Diniz da Costa, Novel membrane percrystallisation process for nickel sulphate production, Hydrometallurgy 185 (2019) 210–217. https://doi.org/10.1016/J.HYDROMET.2019.02.015.

[258] R.S.K. Madsen, J. Motuzas, J. Vaughan, A. Julbe, J.C. Diniz da Costa, Fine control of NaCl crystal size and particle size in percrystallisation by tuning the morphology of carbonised sucrose membranes, J Memb Sci 567 (2018) 157–165. https://doi.org/10.1016/J.MEMSCI.2018.09.003.

[259] G. Jyoti, A. Keshav, J. Anandkumar, Review on Pervaporation: Theory, Membrane Performance, and Application to Intensification of Esterification Reaction,

Journal of Engineering 2015 (2015) 927068. https://doi.org/10.1155/2015/927068.

[260] J.J. Moltedo, A. Schwarz, A. Gonzalez-Vogel, Evaluation of percrystallization coupled with electrodialysis for zero liquid discharge in the pulping industry, J Environ Manage 303 (2022) 114104. https://doi.org/10.1016/J.JENVMAN.2021.114104.

[261] H.A. Nooruddin, M.E. Hossain, Modified Kozeny–Carmen correlation for enhanced hydraulic flow unit characterization, J Pet Sci Eng 80 (2011) 107–115. https://doi.org/10.1016/J.PETROL.2011.11.003.

[262] M. Xiao, X. Wang, Z. Hou, J. Alan Quezada Renteria, D.S. Dlamini, D. Jassby, E.M.V. Hoek, Comparison of classical hydrodynamic models of transport through porous membranes, Sep Purif Technol 360 (2025) 131189. https://doi.org/10.1016/J.SEPPUR.2024.131189.

[263] M.H. Nielsen, C. Quist-Jensen, A. Ali, Development of ceramic membranes for resource recovery from brine through percrystallization, Resour Conserv Recycl 189 (2023) 106768. https://doi.org/10.1016/J.RESCONREC.2022.106768.

[264] J.G. Wijmans, R.W. Baker, The solution-diffusion model: a review, J Memb Sci 107 (1995) 1–21. https://doi.org/10.1016/0376-7388(95)00102-I.

[265] A.O. Emmanuel, F.A. Oladipo, O.O. E., Investigation of Salinity Effect on Compressive Strength of Reinforced Concrete, J Sustain Dev 5 (2012) p74. https://doi.org/10.5539/JSD.V5N6P74.

[266] X. Yan, B. Wu, Q. Wu, L. Chen, F. Ye, D. Chen, Interfacial Engineering of Attractive Pickering Emulsion Gel-Templated

Porous Materials for Enhanced Solar Vapor Generation, Energies (Basel) 14 (2021). https://doi.org/10.3390/en14196077.

[267] A. Ali, J.H. Jacobsen, H.C. Jensen, M.L. Christensen, C.A. Quist-Jensen, Treatment of Wastewater Solutions from Anodizing Industry by Membrane Distillation and Membrane Crystallization, Applied Sciences 2019, Vol. 9, Page 287 9 (2019) 287. https://doi.org/10.3390/APP9020287.

[268] X. Zhang, R. Koirala, B. Pramanik, L. Fan, Y. Zhang, A. Date, V. Jegatheesan, Performance of membrane distillation assisted crystallization and crystal characteristics for resource recovery from desalination brine, Desalination 574 (2024) 117244. https://doi.org/10.1016/J.DESAL.2023.117244.

[269] G. Ji, W. Wang, H. Chen, S. Yang, J. Sun, W. Fu, Z. Huang, B. Yang, A novel membrane-promoted crystallization process integrating water recovery and salt production for brine management, Chemical Engineering Journal 430 (2022) 133022. https://doi.org/10.1016/J.CEJ.2021.133022.

[270] P. Wang, W. Cheng, X. Zhang, Q. Liu, J. Li, J. Ma, T. Zhang, Membrane Scaling and Wetting in Membrane Distillation: Mitigation Roles Played by Humic Substances, Environ Sci Technol 56 (2022) 3258–3266. https://doi.org/10.1021/ACS.EST.1C07294/ASSET/IMAGES/LARGE/ES1C07294_0006.JPEG.

[271] L. Basini, G. D’Angelo, M. Gobbi, G.C. Sarti, C. Gostoli, A desalination process through sweeping gas membrane distillation, Desalination 64 (1987) 245–257. https://doi.org/https://doi.org/10.1016/0011-9164(87)90100-7.

[272] S.H. Kim, H. Yoon, T. Min, B. Han, S. Lim, J. Park, Carbon dioxide utilization in lithium carbonate precipitation: A short

review, Environmental Engineering Research 29 (2024) 230553. https://doi.org/10.4491/EER.2023.553.

[273] M. Abunada, N. Dhakal, R. Gulrez, P. Ajok, Y. Li, A. Abushaban, H. Smit, D. Moed, N. Ghaffour, J.C. Schippers, M.D. Kennedy, Prediction of particulate fouling in full-scale reverse osmosis plants using the modified fouling index – ultrafiltration (MFI-UF) method, Desalination 553 (2023) 116478. https://doi.org/10.1016/J.DESAL.2023.116478.

[274] M. Philibert, L.O. Villacorte, Y. Ekowati, A. Abushaban, S.G. Salinas-Rodriguez, Fouling and scaling in reverse osmosis desalination plants: A critical review of membrane autopsies, feedwater quality guidelines and assessment methods, Desalination 592 (2024) 118188. https://doi.org/10.1016/J.DESAL.2024.118188.

[275] A. Alkhatib, M.A. Ayari, A.H. Hawari, Fouling mitigation strategies for different foulants in membrane distillation, Chemical Engineering and Processing - Process Intensification 167 (2021) 108517. https://doi.org/10.1016/J.CEP.2021.108517.

[276] S. Soukane, H. Elcik, A. Alpatova, J. Orfi, E. Ali, H. AlAnsary, N. Ghaffour, Scaling sets the limits of large scale membrane distillation modules for the treatment of high salinity feeds, J Clean Prod 287 (2021) 125555. https://doi.org/10.1016/J.JCLEPRO.2020.125555.

[277] J.M. Arnal, M. Sancho, I. Iborra, J.M. Gozálvez, A. Santafé, J. Lora, Concentration of brines from RO desalination plants by natural evaporation, Desalination 182 (2005) 435–439. https://doi.org/10.1016/J.DESAL.2005.02.036.

[278] D. Amiruddin, D. Mahajan, D. Fang, W. Wang, P. Wang, B.S. Hsiao, A Facile Ultrapure Water Production Method for

Electrolysis via Multilayered Photovoltaic/Membrane Distillation, Energies 2023, Vol. 16, Page 5765 16 (2023) 5765. https://doi.org/10.3390/EN16155765.

[279] L.A. Melnik, D.A. Krysenko, Ultrapure Water: Properties, Production, and Use, Journal of Water Chemistry and Technology 2019 41:3 41 (2019) 143–150. https://doi.org/10.3103/S1063455X19030020.

[280] I. Bouaziz, M.S. Takriff, M.A. Atieh, A. Shanableh, S.N. Backer, I.W. Almanassra, H. Alawadhi, Sustainable brine management: Unlocking magnesium and calcium for improved carbonation in the modified Solvay process, Desalination Water Treat 319 (2024) 100526. https://doi.org/10.1016/J.DWT.2024.100526.

[281] E.U. Khan, Å. Nordberg, P. Malmros, Waste Heat Driven Integrated Membrane Distillation for Concentrating Nutrients and Process Water Recovery at a Thermophilic Biogas Plant, Sustainability 2022, Vol. 14, Page 13535 14 (2022) 13535. https://doi.org/10.3390/SU142013535.

[282] S.M. Shalaby, A.E. Kabeel, H.F. Abosheiasha, M.K. Elfakharany, E. El-Bialy, A. Shama, R.D. Vidic, Membrane distillation driven by solar energy: A review, J Clean Prod 366 (2022) 132949. https://doi.org/10.1016/J.JCLEPRO.2022.132949.

[283] P.H. Nadeau, S. Sun, S.N. Ehrenberg, The “Golden Zone” temperature distribution of oil and gas occurrence examined using a global empirical database, Mar Pet Geol 158 (2023) 106507. https://doi.org/10.1016/J.MARPETGEO.2023.106507.

[284] S. Deshmukh, Ultrapure Water Production, Handbook of Water and Used Water Purification (2020) 1–22. https://doi.org/10.1007/978-3-319-66382-1_106-1.

[285] E. Alkaya, G.N. Demirer, Water recycling and reuse in soft drink/beverage industry: A case study for sustainable industrial water management in Turkey, Resour Conserv Recycl 104 (2015) 172–180. https://doi.org/10.1016/J.RESCONREC.2015.08.011.

[286] E.O. Ezugbe, S. Rathilal, Membrane Technologies in Wastewater Treatment: A Review, Membranes (Basel) 10 (2020). https://doi.org/10.3390/MEMBRANES10050089.

[287] N. Sharmili, R. Nagi, P. Wang, A review of research in the Li-ion battery production and reverse supply chains, J Energy Storage 68 (2023) 107622. https://doi.org/10.1016/J.EST.2023.107622.

[288] R. Febrida, S. Setianto, E. Herda, A. Cahyanto, I.M. Joni, Structure and phase analysis of calcium carbonate powder prepared by a simple solution method, Heliyon 7 (2021) e08344. https://doi.org/10.1016/J.HELIYON.2021.E08344.

[289] S. Li, B. Lian, Application of Calcium Carbonate as a Controlled Release Carrier for Therapeutic Drugs, Minerals 2023, Vol. 13, Page 1136 13 (2023) 1136. https://doi.org/10.3390/MIN13091136.

[290] M. Younes, G. Aquilina, L. Castle, G. Degen, K.H. Engel, P.J. Fowler, M.J. Frutos Fernandez, P. Fürst, R. Gürtler, T. Husøy, M. Manco, W. Mennes, P. Moldeus, S. Passamonti, R. Shah, I. Waalkens-Berendsen, M. Wright, D. Wölfle, B. Dusemund, A. Mortensen, D. Turck, K. Cheyns, E. Gaffet, K. Loeschner, J. Mast, M. Mirat, A. Undas, S. Barmaz, A. Mech, A.M. Rincon, C. Smeraldi, A. Tard, U. Gundert-Remy, Re-evaluation of

calcium carbonate (E 170) as a food additive in foods for infants below 16 weeks of age and follow-up of its re-evaluation as food additive for uses in foods for all population groups, EFSA Journal 21 (2023) e08106. https://doi.org/10.2903/J.EFSA.2023.8106.

[291] J.C. Abanades, Y.A. Criado, H.I. White, Direct capture of carbon dioxide from the atmosphere using bricks of calcium hydroxide, Cell Rep Phys Sci 4 (2023) 101339. https://doi.org/10.1016/J.XCRP.2023.101339.

[292] N. McQueen, P. Kelemen, G. Dipple, P. Renforth, J. Wilcox, Ambient weathering of magnesium oxide for CO2 removal from air, Nature Communications 2020 11:1 11 (2020) 1–10. https://doi.org/10.1038/s41467-020-16510-3.

[293] T. Li, T.C. Keener, L. Cheng, Carbon dioxide removal by using Mg(OH)2 in a bubble column: Effects of various operating parameters, International Journal of Greenhouse Gas Control 31 (2014) 67–76. https://doi.org/10.1016/J.IJGGC.2014.09.027.

[294] W. Ye, J. Huang, J. Lin, X. Zhang, J. Shen, P. Luis, B. Van Der Bruggen, Environmental evaluation of bipolar membrane electrodialysis for NaOH production from wastewater: Conditioning NaOH as a CO2 absorbent, Sep Purif Technol 144 (2015) 206–214. https://doi.org/10.1016/J.SEPPUR.2015.02.031.

[295] P. Descamps, J. Iker, A.T. Wolf, Effects of anodized aluminium surface parameters on the long-term adhesion of silicone structural glazing sealants, Constr Build Mater 10 (1996) 527–538. https://doi.org/10.1016/0950-0618(96)00008-6.

[296] A. Musza, M. Windisch, M. Török, T. Molnár, S. Kovács, S. Sátán-Papp, K. Szegedi, D. Ugi, N.Q. Chinh, Á. Vida, Tribological Examination of Anodized Al-356 for Automotive Use, Coatings 2023, Vol. 13, Page 1642 13 (2023) 1642. https://doi.org/10.3390/COATINGS13091642.

[297] F. Guo, Y. Cao, K. Wang, P. Zhang, Y. Cui, Z. Hu, Z. Xie, Effect of the Anodizing Temperature on Microstructure and Tribological Properties of 6061 Aluminum Alloy Anodic Oxide Films, Coatings 2022, Vol. 12, Page 314 12 (2022) 314. https://doi.org/10.3390/COATINGS12030314.

[298] M.P. Martínez-Viademonte, S.T. Abrahami, T. Hack, M. Burchardt, H. Terryn, A Review on Anodizing of Aerospace Aluminum Alloys for Corrosion Protection, Coatings 2020, Vol. 10, Page 1106 10 (2020) 1106. https://doi.org/10.3390/COATINGS10111106.

[299] A. Ali, J.H. Jacobsen, H.C. Jensen, M.L. Christensen, C.A. Quist-Jensen, Treatment of Wastewater Solutions from Anodizing Industry by Membrane Distillation and Membrane Crystallization, Applied Sciences 2019, Vol. 9, Page 287 9 (2019) 287. https://doi.org/10.3390/APP9020287.

[300] A. Olsen, W. Luterek, M. Sørensen, A. Grønne, N. Jensen, S. Niss, A. Ali, B. Kirkebæk, Membrane Distillation for Wastewater Treatment in the Anodisation Industry, 2023. https://www.en.bio.aau.dk/.

[301] The Sealing Step in Aluminum Anodizing, (n.d.). https://finishingandcoating.com/index.php/anodizing/1220-the-sealing-step-in-aluminum-anodizing (accessed June 11, 2024).

[302] S. Theohari, C. Kontogeorgou, Effect of temperature on the anodizing process of aluminum alloy AA 5052, Appl Surf Sci

284 (2013) 611–618. https://doi.org/10.1016/J.APSUSC.2013.07.141.

[303] Anodizing Technology Cleaning, (n.d.). https://finishingandcoating.com/index.php/cleaning-pretreatment/582-anodizing-technology-cleaning (accessed June 11, 2024).

[304] Agriculture and Resource Management Council of Australia and New Zealand., Australian and New Zealand Environment and Conservation Council., Guidelines for sewerage systems : acceptance of trade waste (industrial waste)., Agriculture and Resource Management Council of Australia and New Zealand, Australian and New Zealand Environment and Conservation Council, 1994.

[305] afledningstilladelse-european-protein-271217, (n.d.).

[306] D.J. Johnson, W.A. Suwaileh, A.W. Mohammed, N. Hilal, Osmotic's potential: An overview of draw solutes for forward osmosis, Desalination 434 (2018) 100–120. https://doi.org/https://doi.org/10.1016/j.desal.2017.09.017.

[307] N.K. Rastogi, 1 - Forward osmosis: Principles, applications, and recent developments, in: A. Basile, A. Cassano, N.K. Rastogi (Eds.), Current Trends and Future Developments on (Bio-) Membranes, Elsevier, 2020: pp. 3–35. https://doi.org/https://doi.org/10.1016/B978-0-12-816777-9.00001-0.

[308] C. Abels, F. Carstensen, M. Wessling, Membrane processes in biorefinery applications, J Memb Sci 444 (2013) 285–317. https://doi.org/10.1016/J.MEMSCI.2013.05.030.

[309] E. Arnese-Feffin, P. Facco, D. Turati, F. Bezzo, M. Barolo, Understanding Fouling in an Industrial Biorefinery Membrane

Separation Process by Feature-Oriented Data-Driven Modeling, Ind Eng Chem Res 63 (2024) 9136–9150. https://doi.org/10.1021/ACS.IECR.4C00590/ASSET/IMAGES/LARGE/IE4C00590_0015.JPEG.

[310] H. Zhang, X. Zhao, Enhanced Anti-Wetting Methods of Hydrophobic Membrane for Membrane Distillation, Advanced Science 10 (2023) 2300598. https://doi.org/10.1002/ADVS.202300598;PAGEGROUP:STRING:PUBLICATION.

[311] T. Horseman, Y. Yin, K.S.S. Christie, Z. Wang, T. Tong, S. Lin, Wetting, Scaling, and Fouling in Membrane Distillation: State-of-the-Art Insights on Fundamental Mechanisms and Mitigation Strategies, ACS ES and T Engineering 1 (2021) 117–140. https://doi.org/10.1021/ACSESTENGG.0C00025/ASSET/IMAGES/MEDIUM/EE0C00025_0012.GIF.

[312] F.B. Dilek, U. Yetis, C.F. Gökçay, Water savings and sludge minimization in a beet-sugar factory through re-design of the wastewater treatment facility, J Clean Prod 11 (2003) 327–331. https://doi.org/10.1016/S0959-6526(02)00029-X.

[313] NordicSugar, From the beet to sugar How we extract sugar from beet, (2022) 4.

[314] S. Fida, M. Yasmeen, R. Adnan, M. Zeeshan, Treatment methods for sugar rich wastewater: A review, Cleaner Water 3 (2025) 100067. https://doi.org/10.1016/J.CLWAT.2025.100067.

[315] S. Sharma, H. Simsek, Sugar beet industry process wastewater treatment using electrochemical methods and optimization of parameters using response surface methodology, Chemosphere

238 (2020) 124669. https://doi.org/10.1016/J.CHEMOSPHERE.2019.124669.

[316] L.D. Tijing, Y.C. Woo, J.S. Choi, S. Lee, S.H. Kim, H.K. Shon, Fouling and its control in membrane distillation—A review, J Memb Sci 475 (2015) 215–244. https://doi.org/10.1016/J.MEMSCI.2014.09.042.

[317] Y. Chen, X. Ding, Y. Zhang, A. Natalia, X. Sun, Z. Wang, H. Shao, Design and synthesis of magnetic nanoparticles for biomedical diagnostics, Quant Imaging Med Surg 8 (2018) 95770–95970. https://doi.org/10.21037/QIMS.2018.10.07.

[318] T.D. Schladt, K. Schneider, H. Schild, W. Tremel, Synthesis and bio-functionalization of magnetic nanoparticles for medical diagnosis and treatment, Dalton Transactions 40 (2011) 6315–6343. https://doi.org/10.1039/C0DT00689K.

[319] H.E. Ahmed, B.H. Salman, A.S. Kherbeet, M.I. Ahmed, Optimization of thermal design of heat sinks: A review, Int J Heat Mass Transf 118 (2018) 129–153. https://doi.org/10.1016/J.IJHEATMASSTRANSFER.2017.10.099.

[320] A. Steen, J. Jensen, L. Bang, S. Khai, A. Ali, B. Kirkebæk, Percrystallization with Additively Manufactured Membranes Subject: Additive Manufacturing of Membranes, 2023.

Appendices